

國立臺灣大學理學院大氣科學研究所

博士論文

Graduate Institute of Atmospheric Sciences

College of Science

National Taiwan University

Doctoral Dissertation



可預報冰晶成長習性和視密度之多矩量冷雲總體雲微
物理參數法應用於WRF模式

A Multi-Moment Bulkwater Ice Microphysics Scheme with
Consideration of the Adaptive Growth Habit and Apparent
Density for Pristine Ice in the WRF Model

蔡子衿

Tzu-Chin Tsai

指導教授：陳正平 博士

Advisor: Jen-Ping Chen, Ph.D.

中華民國 103 年 9 月

September 2014

|





國立臺灣大學博士學位論文
口試委員會審定書

本論文係 蔡子衿 君 (學號 D97229002) 在國立臺灣大學
大氣科學系、所完成之博士學位論文，於民國 103 年 8 月 8 日承下
列考試委員審查通過及口試及格，特此證明

口試委員：

陳正午

(簽名)

(指導教授)

陳淑華

王寶貴

陳維序

楊明仁

吳維倫

隋中興

系主任、所長

[Signature]

(簽名)



摘要


在雲模式中，冰晶複雜的形狀和其成長機制一直是冷雲參數法裡不易處理的物理過程。而本研究根據Chen and Lamb在1994年所提的冰晶成長理論參數法發展出一套冰晶形狀總體參數法，還建立一個具有六種雙矩量(質量和數量)水物且都是伽碼粒徑分佈的總體雲物理參數法。兩個新的參數法都已移植至WRF氣象模式，成為一個多矩量總體雲微物理參數法。在新的參數法中，更針對雲冰增加了冰晶形狀和體積兩個矩量來預報其成長習性和視密度，並提出一個使用第零、第二和第三矩量之矩量閉合方法。而冰晶形狀總體參數法的理論驗證是和細格(bin)方法作比較；氣塊(parcel)法零維計算的結果展示出粒徑譜形能彈性變化的重要性，以及冰晶形狀對其凝華成長的顯著影響，同時冰晶的成長習性能夠根據不同的環境條件及初始粒徑做出調整；總體三矩量方法和細格方法的結果較為一致。至於觀測驗證，分別選取C3VP和DIAMET兩個冬季觀測計畫之個案以WRF模式進行模擬，並分別假設球形和非球形的冰晶來評估其影響程度。C3VP個案模擬結果顯示出雲冰形狀在雲物理過程、地面降水和輻射通量的顯著影響及較為接近真實的冰晶成長習性演變。而DIAMET個案結果顯示，新的雲微物理參數法能準確地預報其鋒面狹長雨帶的降水結構和伴隨的天氣特徵，且模擬出柱狀和碟狀冰晶在不同溫度區間的垂直分布並記憶其形狀的演變，而和飛機雲物理觀測資料的比較亦顯示冰晶在其二次增殖生成的溫度區間，兩者在冰晶數量濃度、綜橫軸比例和其凝華加熱率具有高度的一致性。

關鍵字：冰晶形狀，冰晶習性，WRF，雲物理參數法，C3VP，DIAMET

ABSTRACT



The wide variety of ice crystal shapes and growth habits makes it a complicated issue in cloud models. This study developed the bulk ice adaptive habit parameterization based on the theoretical approach of Chen and Lamb (1994) and introduced a 6-class hydrometeors double-moment (mass and number) bulk microphysics scheme with gamma-type size distribution function. Both the proposed schemes have been implemented into the Weather Research and Forecasting model (WRF) model forming a new multi-moment bulk microphysics scheme. Two new moments of ice crystal shape and volume are included for tracking pristine ice's adaptive habit and apparent density. A closure technique is developed to solve the time evolution of the bulk moments. For the verification of the bulk ice habit parameterization, some parcel-type (zero-dimension) calculations were conducted and compared with binned numerical calculations. The results showed that: a flexible size spectrum is important in numerical accuracy, the ice shape can significantly enhance the diffusional growth, and it is important to consider the memory of growth habit (adaptive growth) under varying environmental conditions. Also, the derived results with the 3-moment method were much closer to the binned calculations. Two field campaigns from the C3VP and DIAMET were selected to simulate in the WRF model for real-case



studies. The simulations were performed with the traditional spherical ice and the new adaptive shape schemes to evaluate the effect of crystal habits. Realistic evolution of ice growth habits and great impacts on the ice-phase microphysical processes, surface precipitations, and radiation fluxes were found in the simulation results of C3VP case. For the DIAMET case, some main features of narrow rain band, as well as the embedded precipitation cells, in the cold front case were well captured by the model. The vertical variation of ice crystal shapes was nicely simulated. Furthermore, the simulations produced a good agreement in the microphysics against the aircraft observations in ice particle number concentration, ice crystal aspect ratio, and deposition heating rate especially within the temperature region of ice secondary multiplication production.

Keywords: crystal shape, ice habit, WRF, cloud scheme, C3VP, DIAMET

ACKNOWLEDGEMENTS



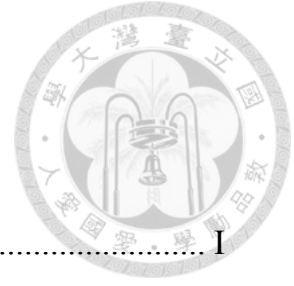
本篇論文可以順利完成，要感謝的人很多。首先是指導教授陳正平老師，除提供良好的工作環境，並每在研究遇到瓶頸時，適時給予建議；而老師在研究上精益求精的嚴謹態度，不僅促進研究能力的提昇，亦是為學最有效的身教。感謝口試委員隋中興老師、王寶貫老師、楊明仁老師、陳維婷老師、陳淑華老師及吳健銘老師，在百忙之中親臨指導，並提出各項建議使論文內容益加充實。

感謝赴美 NASA/GSFC 研習期間，陶為國博士及其研究團隊所給予的指導和協助，以及朱定中博士、謝鍾靈博士、許乾忠學長和 Michael Yen 學長等人在生活上的照顧，這段時間著實增廣自己的視野，也培養出學習解決研究問題的基本態度。此外模式發展期間，感謝 Dr. Christopher Dearden 參與討論並提供觀測資料來驗證模擬結果。還要感謝雲與氣膠研究室的大家庭成員們，以及環保署監資處二科同仁們，多年來持續給予打氣和鼓勵。

最後，感謝家人們這些年的體諒，特別是太太多年來的陪伴和支持，讓我可以無後顧之憂，專心在研究工作上。

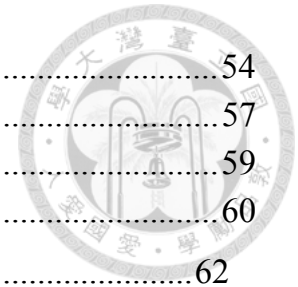
真的很感謝您們~

TABLE OF CONTENTS



摘要	I
ABSTRACT	II
ACKNOWLEDGEMENTS	IV
TABLE OF CONTENTS	V
LIST OF TABLES	VII
LIST OF FIGURES	VIII
1. Introduction	1
1.1 Ice crystal habits	1
1.2 Bulk approaches	4
1.3 Microphysics schemes in WRF	6
1.4 Motivation	8
2. Methodology	10
2.1 An adaptive growth habit bulkwater parameterization	10
2.1.1 Bulk ice shape and volume moments	11
2.1.2 Deposition growth	14
2.1.3 Riming growth	19
2.1.4 Accretion rate by other particles	22
2.1.5 Aggregation among pristine ice	24
2.1.6 Mass-dimension and Area-dimension relationships	26
2.1.7 Terminal velocity-dimension relationships	29
2.1.8 Ventilation effect	32
2.1.9 3-moment closure technique	34
2.1.10 Orientation of crystal shape	36
2.1.11 Remarks	38
2.2 A new multi-moment microphysics scheme	38
2.2.1 Activation/deactivation	41
2.2.2 Nucleation/multiplication	43
2.2.3 Vapor diffusion/evaporation	47
2.2.4 Accretion/aggregation	48
2.2.5 Auto-conversion/ initiation of graupel/breakup	52

2.2.6 Hailstone growth/Shedding	54
2.2.7 Melting of frozen particles	57
2.2.8 Remarks	59
2.3 Summary	60
3. Zero-dimension calculations	62
3.1 The role of ice crystal shape and spectral index	63
3.2 Adaptive growth	67
3.3 Ice growth dependence on initial size	70
3.4 Ice growth with ventilation effect	72
3.5 Ice crystal shape effect on radiation flux	74
3.6 Summary	76
4. The WRF model simulation results	78
4.1 C3VP synoptic snowfall event	78
4.1.1 Model setup	80
4.1.2 Simulation results	82
4.1.3 Remarks	88
4.2 DIAMET cold-front event	89
4.2.1 Model setup	91
4.2.2 Simulation results	93
4.2.3 Remarks	106
4.3 Summary	107
5. Conclusions	109
5.1 Summary	109
5.2 Future perspective	110
References	112
Tables	119
Figures	124
Appendix A	162
Appendix B	165



LIST OF TABLES



Table 1 The prognostic variables in terms to the current microphysics schemes in the WRF model for version 3.4.1, where Q , N , and V represents mixing ratio, number concentration, and volume whereas v , c , r , i , s , g , h , and ccn are denoted water vapor, cloud, rain, ice, snow, graupel, hail and cloud condensation nuclei, respectively.....	119
Table 2 The lists of ice shape and volume moments used in the new microphysics scheme.	119
Table 3 The coefficients used for the spectral index (α_x), the mass-dimensional relationship (a_{mx} , b_{mx}), bulk density (ρ_x), terminal velocity-dimensional relationship (a_{vx} , b_{vx}) for all hydrometeor categories.	120
Table 4 All collection efficiencies E utilized in the new microphysics scheme. The left two columns represent interacting hydrometeor categories, where T_c is air temperature in C degree, D is the mean volume diameter, ρ_x is the bulk density, and $STOKE$ is the stoke number.	120
Table 5 All notations BMP_{xy} (or BMP_{xyz}) utilized in the new microphysics scheme, where B for the prognostic variable, MP for the microphysical process, and xyz for the hydrometeor category.	121
Table 6 Coefficients of the formulas adopted from Chen and Liu (2004).....	122
Table 7 Numbers, means, and geometric width of nucleation (Nu), accumulation (Ac), and coarse (Co) modes of three aerosol size distribution types over marine and continent types, including clean, average and urban background.	122
Table 8 Parameters used for the ice deposition-nucleation mode.	122
Table 9 The model setup for the new multi-moment microphysics and GSFC radiation schemes with respect to three simulations of Sphere-2M, Shape-2M, and Shape-3M. Circle was represented for available whereas cross was not.	123
Table 10 The WRF model setup and physics options used for the C3VP case.	123
Table 11 The WRF model setup and physics options used for the DIAMET case.	123

LIST OF FIGURES



Figure 1.1 Perspective views of prolate and oblate spheroids that resemble columnar and planar ice crystals, respectively.	124
Figure 1.2 The illustration of ice crystal habit diagram as a function of both temperature and ice supersaturation. (Download from the website of www.cas.manchester.ac.uk).	124
Figure 2.1 The ice shape enhanced factor (y -axis) with respect to the adaptive growth ratio (x -axis, $\zeta < 0$ for oblate while $\zeta > 0$ for prolate).	125
Figure 2.2 The original (in triangle red) and corrected (in circle blue) data points between $\left(\frac{M_3}{M_3^*}\right)^\zeta$ (y -axis) and $\frac{M_\phi}{M_3}$ (x -axis).	125
Figure 2.3 The shaded contour of pristine ice fall speed (m/s) in terms of equivalent diameters (y -axis) from $1 \mu\text{m}$ to 2 mm and adaptive growth ratios (x -axis, $\zeta < 0$ for oblate while $\zeta > 0$ for prolate) at a given density of 500 kg m^{-3}	126
Figure 2.4 The shaded contour of pristine ice ventilation effect in terms of equivalent diameters (y -axis) from $1 \mu\text{m}$ to 2 mm and adaptive growth ratios (x -axis, $\zeta < 0$ for oblate while $\zeta > 0$ for prolate) at a given density of 900 kg m^{-3}	126
Figure 2.5 The representation of hydrometeor categories predicted in the new microphysics scheme, where Q , N , F , and V represents mixing ratio, number concentration, shape, and volume whereas v , c , r , i , s , g , h , in , and ccn are denoted water vapor, cloud, rain, ice, snow, graupel, hail, ice nuclei, and cloud condensation nuclei, respectively.	127
Figure 2.6 The aerosol spectrums of marine (blue), clean (green), average (yellow), and urban (red) type referred to Whitby (1978).	127
Figure 3.1 The representations of initial spectrum for the bulk (left) and bin (right) methods with the parameters of $\lambda_i = 8 \times 10^5 \text{ m}^{-1}$, $N_i = 100 \text{ m}^{-3}$, and $\alpha_i = 3$	128
Figure 3.2 The calculation results of (a) the 3 rd -moment, (b) the bulk aspect ratio, and (c) the bulk adaptive growth ratio for shape ice with the bin (in solid-black), bulk-2M (in dotted-green), and bulk-3M (in dash-red) methods, as well as for spherical ice	

with the bin (solid-gray) and bulk-2M methods (in dash-dot-blue). For these calculations, $T=266\text{K}$, $P=800\text{ hpa}$, $\Delta Q_{vi}=10^{-5}\text{ kg kg}^{-1}$, $f_{vi}=1$, and $\Gamma(T)=2.0$ 129

Figure 3.3 The size spectrums of the Shape-bin (in solid-black), Sphere-bin (in solid-gray) Shape-3M (in dash-red), Shape-2M (in dotted-green), and Sphere-2M (in dash-dot-blue) with an indicator of α_i individually at the starting 200 seconds with an interval of 40s depicted from panel (a) to (f). 130

Figure 3.4 The bar chart plots of β in each bin for Shape-bin calculation at the (a) zero, (b) 1000, and (c) 5000 seconds, respectively. The x -axis denoted the number of bin from 1 to 100 and the y -axis was the representation of β 131

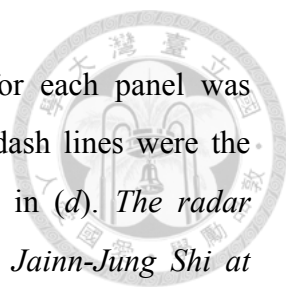
Figure 3.5 The calculation results of (a) the 3rd-moment, (b) the bulk aspect ratio, and (c) the bulk adaptive growth ratio for shape ice with the bin (in solid-black), bulk-2M (in dotted-green), and bulk-3M (in dash-red) methods. For these calculations, the environment was the same to Figure 3.2 except for $\Gamma(T)=0.5$ after 200 seconds. 132

Figure 3.6 The bar chart plots of the Shape-bin's calculation results over (a) the adaptive growth ratio and (b) the equivalent diameter (m) for each bin at the 200 and 5000 seconds. The x -axis was the bin number from 1 to 100. Panel (c) represented the number density for each bin (bin 1-10 in red circle, bin 21-40 in orange triangle, bin 41-60 in green square, bin 61-80 in light blue star, and bin 81-100 in blue diamond) at the 0, 200, 1000, 3000, and 5000 seconds. 133

Figure 3.7 The illustration of the aspect ratio increase over certain time steps due to vapor diffusional growth for two ice particles with an initially small sphere (left) and an initially large one (right). While the increase in volume (in shaded green) is bigger for the initially larger particle ($dV_L > dV_S$), the relative increase in volume (dV/V) is larger for the smaller sphere. This new volume is distributed over the a and c axes by inherent growth ratio $\Gamma(T)$, causing a larger increase in aspect ratio for the initially smaller sphere. (*This plot was reproduced from the Figure 3. in Sheridan et al. 2009*). 134

Figure 3.8 The calculation results of (a) the 3rd-moment, (b) the bulk aspect ratio, (c) the bulk adaptive growth ratio, and (d) the mean volume diameter with the initial mean volume diameters of $1\ \mu\text{m}$ (in solid-green) and $10\ \mu\text{m}$ (in dash-red) both with the bulk 3-moment method. For these calculations, the environmental conditions were

the same to Figure 3.2.	135
Figure 3.9 The calculation results of (a) the 3 rd -moment, (b) the bulk aspect ratio, and (c) the bulk adaptive growth ratio for shape ice with the bin (in solid-black), bulk-2M (in dotted-green), and bulk-3M (in dash-red) methods, as well as for spherical ice with the bulk method (in solid-blue). For these calculations, $T=266\text{K}$, $P=800\text{ hpa}$, $\Delta Q_{vi}=5\times 10^{-5}\text{ kg kg}^{-1}$, and $\Gamma(T)=2.0$	136
Figure 3.10 The shaded contour plot of ice optical depth (τ_i) against the adaptive growth ratio (ζ , x -axis) and solar zenith angle (θ_s , y -axis). In this calculation, the ice equivalent diameter (D_i) was assumed to be $100\ \mu\text{m}$, $Q_i = 4.71\times 10^{-6}\text{ kg}$, $\lambda_i = 4.93\times 10^4\text{ m}^{-1}$, $N_i = 10^4\text{ m}^{-3}$, $\alpha_i = 3$, $z = 10^4\text{ m}$, and $\rho_i = 900\text{ kg m}^{-3}$	137
Figure 4.1 The model domain setup and terrain height (m) for C3VP case.	137
Figure 4.2 The simulation results of accumulated precipitation (mm) for (a) Sphere-2M, (b) Shape-2M, (c) Shape-3M runs, and a time series plot of domain-averaged precipitation intensity (mm hr^{-1}) depicted in (d) separately for Sphere-2M (in solid blue), Shape-2M (in dotted-green), and Shape-3M (in dash-red) runs over the inner domain within the simulation period from 06Z 21 January to 00Z 23 January 2007. The cross and star symbols represented the locations of the Centre for Atmospheric Research Experiments (CARE, 44.23°N , 79.78°W) site and the King City radar (43.96°N , 79.57°W).....	138
Figure 4.3 Snapshots of horizontal distributions of vertically maximum radar reflectivity (dBZ) at 00Z 22 January 2007 derived from the model simulation results of (a) Sphere-2M, (b) Shape-2M, and (c) Shape-3M runs, and the observation of the C-band King City radar depicted in (d). <i>The radar measurement was provided by Dr. Takamichi Iguchi and Dr. Jainn-Jung Shi at NASA/GSFC</i>	139
Figure 4.4 Latitudinal averaged of radar reflectivity (dBZ) by altitude (km) derived from the (a) Sphere-2M, (b) Shape-2M, and (c) Shape-3M simulation results at 00Z 22 January 2007. <i>Panel(d) indicated the measurement of King City radar which was provided by Dr. Takamichi Iguchi and Dr. Jainn-Jung Shi at NASA/GSFC</i>	140
Figure 4.5 Normalized contoured frequency with altitude (km) diagram of radar reflectivity derived from the simulations of the (a) Sphere-2M, (b) Shape-2M, (c) Shape-3M, and the measurement of the (d) King City radar from the period of 00Z	



22 January to 12Z 22 January 2007. The correlation (R) for each panel was determined against to the observation and the overlay black dash lines were the contour edges equal to 0.005, 0.2, 0.5, and 1 of the results in (d). *The radar measurement was provided by Dr. Takamichi Iguchi and Dr. Jainn-Jung Shi at NASA/GSFC.* 141

Figure 4.6 The vertical profiles of the simulated pristine ice aspect ratios ($\phi_i > 1.05$ for columnar, $\phi_i < 0.95$ for planar, otherwise for spherical crystals in orange) averaged by longitude within the latitude between 43.5°N and 44.5°N over the inner-domain for the (a) Shape-2M and (b) Shape-3M runs from the simulating period at (1) 22Z 21 January, (2) 00Z 22 January, (3) 02Z 22 January, to (4) 04Z 22 January 2007. The overlay black dash line was for the averaged ambient temperature (°C) and the y-axis denoted the altitude in km. 142

Figure 4.7 The vertical profiles of the inner-domain-averaged mixing ratio (kg m^{-3}) from 06Z 21 to 00Z 23 January for cloud droplets (Q_c), rain drops (Q_r), pristine ice (Q_i), snow-aggregates (Q_s), graupel (Q_g), and hail (Q_h) separately for the Sphere-2M (in solid blue), Shape-2M (in dotted green), and Shape-3M (in dash red) runs. The y-axis denoted the altitude in km. 143

Figure 4.8 Same as Figure 4.7 but for number concentration (m^{-3}). 143

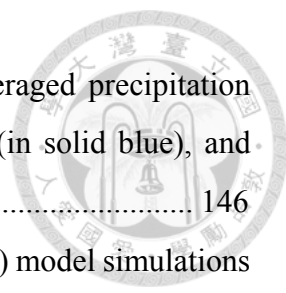
Figure 4.9 Same as Figure 4.7 but for effective radius (μm). 144

Figure 4.10 Same as Figure 4.7 but for mixing ratio change rates ($\text{kg kg}^{-1}\text{s}^{-1}$) of pristine ice. $QIMii$ for multiplication, $QVDvi$ for deposition growth, $QCNis$ for aggregation to snow-aggregates, $QNDvi$ for deposition-nucleation, $QFZci$ for cloud droplets freezing, and $QRMci$ for riming growth. 144

Figure 4.11 The time series plots of the inner-domain-averaged surface radiation fluxes (in W m^{-2}) for (a) the upwelling shortwave flux (in negative), (b) the down welling shortwave flux, (c) the upwelling longwave flux (in negative), and (d) the down welling longwave flux separately for Sphere-2M (in solid blue), Shape-2M (in dotted green) and Shape-3M (in dash red) runs. Panels (1) were the differences compared to the result of Sphere-2M run. 145

Figure 4.12 The model domain setup and terrain height (m) for DIAMET case. 146

Figure 4.13 The simulation results of accumulated precipitation (mm) for (a) Sphere-2M,



and (b) Shape-3M runs, and a time series plot of domain-averaged precipitation intensity (mm hr^{-1}) depicted in (c) separately for Sphere-2M (in solid blue), and Shape-3M (in dash red) runs over the inner domain. 146

Figure 4.14 The time series plots of precipitation rate (mm hr^{-1}) for (a) model simulations (Sphere-2M in solid blue and Shape-3M in dash red) and (b) ground-based observation (in black bar) at the Chilbolton Facility for Atmospheric and Radio Research site (CFARR, 51.15°N , 1.44°W). *The ground-based rainfall observation was provided by Dr. Christopher Dearden at University of Manchester.*..... 147

Figure 4.15 Precipitation rate in mm hr^{-1} for the (a) Sphere-2M, (b) Shape-3M model results, and (c) estimated from the ground-based S-band Chilbolton Advanced Meteorological Radar (CAMR) observation at 14Z 29 November 2011. The red-cross spot was the location of the CAMR site, and the dash black square was corresponding to the model inner domain. *Panel (c) was provided by Dr. Christopher Dearden at University of Manchester.*..... 147

Figure 4.16 Same as Figure 4.15 but for the time period of 15Z. 148

Figure 4.17 Same as Figure 4.15 but for the time period of 16Z. 148

Figure 4.18 The plots of radar reflectivity (dBZ) derived from the Shape-3M simulation result at an altitude of 2 km above ground level with a solid black line for the horizontal flight track and a dash black line for the corresponding cross section in (c). Panel (b) depicted the CAMR radar observation in the scanning mode of PPI at 1351 UTC with an elevation angle of 0.5° and the azimuth angles from 283.20° to 292.95° . Panel (d) was for the RHI scanning mode at 1352 UTC with an averaged elevation angle of 7.483° and a fixed azimuth angle of 283° . *The radar measurement was provided by Dr. Christopher Dearden at University of Manchester.*..... 149

Figure 4.19 Same as Figure 4.18 but at the period of 15.5Z for the model result in (a) and (c). Panel (b) depicted the CAMR radar observation in the scanning mode of PPI at 1525 UTC with an elevation angle of 0.5° and the azimuth angles from 280.02° to 379.79° . Panel (d) was for the RHI scanning mode at 1527 UTC with an averaged elevation angle of 0.95° and a fixed azimuth angle of 366.99° . *The radar measurement was provided by Dr. Christopher Dearden at University of Manchester.* 150

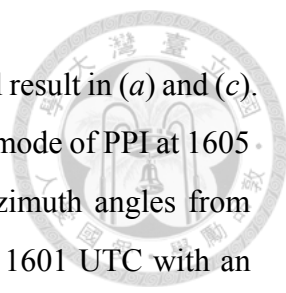


Figure 4.20 Same as Figure 4.18 but at the period of 16Z for the model result in (a) and (c). Panel (b) depicted the CAMR radar observation in the scanning mode of PPI at 1605 UTC with the elevation angles from 0.48° to 0.50° and the azimuth angles from 0.052° to 59.78°. Panel (d) was for the RHI scanning mode at 1601 UTC with an averaged elevation angle of 7.485° and a fixed azimuth angle of 44°. *The radar measurement was provided by Dr. Christopher Dearden at University of Manchester.*

..... 151

Figure 4.21 Normalized contoured frequency with altitude diagram of radar reflectivity derived from the inner-domain simulations of the (a) Sphere-2M and (b) Shape-3M runs from 06Z to 18Z 29 November 2011. The overlay black dash lines were the contour edges equal to 0.01, 0.1, and 0.3 of the results in (a)..... 152

Figure 4.22 The vertical shaded contour plots of the inner-domain-averaged by longitude within the flight track region in latitude between 50.5°N and 51.5°N for the pristine ice (a) mixing ratio (g kg^{-1}), (b) number concentration (L^{-1}), (c) mean volume diameter (μm), (d) bulk aspect ratio ϕ , (e) deposition heating rate (K hr^{-1}), and (f) riming heating rate (K hr^{-1}) at the simulating period of 15Z 29 November 2011 for the Shape-3M run. The overlay black dash line was for the averaged ambient temperature ($^{\circ}\text{C}$) and the y-axis denoted the altitude in km. 153

Figure 4.23 Same as Figure 4.22, but for the simulation period at 16Z..... 154

Figure 4.24 The scatter plots with mean vertical profiles (in black dash lines) of the ice number concentration (L^{-1} , x-axis) for the model (a) Sphere-2M (in blue), (b) Shape-3M run (in red), and (c) the aircraft observation (in black) with sampling data points (in grey bar) as a function of ambient temperature ($^{\circ}\text{C}$, y-axis) over the flight track area (50.5~51.5°N; -1~-3°W) from 14Z to 16.5Z. *The aircraft measurement data was provided by Dr. Christopher Dearden at University of Manchester.* 155

Figure 4.25 Same as Figure 4.24, but for the results of deposition heating rate (K hr^{-1} , x-axis). 156

Figure 4.26 The scatter plots with mean vertical profiles (in black dash lines) of the ice aspect ratio (x-axis) derived from the model Shape-3M run for (a) column ice alone (in red), (b) planar ice alone (in green), and (c) for the aircraft observation (in blue) with (d) sampling data points (in grey bar) as a function of ambient temperature ($^{\circ}\text{C}$,

	y-axis) within the diameter from 50 to 400 μm over the flight track area (50.5~51.5°N; -1~-3°W) from 14Z to 16.5Z. <i>The aircraft measurement data was provided by Dr. Christopher Dearden at University of Manchester.</i>	157
Figure 4.27	Ice crystals imaged by the 2D-S probe at 15:11Z from the aircraft observation. The circle hollow particles were cloud droplets. <i>The image was provided by Dr. Christopher Dearden at University of Manchester.</i>	158
Figure 4.28	The scatter plots with mean vertical profiles (in black dash lines) of the (a) bulk mean volume diameter (μm , x-axis) and (b) apparent density (kg m^{-3} , x-axis) of pristine ice as a function of ambient temperature ($^{\circ}\text{C}$, y-axis) from the Shape-3M run over the flight track area (50.5~51.5°N; -1~-3°W) from 14Z to 16.5Z.	158
Figure 4.29	The vertical profiles of the inner-domain-averaged in mixing ratio (kg m^{-3}) within the period from 06Z to 18Z 29 November 2011 for cloud droplets (Q_c), rain drops (Q_r), pristine ice (Q_i), snow-aggregates (Q_s), graupel (Q_g), and hail (Q_h) separately for the Sphere-2M (in solid blue) and the Shape-3M (in dash red) runs. The y-axis denoted the altitude in km.....	159
Figure 4.30	Same as Figure 4.29 but for number concentration (m^{-3}).	159
Figure 4.31	Same as Figure 4.29 but for effective radius (μm).	160
Figure 4.32	Same as Figure 4.29 but for mixing ratio change rates ($\text{kg kg}^{-1}\text{s}^{-1}$) of pristine ice. QIM_{ii} for multiplication, QVD_{vi} for deposition growth, QCN_{is} for aggregation to snow-aggregates, QND_{vi} for deposition-nucleation, QFZ_{ci} for cloud droplets freezing, and QRM_{ci} for riming growth.	160
Figure 4.33	Time series of the regional averaged surface radiation fluxes (in W m^{-2}) around CFARR site within 0.05° for (a) the upwelling shortwave flux (in negative), (b) the down welling shortwave flux, (c) the upwelling longwave flux (in negative), and (d) the down welling longwave flux separately for Sphere-2M (in solid blue) and Shape-3M (in dash red) runs. Panels (I) were the differences between two model runs.	161

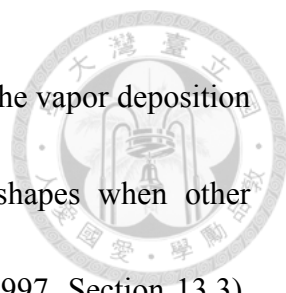


1. Introduction

With increasing computer power in recent years, cloud processes continue to be simulated in finer resolutions, and explicit microphysics schemes are required for better representing cloud and precipitation processes in grid-scale. But traditional explicit microphysics schemes still need improvements in the physical representation of ice-phase microphysics and in the numerical approach to represent the evolution of hydrometeor size distributions (Tao et al. 2012). The ice-phase microphysics representation contains many uncertainties related to the complex shapes of ice crystals, while the traditional bulk approaches applied a not so realistic representation of particle size spectrum. These subjects will be introduced in the next two sections, followed by some brief illustrations of different treatments of ice crystal in current microphysics schemes of the WRF (Weather Research and Forecasting) model. The last section will discuss the motivation of this study.

1.1 Ice crystal habits


Ice crystals in the upper troposphere are considered important to global radiation budget and cloud microphysics structure (McFarquhar et al. 2000; Jakob 2002). The wide variety of ice crystal shapes may introduce many uncertainties for numerical



models to evaluate the impact of ice-phase processes. For example, the vapor deposition growth rates of ice crystals can differ significantly with their shapes when other conditions being equal (Cotton et al. 1982; Pruppacher and Klett 1997, Section 13.3).

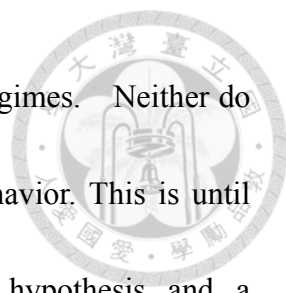
Different shapes of ice particles result in a diversity in terminal velocity-dimension (v - D) and mass-dimension (m - D) relationships (Mitchell 1996; Heymsfield et al. 2007). Furthermore, the ice crystal shape affects the cloud radiation flux by its oriented cross-section (e.g., Kinne and Liou 1989; Chou et al. 2002) and optical scattering phase function (e.g., Takano and Liou 1989; Yang and Fu 2009). Despite the important role that ice crystal shape plays, it remains difficult for cloud models to capture its variation well due to a lack of observational constraints and physical understanding.

The shapes of ice crystal, commonly referred to as the growth habits, can be characterized to the first degree by the ratio of the two axis lengths a and c (i.e., the aspect ratio $\phi \equiv c/a$). The c (principal) axis is the semi-dimension perpendicular to the basal faces, whereas the a (lateral) axis is the semi-dimension toward a corner of the hexagon (Pruppacher and Klett 1997, Section 2.2). **Figure 1.1** shows schematics of the two basic types of pristine ice crystals using spheroidal representation: The prolate to represent columnar ice and the oblate to represent the planar ice. The ice growth habit mainly depends on temperature and partially on supersaturation based on laboratory and *in-situ* data (e.g., Hallet and Mason 1958; Kobayashi 1961, a diagram example as



shown in **Figure 1.2**). These data suggest three transitions of the primary habits variation with decreasing temperature from plate to column near -4°C , back to plate near -9°C , and then switch to column again near -22°C . Although a recent habit diagram suggested by Bailey and Hallet (2009) claimed that plates tend to occur more often than columns at temperature below -22°C , these classical ice habit pictures remain valid for $T > -22^{\circ}\text{C}$. The secondary habits are modifications of the primary habits and are mainly determined by the excess vapor density (ambient minus crystal surface). Once ice crystals grow into regions of high supersaturation, the columnar crystals tend to become needles around -6°C , and the planar crystals easily evolve into dendrites at about -15°C , as well as rosette and polycrystals forming at temperature below -22°C .

Prior cloud modeling studies often utilized a fixed m - D and v - D relationships with independent coefficients for specific crystal habits to explore the impact of ice shape (e.g., Ji and Wang 1999; Harrington et al. 1995; Avramov and Harrington, 2010). However, these approaches merely predict the mass content of ice crystal, besides, the growth history of crystal is ignored meaning that crystal shape is not a prognostic but a diagnostic variable as determined by coefficients derived from *in-situ* data. Though Straka and Mansell (2005) could track two types of ice crystal habits diagnosed from ambient temperature, their aspect ratio and m - D relationship were held constant throughout the simulations. Thus, these simplified methods are not able to simulate the



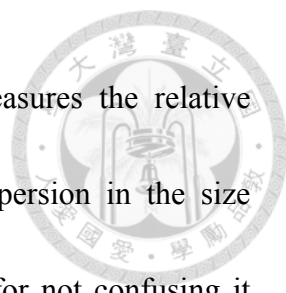
slow switch of ice habits when the crystals enter different growth regimes. Neither do they link directly between crystal shapes and ice mass growth behavior. This is until Chen and Lamb (1994a) applied an axes mass-redistribution hypothesis and a spheroidal shape approximation to form a theoretical basis of parameterization for ice crystal habits. Their method allowed crystal shapes to evolve in a realistic way and also considered the feedback between the changes in aspect ratio and diffusional mass growth. Hashino and Tripoli (2007) and Harrington et al. (2013a) took their approach and developed their own adaptive habit methods separately in a hybrid-bin and a two-moment bulk microphysics models (further details given in Section 1.4).

1.2 Bulk approaches

Both bulkwater and bin methods have been used for to resolve grid-scale cloud microphysical processes in the numerical models. However, with the advantage of computational efficiency, the bulk method continues to be a more practical approach than the bin method that is applied in regional models. A typical bulk scheme represents the size spectra of a hydrometeor category x by a three-parameter gamma distribution function of the form

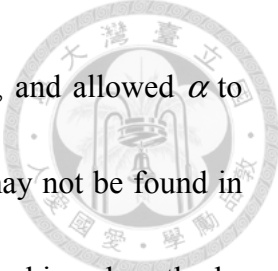
$$N_x(D_x) = N_{0x} D_x^{\alpha_x} e^{-\lambda_x D_x}, \quad (1.1)$$

where N_{0x} , λ_x , and α_x are the intercept, slope, and spectral index, respectively. The



parameter α is commonly called the shape parameter which measures the relative abundance of the small versus large particles or the spectral dispersion in the size spectrum of hydrometeor. But it is called the spectral index here for not confusing it with the ice crystal shape. This parameter (α) is often assumed as a constant value. If it is assigned as zero, and then (1.1) reduces to the Marshall-Palmer distribution which is commonly adopted in cloud microphysical schemes and radar reflectivity calculations.

Variation of the size distribution is calculated by predicting the changes to these parameters according to the prognostic changes in the moments of the distribution function. For instance, the traditional one-moment schemes exclusively assumed a stiff inverse-exponential distribution functions that N_{0x} and α_x are held constant and only predicts the mass content of the hydrometeor which can be used to derive λ_x (e.g., Lin et al. 1983; Tao and Simpson 1993). For the two-moment schemes, both mass content and number concentration are predicted and this permits the size spectrum to evolve somewhat more flexibly because both λ_x and N_{0x} are allow to vary (e.g., Morrison et al. 2005; Thompson et al. 2008). Although several studies (e.g., Morrison et al. 2009) have shown the superiority of the two-moment approach in considering the effect of size sorting (i.e., diffusional growth, breakup, self-collection, and so on), they need to fix the parameter α_x . Clark (1974) is probably the first that developed a 3-parameter gamma




distribution scheme by tracking the zeroth, first and third moments, and allowed α to vary between 3 to 400 (but he indicated that values larger than 10 may not be found in nature). He was able to obtain results in good agreement with the binned methods.

Milbrandt and Yau (2005a) pointed out that α_x significantly affects the rates of size sorting (e.g. instantaneous growth and sedimentation). In addition to the moments of mass and number, they proposed a third moment -- the radar reflectivity factor -- which is proportional to the sixth power of size, and developed a closure technique for the three-moment parameterization to allow the shape of the size distribution to evolve freely (Milbrandt and Yau 2005b). Their idealized hailstorm simulations indicated that the evolution of the surface precipitation rate is notably different between the three-moment and two-moment schemes.


1.3 Microphysics schemes in WRF

There are a suite of cloud microphysics schemes in the WRF model version 3.4.1 to be applied in this study. As summarized in **Table 1**, the Kessler, Purdue-Lin, WSM3/WSM5/WSM6, Eta_MP, Goddard, and SBU-Lin are one-moment schemes which tracks the mass mixing ratio for each hydrometeor category. The Thompson, Morrison, and WDM5/WDM6 are semi-two-moment schemes which track the mass concentration, but the predictions of number concentration are limited to a few specific



hydrometeors. The Milbrandt and Yau scheme and the NSSL scheme are fully two-moment schemes with the prognostic variables for mixing ratio and number concentration. In addition to mass and number moments, WDM5/WDM6 and NSSL schemes can track the number concentration of cloud condensation nuclei (CCN) to allow for a certain degree of aerosol-cloud interactions. For ice microphysics, SBU-Lin and NSSL schemes are also separately predict ice riming intensity and graupel density. The former scheme includes the effects of partially rimed particles using a diagnostic riming intensity as well as functional forms of the m - D , A - D and v - D relationships, while the latter one tracks the volume moment of graupel during riming growth.

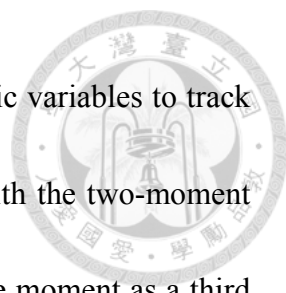
As for cloud ice crystals, the earliest Kessler scheme only considered warm cloud processes. Then, a simple ice scheme WSM3 was added to treat cloud/rain water below freezing point as ice/snow water. Although cloud ice has been added as a separate hydrometeor category afterwards in WSM5/WSM6, Eta_MP, Goddard, WDM5/WDM6, and SBU-Lin schemes, no size distribution information was imposed. A major feature of cloud ice schemes in WSM/WDM is their using fixed relations of N - m , D - m , and v - D pertaining to a particular crystal type of “single bullets” to diagnose its ice number concentration, equivalent diameter, and terminal velocity from the ice mass content. The other schemes mostly employ a mean terminal velocity of falling ice as proposed by Heymsfield and Donner (1990) to calculate sedimentation of cloud ice. The ice crystal



shapes are spherical in most two-moment schemes, whereas snow categories are optionally assumed a non-spherical shape with fixed relationships between mass and diameter based on observations in Thompson and Milbrandt schemes. For bulk density, a fixed value of 500 kg m^{-3} for cloud ice is adopted in most of the two-moment schemes, except for 840 kg m^{-3} used in the Milbrandt scheme. Graupel density is predicted mainly by calculating rimed-ice density during riming growth in NSSL scheme. For snow category, Milbrandt scheme used two constants derived from observations to account for the relation of mass and diameter, while the snow density varies inversely with diameter in Thompson scheme.

1.4 Motivation

As the current cloud microphysics schemes in WRF and most other models do not consider the free evolution of ice crystal shape, and yet many studies indicated that ice crystal shape is an important factor in cloud microphysical and radiative processes. Chen and Lamb (1994a, hereafter CL94) developed a theory-based method to describe ice crystal shape evolution for detailed bin models. This study intends to follow their approach and develop an adaptive growth habit method to track the evolution of ice crystal shape and density with bulkwater parameterization. Note that Harrington et al. (2013a,b) already proposed an adaptive ice habit parameterization in a bulk



microphysics parcel model based on CL94, they used four prognostic variables to track the ice aspect ratio by predicting the a - and c - axes individually with the two-moment approach. This study will predict a new variable called crystal shape moment as a third moment. This shape moment also allows us to diagnose the cross-section area, which benefits the calculation of collection kernels and radiative transfer. Moreover, ice crystal density has certain impact on many microphysical processes, but currently this parameter is kept as constant in most cloud schemes. This study will propose another new variable of crystal volume moment for the prediction of bulk ice density. Furthermore, both the ice adaptive habit parameterization and the three-moment closure method developed in this study will be implemented into the WRF model for the simulation using real cases.

Details of the bulk adaptive habit parameterization and a new full set of microphysics scheme will be described in Chapter 2. Chapter 3 will present some validations in a zero-dimension model (i.e. parcel model). In Chapter 4, the new schemes are implemented into the WRF model and applied to two real-case studies conducted in Canada and England. Summary and future perspective will be given in Chapter 5.



2. Methodology

The methodology developed in this study mainly included the development of a theoretical ice crystal adaptive growth habit bulkwater parameterization and a new multi-moment microphysics scheme.

2.1 An adaptive growth habit bulkwater parameterization

The shape of ice crystal is typically represented, to the first order, as the ratio of c - and a - lengths, and these two axes were found by many observations (e.g., Heymsfield and Knollenberg 1972; Jayaweera and Ohtake 1974) to be in an exponential relationship as follows (cf. CL94):

$$c = \eta a^\beta. \quad (2.1)$$

where η and β are positive constants that have specific values corresponding to the given crystal types and environment conditions. These fixed-form equations were almost exclusively used for describing ice crystal shapes in some earlier modeling studies until a theory-based parameterization was proposed by CL94. They theoretically derived an equation of

$$\frac{dc}{da} = \Gamma(T)\phi, \quad (2.2)$$

where $\Gamma(T)$ is the inherent growth ratio and $\phi (\equiv c/a)$ is the aspect ratio. The parameter

$\Gamma(T)$ is the ratio of the condensation coefficients for the basal and prism faces driven by surface kinetic processes and is primarily a function of temperature. Equation (2.2)

expressed in an integrated form ($c \propto a^{\Gamma(T)}$) is identical to (2.1), with $\Gamma(T)$ corresponds to its exponent. Though $\Gamma(T)$ was measured in the laboratory, CL94 found that it was quite consistent to the exponent in (2.1) obtained from observations within 0°C to -30°C (see their Fig. 3). Upon their mass-redistribution hypothesis, the depositional growth mass is added onto the crystal faces varied in different temperature regimes through the relation (2.2). Furthermore, with the links to the change rates of aspect ratio and mass growth, CL94 provides a realistic approach to simulate the variation of ice crystal shape under different environment conditions. Note that rosette and polycrystals which commonly present at ambient temperatures below -22°C may need a separate parameterization scheme and are not treated in this study.

2.1.1 Bulk ice shape and volume moments

In contrast to the inherent growth ratio which is a temperature-dependent function, this study furthered CL94's approach and defined the exponent in (2.1) as an adaptive growth ratio of β which retains the growth history of ice crystals in the new parameterization. Applying an isometric growth limitation for small crystals ($a = c$ when radius of r was smaller than a threshold size of r_0) has been done in CL94, η in (2.1)

was close to

$$\eta \cong r_0^{1-\beta}. \quad (2.3)$$



Then adopting the spheroidal shape approximation, the volume of ice particle was

$$V = \frac{4}{3}\pi a^2 c = \frac{4}{3}\pi r^3, \quad (2.4)$$

where r is the spherical equivalent radius (i.e. the radius of a spherical particle of the same volume). Substituting (2.3) and (2.4) into (2.1), the a - and c - lengths were separately given by

$$a = r_0^{\frac{\beta-1}{\beta+2}} r^{\frac{3}{\beta+2}}; \quad (2.5a)$$

$$c = \eta a^\beta = r_0^{\frac{-2(\beta-1)}{\beta+2}} r^{\frac{3\beta}{\beta+2}}. \quad (2.5b)$$

Let (2.5b) be divided by (2.5a), the aspect ratio was transformed into a function of

$$\phi \equiv \frac{c}{a} = \left(\frac{r}{r_0}\right)^{\frac{3(\beta-1)}{\beta+2}} \equiv \left(\frac{r}{r_0}\right)^{3\zeta}, \quad (2.6)$$

where $\zeta = (\beta-1)/(\beta+2)$. By relating β to ϕ , ice aspect ratio can be determined by knowing β alone instead of individually tracking the two axis lengths. As β goes larger than 1 ($\zeta > 0$), smaller than 1 ($\zeta < 0$), and equal to 1 ($\zeta = 0$), the ice crystal shape will be classified as columnar ($\phi > 1$), planar ($\phi < 1$), and spherical ($\phi = 1$), respectively.

For a bulk method, the aspect ratio of particles are assumed to follow the power law (2.1), but the exponent is not determined by temperature as in (2.2) but rather changes gradually from its earlier value by adapting to the new ambient temperature

which determines $\Gamma(T)$. So, this “adaptive growth ratio” parameter for a distribution of ice particles is different from $\Gamma(T)$, and is defined here as β . However, the bulk adaptive growth ratio β is not an extensive property and thus cannot be conserved during spatial advection. Alternatively, we defined the bulk aspect ratio as a “volume-weighted” (or 3rd-moment weighted) shape parameter and introduced as the first new variable of the bulk ice shape moment in our parameterization:

$$M_\phi = \int \phi D^3 N(D) dD = \int \left(\frac{D}{D_0} \right)^{3\zeta} D^3 N(D) dD = D_0^{-3\zeta} M_{3\zeta+3}, \quad (2.7)$$

where $M_k \equiv \int D^k N(D) dD$ is the k th moment of the size distribution. Ice density is also not an extensive property, but can be diagnosed from the mass mixing ratio and the volume of ice particles. In the same way, we defined the ice volume as another new variable of the bulk ice volume moment in diameter D ,

$$M_V = \frac{\pi}{6} \int D^3 N(D) dD = \frac{\pi}{6} M_3. \quad (2.8)$$

Note that, now the third moment of the size distribution is represented by M_3 and becomes a tracking variable which is not used in determining the size distribution parameters in (1.1). Similar approaches were also employed in the recent studies of Mansell et al. (2010) and Milbrandt and Morrison (2013) for the prediction of bulk density. These two newly introduced bulk moments are advected along with the mass mixing ratio and other moments, so the conservation of moments can be guaranteed



throughout simulations.

2.1.2 Deposition growth

Ice crystals were normally assumed to be spherical in traditional bulk-water parameterization when calculating their deposition growth

$$\frac{dm_i}{dt} = 2\pi D_i f_{vi} D_v \Delta\rho_v, \quad (2.9a)$$

where D_i is the spherical diameter, D_v the diffusivity of water vapor in air, f_{vi} the ventilation effect, and $\Delta\rho_v$ is the excess vapor density. Yet, according to the classical capacitance model (Byers 1965), the actual growth equation with the shape consideration is

$$\frac{dm}{dt} = 2\pi C_i f_{vi} D_v \Delta\rho_v, \quad (2.9b)$$

where C_i is the electrostatic capacitance in diameter and the ratio of C_i/D_i in these two equations is a strong function of ice aspect ratio (see **Figure 2.1**). For a bulk method, the enhancement of the deposition growth rate due to ice shape effect is parameterized by integrating C_i/D_i over the whole size spectrum as shown below.

$$\int \frac{C_i}{D_i} N_i(D_i) dD_i / \int N_i(D_i) dD_i. \quad (2.10)$$

Observational results showed that the aspect ratio of an ice crystal varied with its size.

Theoretical analysis of CL94 demonstrated that this relationship depends on the inherent growth ratio and they also showed that



$$d \ln \phi_i = \gamma d \ln V_i. \quad (2.11)$$

This equation can be rewritten as (note that γ was replaced with ζ used for this study),

$$\phi_i = \left(\frac{V_i}{V_{i0}} \right)^{1/\zeta}, \quad (2.12)$$

where V_{i0} is the maximum volume of the ice crystal that grow isometrically (i.e. $\frac{4\pi}{3}r_0^3$)

and ζ is the function of adaptive growth ratio. Note that when ice crystals are still very small (diameter roughly less than $6 \mu\text{m}$), their shapes retain as isometric (i.e., $\phi_i = 1$).

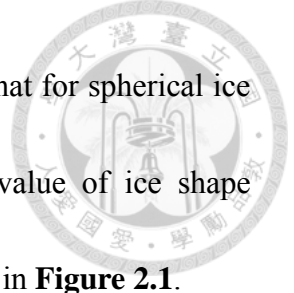
Since we know the dependence of C_i/D_i on ϕ_i (cf. CL94), it can be converted to a function of V_i/V_{i0} and β . Following the method of Chen et al. (2013), a matrix of C_i/D_i values can be obtained by systematically varying V_i/V_{i0} and β , which then can be fitted into the following simple function form to allow analytical solution to be derived for (2.10):

$$\frac{C_i}{D_i} \cong \left(\frac{V_i}{V_{i0}} \right)^{f(\beta)}. \quad (2.13)$$

where the power law coefficient $f(\beta)$ was derived by statistical fitting into the form:

$$f(\beta) = (\beta - 1) \cdot (a_1 + a_2\beta + a_3\beta^2). \quad (2.14)$$

For planar ice ($\beta < 1$; represented by oblate spheroids), $a_1 = -0.13779757$, $a_2 = 0.083060608$, $a_3 = 0.049632531$, and the coefficient of determination (R^2) for the fitting was 0.9793; for columnar ice ($\beta > 1$; represented by prolate spheroids), $a_1 = -0.069605658$, $a_2 = 0.12556528$, $a_3 = -0.026643093$, and the R^2 for the fitting was



0.9548. Note that the specific form in (2.14) was chosen to ensure that for spherical ice crystal ($\beta=1$) the shape enhanced factor reduced to unity. The value of ice shape enhanced factor with respect to the adaptive growth ratio was shown in **Figure 2.1**.

To get the final solution for (2.10), we need to convert the variable V_i in (2.13) to diameter D_i so that

$$\frac{C_i}{D_i} \cong \left(\frac{D_i^3}{D_{i0}^3} \right)^{f(\beta)} = \left(\frac{D_i}{D_{i0}} \right)^{3f(\beta)}, \quad (2.15)$$

with D_{i0} set to 6 μm according to observational evidences (cf. Pruppacher and Klett 1997, Section 2.2). The modification factor for (2.10) can finally be derived as

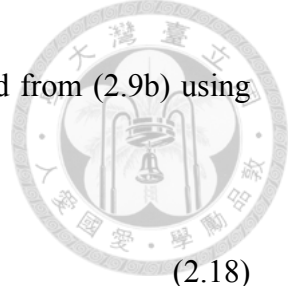
$$\int \left(\frac{D_i}{D_{i0}} \right)^{3f(\beta)} N_i(D_i) dD_i / \int N_i(D_i) dD_i = \frac{M_{3f(\beta)}^i}{D_{i0}^{3f(\beta)} M_0^i}. \quad (2.16)$$

Note that, for spherical particles, (2.16) reduces to unity. Such a shape-induced growth modification can be applied safely to cloud ice (here defined as pristine ice crystals) but not to snow because, by definition, snow includes ice crystal aggregates whose deposition growth not necessarily follow (2.13).

Prediction of bulk ice aspect ratio requires a prognostic equation for the bulk ice shape moment introduced in (2.7). So we differentiated M_ϕ with respect to time, and a rate equation was derived as follows:

$$\frac{dM_\phi}{dt} = \int \frac{d(\phi_i D_i^3)}{dt} N_i(D_i) dD_i = \int \frac{d\phi_i}{dt} D_i^3 N_i(D_i) dD_i + \int \frac{dD_i^3}{dt} \phi_i N_i(D_i) dD_i, \quad (2.17)$$

where the $d\phi_i$ term can be obtained from its relationship with dV_i in (2.11), and the rate



change in ice volume moment for deposition growth can be derived from (2.9b) using the mass-volume-density relationship:

$$\frac{dM_V}{dt} = \frac{1}{\rho_{i,dep}} \frac{dm}{dt} \equiv A_{dep} C_i, \quad (2.18)$$

where $A_{dep} \equiv 2\pi D_v f_{vi} \Delta\rho_v / \rho_{i,dep}$, dm/dt is the deposition growth rate of mixing ratio in (2.9b), and $\rho_{i,dep}$ is the effective ice deposition density as defined and parameterized by CL94,

$$\rho_{i,dep} = 910 \exp\left[\frac{-3 \cdot \max(\Delta\rho_v - 5 \times 10^{-5}, 0)}{\Gamma(T)}\right]. \quad (2.19)$$

From (2.15), we obtained $C_i = (D_i/D_{i0})^{3f(\beta)} D$. So the change rate of ice shape moment in (2.17) can be written as

$$\begin{aligned} \frac{dM_\phi}{dt} &= \frac{6A_{dep}}{\pi} (\gamma + 1) \int \left(\frac{D_i}{D_{i0}}\right)^{3f(\beta)} D_i \left(\frac{D_i}{D_{i0}}\right)^{3\zeta} N_i(D_i) dD_i \\ &= \frac{6A_{dep} (\gamma + 1)}{\pi D_{i0}^{3[f(\beta)+\zeta]}} M_{3f(\beta)+3\zeta+1} \end{aligned}, \quad (2.20)$$

and the change rate of ice volume moment in (2.18) is

$$\frac{dM_V}{dt} = \int \frac{1}{\rho_{i,dep}} \frac{dm}{dt} = \frac{A_{dep}}{D_{i0}^{3f(\beta)}} M_{3f(\beta)+1}, \quad (2.21)$$

With the prognostic equations for the ice shape moment and the ice volume moment, our parameterization enables the bulk shape and volume of ice crystal to be predicted. The volume-weighted mean aspect ratio can be defined as:

$$\bar{\phi}_i = \frac{\int \phi_i D_i^3 N_i(D_i) dD_i}{\int D_i^3 N_i(D_i) dD_i} = \frac{M_\phi}{M_3}. \quad (2.22)$$

The larger values of spectral index correspond to increasingly more narrow size distributions with the peak of the distribution curve approaching the mean diameter of the distribution (See **Figure 3.3**). Chen et al. (2013) demonstrated that, for a narrow size

distribution, the integrals in (2.22) can be simplified by replacing the diameter D_i with the mean (or modal) diameter. So, for large α_i values, one can get:

$$\phi_i = \left(\frac{D_i}{D_{i0}} \right)^{3\zeta} \Rightarrow \left(\frac{\overline{D_i^3}}{D_{i0}^3} \right)^\zeta = \left(\frac{M_3}{M_3^*} \right)^\zeta, \quad (2.23)$$

where $M_3^* = N_i D_{i0}^3$ and N_i is the number concentration (zeroth moment) of ice crystals.

For small α values, the above approximation needs to be modified. Given different conditions of the adaptive growth ratio (ζ varied from -0.4 to 0.4) and the spectral index (α_i varied from 0 to 50) against the corresponding aspect ratio in the range from 1.54×10^{-3} to 6.66×10^2 , the original fitting regression equation between (2.23) and (2.24)

$$\text{was } \left(\frac{M_3}{M_3^*} \right)^\zeta = 0.937 \times \left(\frac{M_\phi}{M_3} \right) - 0.291 \text{ with } R^2 \text{ of } 0.998 \text{ and absolute relative error of}$$

10.987%. The error above was mainly attributed to the large dispersion and deviation of the spectrum from the normal distribution when α_i is small. If the variation of α_i is limited within 5 to 50, the revised absolute relative error can reduce to less than 5%. If one requires a better accuracy, the following polynomial equation can be used instead,

$$f(\zeta, \alpha_i) = \frac{a + c\zeta + e\alpha_i + g\zeta^2 + i\alpha_i^2 + k\zeta\alpha_i}{1 + b\zeta + d\alpha_i + f\zeta^2 + h\alpha_i^2 + j\zeta\alpha_i}, \quad (2.24)$$

where $a = 0.99891855$; $b = 1.37997010$; $c = -0.57846829$; $d = 0.44399356$; $e = 0.44405825$; $f = 1.22795810$; $g = -0.67145947$; $h = -0.00015110$; $i = -0.00015185$; $j = -0.01506508$; $k = -0.01503099$, and the R^2 reaches 1.000. Applying the correction function, the values of bulk ice aspect ratio in (2.22) and (2.23) become almost identical to each other with an absolute error of 0.068%. The original and corrected data points were depicted in **Figure 2.2**. With this correction factor, the bulk adaptive growth ratio can be determined accurately at each time step through the equation below,

$$\bar{\beta} = \frac{1 + 2 \log \left(\frac{M_3}{M_3^*} \right)^{\frac{M_\phi}{M_3}}}{1 - \log \left(\frac{M_3}{M_3^*} \right)^{\frac{M_\phi}{M_3}}}. \quad (2.25)$$



Also, we can derive the bulk ice density at each time step by dividing ice mixing ratio by the volume moment, as shown below.

$$\bar{\rho}_i = \frac{Q_i}{M_V}. \quad (2.26)$$

The value of bulk ice density is in the range of 100 to 910 kg m⁻³. The role it plays is to reflect the indents, voids or hollows in the secondary growth habits developed under the fast growth conditions (i.e., high vapor density access). Higher supersaturation (vapor density access to be more exact) over ice results in the smaller bulk density, especially in the temperature region of dendrite. Hence the secondary ice growth habit is implicitly included in our approach as well.

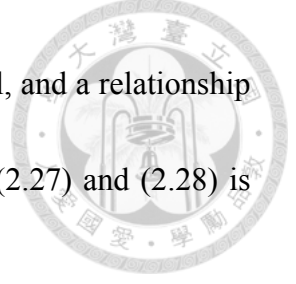
2.1.3 Riming growth

For the riming growth of pristine ice (which then convert to graupel), two differential forms of ice volume and aspect ratio are separately represented as follows,

$$dV_i = \frac{\pi}{6} D_{ia}^2 D_{ic} dD_{ia} + \frac{\pi}{6} D_{ia}^2 D_{ic}' dD_{ic}, \quad (2.27)$$

$$d\phi_i = D_{ia}^{-1} dD_{ic} - D_{ic} D_{ia}^{-2} dD_{ia}. \quad (2.28)$$

where D_{ic} and D_{ia} stand for the principal (major) and lateral (minor) axes of the ice crystal. The rate change of ice crystal shape through riming growth is referred to Chen and Lamb (1994b) which assumed all droplets are accreted along the short axis with a



fixed long-axis length. Hence, dD_{ic} should be zero for prolate crystal, and a relationship between ice volume and aspect ratio change rates simplified from (2.27) and (2.28) is obtained

$$d\phi_i = \frac{-3}{\pi D_{i0}^{3\zeta} D_i^{3g_\beta}} dV_i, \quad (2.29)$$

where $g_\beta = 3/(\beta+2)$. By considering the sweep cross-section for riming collection and taking into account the relationship between the change rates of ice volume and aspect ratio in (2.29), the change rates of moments during riming can be derived as the following: (1) the shape moment:

$$\begin{aligned} \frac{dM_\phi}{dt} &= \int \frac{d\phi_i}{dt} D_i^3 N_i(D_i) dD_i + \frac{6}{\pi} \int \frac{dV_i}{dt} \left(\frac{D_i}{D_{i0}} \right)^{3\zeta} N_i(D_i) dD_i \\ &= \frac{3\pi E_{ix} |\bar{v}_i - \bar{v}_x|}{4\pi \rho_{i,rim} D_{i0}^{3\zeta}} \iint D_i^{3\zeta} (D_{ia} + D_x)(D_{ic} + D_x) m_x(D_x) N_i(D_i) N_x(D_x) dD_i dD_x \\ &= \frac{3\pi \rho_w E_{ix} \Delta v_{ix}}{8\rho_a \rho_{i,rim} D_{i0}^{3\zeta}} \left[\begin{aligned} &D_{i0}^{-\zeta} M_{i,f_\beta+3\zeta} M_{x,3} + D_{i0}^{-2\zeta} M_{i,h_\beta+3\zeta} M_{x,4} + \\ &D_{i0}^\zeta M_{i,g_\beta+3\zeta} M_{x,4} + M_{i,3\zeta} M_{x,5} \end{aligned} \right] \end{aligned} \quad (2.30)$$

where $h_\beta = 3\beta/(\beta+2)$ and $f_\beta = 3(\beta+1)/(\beta+2)$; (2) The change rate for mixing ratio:

$$\begin{aligned} \frac{dm}{dt} &= \frac{\pi}{4} \iint |\bar{v}_i - \bar{v}_x| (D_{ia} + D_x)(D_{ic} + D_x) m_x(D_x) E_{ix} N_i(D_i) N_x(D_x) dD_i dD_x \\ &= \frac{\pi^2 \rho_w E_{ix} \Delta v_{ix}}{24\rho_a} \left[D_{i0}^{-\zeta} M_{i,f_\beta} M_{x,3} + D_{i0}^{-2\zeta} M_{i,h_\beta} M_{x,4} + D_{i0}^\zeta M_{i,g_\beta} M_{x,4} + M_{x,5} \right] \end{aligned} \quad (2.31)$$

(3) The change rate for number concentration of cloud drops is

$$\begin{aligned} \frac{dN}{dt} &= \frac{\pi}{4} \iint |\bar{v}_i - \bar{v}_x| (D_{ia} + D_x)(D_{ic} + D_x) E_{ix} N_i(D_i) N_x(D_x) dD_i dD_x \\ &= \frac{\pi E_{ix} \Delta v_{ix}}{4\rho_a} \left[D_{i0}^{-\zeta} M_{i,f_\beta} + D_{i0}^{-2\zeta} M_{i,h_\beta} M_{x,1} + D_{i0}^\zeta M_{i,g_\beta} M_{x,1} + M_{x,2} \right] \end{aligned} \quad (2.32)$$

where $x \in (c, r)$, c represents cloud droplet and r represents raindrop. The collection

efficiency (E_{ic}) is referred to Wang and Ji (2000). A table of E_{ic} for columnar ice in terms of different Reynolds number, Re , collecting cloud droplet with radius from 0 to 100 μm was constructed from their numerical results (see their Fig. 9). In addition, a riming threshold diameter of 100 μm is given. Ice riming density is adopted from Rasmussen and Heymsfield (1985) in the form of

$$\rho_{i,rim} = 300 \left[\frac{0.5 \times 10^6 D_c \cdot 0.6 \cdot \Delta V_{im}}{T_0 - T} \right]^{0.44} \quad (2.33)$$

where $T_0 = 273.15\text{K}$, D_c is the cloud droplet diameter in meter, and ΔV_{im} is the impact velocity in meter per sec.

For oblate crystal, dD_{ia} likewise is zero. A relationship between ice volume and aspect ratio change rates derived from (2.27) and (2.28) again is obtained

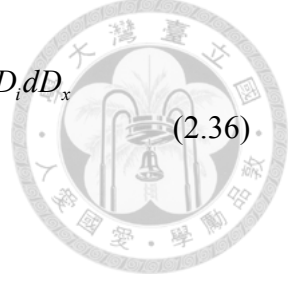
$$d\phi_i = \frac{6}{\pi D_{i0}^{3\zeta} D_i^{3g_\beta}} dV_i \quad (2.34)$$

Thus, the change rates of ice shape, mass, and number moments in consideration of collecting geometric cross-section for planar ice are derived below: (1) Shape moment:

$$\begin{aligned} \frac{dM_\phi}{dt} &= \int \frac{d\phi_i}{dt} D_i^3 N_i(D_i) dD_i + \frac{6}{\pi} \int \frac{dV_i}{dt} \left(\frac{D_i}{D_{i0}} \right)^{3\zeta} N_i(D_i) dD_i \\ &= \frac{12 \overline{|v_i - v_x|}}{\pi \rho_a \rho_{i,rim} D_{i0}^{3\zeta}} \iint D_i^{3\zeta} \frac{\pi}{4} (D_{ia} + D_x)^2 m_x(D_x) E_{ix} N_i(D_i) N_x(D_x) dD_i dD_x \quad (2.35) \\ &= \frac{\pi \rho_w E_{ix} \Delta v_{ix}}{2 \rho_a \rho_{i,rim} D_{i0}^{3\zeta}} \left[D_{i0}^{2\zeta} M_{i,2g_\beta+3\zeta} M_{x,3} + 2 D_{i0}^\zeta M_{i,g_\beta+3\zeta} M_{x,4} + M_{i,3\zeta} M_{x,5} \right] \end{aligned}$$

(2) The change rate for mixing ratio:

$$\begin{aligned}
\frac{dm}{dt} &= \frac{\pi}{4} \iint |\bar{v}_i - \bar{v}_x| (D_{ia} + D_x)^2 m_x(D_x) E_{ix} N_i(D_i) N_x(D_x) dD_i dD_x \\
&= \frac{\pi^2 \rho_w E_{ix} \Delta v_{ix}}{24 \rho_a} \left[D_{i0}^{2\zeta} M_{i,2g\beta} M_{x,3} + 2D_{i0}^\zeta M_{i,g\beta} M_{x,4} + M_{x,5} \right]
\end{aligned} \tag{2.36}$$



(3) The change rate for number concentration:

$$\begin{aligned}
\frac{dN}{dt} &= \frac{\pi}{4} \iint |\bar{v}_i - \bar{v}_x| (D_{ia} + D_x)^2 E_{ix} N_i(D_i) N_x(D_x) dD_i dD_x \\
&= \frac{\pi E_{ix} \Delta v_{ix}}{4 \rho_a} \left[D_{i0}^{2\zeta} M_{i,2g\beta} + 2D_{i0}^\zeta M_{i,g\beta} M_{x,1} + M_{x,2} \right]
\end{aligned} \tag{2.37}$$

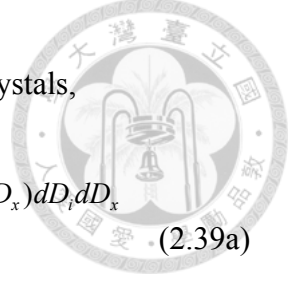
Another table of E_{ic} for plate ice collecting cloud droplet was also constructed from the Fig. 6 of Wang and Ji (2000) and a riming threshold diameter of $150 \mu\text{m}$. At last, the rate change of ice volume moment during riming growth is

$$\frac{dV_i}{dt} = \frac{1}{\rho_{i,rim}} \frac{dm}{dt} \tag{2.38}$$

where dm/dt is used (2.31) for columnar ice or (2.36) for planar ice, and $\rho_{i,rim}$ is from (2.33). The relationship between ice habit and its fall speed will be introduced later in Section 2.1.7. Therefore, the effects of ice habit onto geometric cross-section, collection efficiency, and fall speed have been considered during riming growth in the new parameterization.

2.1.4 Accretion rate by other particles

Different shapes of ice crystals would result in the variation in accretion rate by other large hydrometeors due to different geometric cross-section and fall speed. With this consideration, the rate change in the accretion of pristine ice shape, mass, and



number moments (their sink terms) are derived below. For prolate crystals,

$$\begin{aligned} \frac{dM_\phi}{dt} &= \frac{\pi E_{ix} |\bar{v}_i - \bar{v}_x|}{4 a_{mi} D_{i0}^{3\zeta}} \iint D_i^{3\zeta} (D_{ia} + D_x)(D_{ic} + D_x) m_i(D_i) N_i(D_i) N_x(D_x) dD_i dD_x \\ &= \frac{\pi E_{ix} \Delta v_{ix}}{4 \rho_a D_{i0}^{3\zeta}} \left[D_{i0}^{-\zeta} M_{i,f\beta+3\zeta+b_{mi}} + D_{i0}^{-2\zeta} M_{i,h\beta+3\zeta+b_{mi}} M_{x,1} + \right. \\ &\quad \left. D_{i0}^\zeta M_{i,g\beta+3\zeta+b_{mi}} M_{x,1} + M_{i,3\zeta+b_{mi}} M_{x,2} \right] \end{aligned} \quad (2.39a)$$

The accretion rate for mixing ratio is

$$\begin{aligned} \frac{dm}{dt} &= \frac{\pi}{4} \iint |\bar{v}_i - \bar{v}_x| (D_{ia} + D_x)(D_{ic} + D_x) m_i(D_i) E_{ix} N_i(D_i) N_x(D_x) dD_i dD_x \\ &= \frac{\pi a_{mi} E_{ix} \Delta v_{ix}}{4 \rho_a} \left[D_{i0}^{-\zeta} M_{i,f\beta+b_{mi}} + D_{i0}^{-2\zeta} M_{i,h\beta+b_{mi}} M_{x,1} + \right. \\ &\quad \left. D_{i0}^\zeta M_{i,g\beta+b_{mi}} M_{x,1} + M_{i,b_{mi}} M_{x,2} \right] \end{aligned} \quad (2.40a)$$

The accretion rate for number concentration is

$$\begin{aligned} \frac{dN}{dt} &= \frac{\pi}{4} \iint |\bar{v}_i - \bar{v}_x| (D_{ia} + D_x)(D_{ic} + D_x) E_{ix} N_i(D_i) N_x(D_x) dD_i dD_x \\ &= \frac{\pi E_{ix} \Delta v_{ix}}{4 \rho_a} \left[D_{i0}^{-\zeta} M_{i,f\beta} + D_{i0}^{-2\zeta} M_{i,h\beta} M_{x,1} + D_{i0}^\zeta M_{i,g\beta} M_{x,1} + M_{x,2} \right] \end{aligned} \quad (2.41a)$$

For oblate crystals, these rates are:

$$\begin{aligned} \frac{dM_\phi}{dt} &= \frac{\pi E_{ix} |\bar{v}_i - \bar{v}_x|}{4 a_{mi} D_{i0}^{3\zeta}} \iint D_i^{3\zeta} (D_{ia} + D_x)^2 m_i(D_i) N_i(D_i) N_x(D_x) dD_i dD_x \\ &= \frac{\pi E_{ix} \Delta v_{ix}}{4 \rho_a D_{i0}^{3\zeta}} \left[D_{i0}^{2\zeta} M_{i,2g\beta+3\zeta+b_{mi}} + 2 D_{i0}^\zeta M_{i,g\beta+3\zeta+b_{mi}} M_{x,1} + M_{i,3\zeta+b_{mi}} M_{x,2} \right] \end{aligned} \quad (2.39b)$$

The accretion rate for mixing ratio is

$$\begin{aligned} \frac{dm}{dt} &= \frac{\pi}{4} \iint |\bar{v}_i - \bar{v}_x| (D_{ia} + D_x)^2 m_i(D_i) E_{ix} N_i(D_i) N_x(D_x) dD_i dD_x \\ &= \frac{\pi a_{mi} E_{ix} \Delta v_{ix}}{4 \rho_a} \left[D_{i0}^{2\zeta} M_{i,2g\beta+b_{mi}} + 2 D_{i0}^\zeta M_{i,g\beta+b_{mi}} M_{x,1} + M_{i,b_{mi}} M_{x,2} \right] \end{aligned} \quad (2.40b)$$

The accretion rate for number concentration is



$$\begin{aligned}\frac{dN}{dt} &= \frac{\pi}{4} \iint |\bar{v}_i - \bar{v}_x| (D_{ia} + D_x)^2 E_{ix} N_i(D_i) N_x(D_x) dD_i dD_x \\ &= \frac{\pi E_{ix} \Delta v_{ix}}{4 \rho_a} \left[D_{i0}^{2\zeta} M_{i,2g\beta} + 2D_{i0}^{\zeta} M_{i,g\beta} M_{x,1} + M_{x,2} \right]\end{aligned}\quad (2.41b)$$

where $x \in (r, s, g, h)$ and r , s , g , and h represents for raindrop, snow-aggregates, graupel, and hail, respectively. The values of collection efficiencies (E_{ix}) used for interaction between two hydrometeor categories are listed in **Table 4**. The parameters of a_m and b_m are discussed in Section 2.1.6. Note that the habit and density of the remaining pristine ice are not changed during the accretion process.

2.1.5 Aggregation among pristine ice

For self-collection among pristine ice, it is hard to explicitly derive the conversion rate without tracking different types of ice crystals individually. A simple method referred to Cotton et al. (1986) with some modifications considering geometric cross-section for shaped ice crystals is adopted to estimate collection rate among a population of pristine ice. But the effects of size distribution and habit have not been explicitly considered in their study. Here, the conversion rates of mixing ratio and number concentration from pristine ice to aggregate are shown below for columnar ice:

$$\frac{dm}{dt} = \frac{\pi}{6} v_i E_{ii} X_{disp} \cdot Q_i N_i D_{i0}^{-\zeta} \bar{D}_i^{f\beta} \quad (2.42a)$$

$$\frac{dN}{dt} = \frac{\pi}{6} v_i E_{ii} X_{disp} \cdot N_i^2 D_{i0}^{-\zeta} \bar{D}_i^{f\beta} \quad (2.43a)$$

and for planar ice:

$$\frac{dm}{dt} = \frac{\pi}{6} v_i E_{ii} X_{disp} \cdot Q_i N_i D_{i0}^{2\zeta} \overline{D}_i^{2g_\beta} \quad (2.42b)$$

$$\frac{dN}{dt} = \frac{\pi}{6} v_i E_{ii} X_{disp} \cdot N_i^2 D_{i0}^{2\zeta} \overline{D}_i^{2g_\beta} \quad (2.43b)$$

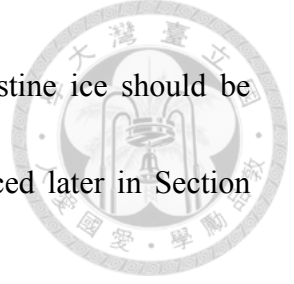


where $g_\beta = 3/(\beta+2)$ and $f_\beta = 3(\beta+1)/(\beta+2)$, v_i is ice fall speed, X_{disp} is a constant of 0.25 to account for the dispersion of size spectra, and D_{i0} is $6 \mu\text{m}$. The collection efficiency (E_{ii}) is composed of the collision efficiency E_c and aggregation efficiency E_{agg} (i.e., the probability of merging after collision) as follows:

$$E_{ii} = \max\left(1 - \frac{\overline{\rho}_i}{\rho_{i0}}, 10^{0.035T_c - 0.7}\right), \quad (2.44)$$

where ρ_{i0} is initial ice density (910 kg m^{-3}) and ρ_i is bulk apparent density. This equation is adopted from the maximum value between Chen and Lamb (1994b) (left) and Cotton et al. (1986) (right). The former is the fitting result of ice density from observation, representing mechanical locking between branched ice crystals; the latter is an empirical temperature-dependent function. Again the habit and density of the remaining pristine ice are not changed during the aggregation process. The aggregated ice crystals are converted into the “snow (aggregate)” category.

In our new parameterization, the only source of snow category is from aggregation among pristine ice. It should be noted that a threshold size ($125 \mu\text{m}$ mostly) for traditional auto-conversion process is not required in our scheme, thus the pristine ice is allowed to reach much larger sizes by diffusional growth because no arbitrary



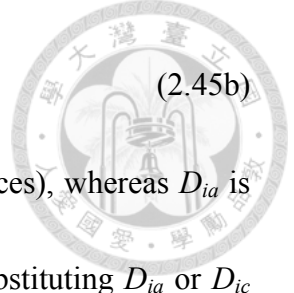
limit is imposed. As a result, bulk ventilation effect for large pristine ice should be included with consideration of crystal shape. This will be introduced later in Section 2.1.8.

2.1.6 Mass-dimension and Area-dimension relationships

The mass of ice crystal was traditionally represented by the m - D relationship of Locatelli and Hobbs (1974) as follows:

$$m_i(D_i) = a_{mi} D_i^{b_{mi}}, \quad (2.45a)$$

where D_i is the maximum dimension of the ice particles and a_{mi} and b_{mi} are constants corresponding to the specific crystal type. Prior modeling studies used to utilize a fixed m - D relationship with constant a_{mi} and b_{mi} derived from observations to represent the crystal shape. However, this relationship is crystal-type specific, but it provides no physical interpretation for the fixed relationship and its coefficients. But according to CL94, these coefficient are related to the inherent growth ratio $\Gamma(T)$ shown in (2.2). With the predictions of bulk ice shape and density developed in this study, the coefficients of a_{mi} and b_{mi} are able to vary according to the shape of ice crystals and ambient conditions. By adopting the spheroidal shape approximation, the mass of the ice crystal can be expressed as a function of crystal dimensions:



$$m_i(D_i) = \frac{\pi}{6} \rho_i D_{ia}^2 D_{ic}, \quad (2.45b)$$

where D_{ic} is the c -axis dimension (i.e. perpendicular to the basal faces), whereas D_{ia} is the a -axis dimension (i.e., perpendicular to the prism faces). By substituting D_{ia} or D_{ic} with the formulation of (2.5), (2.45b) can be written as

$$m_i(D_i) = \frac{\pi}{6} \rho_i \eta^{\beta} D_{ic}^{\beta} D_{ic}^{\frac{2}{\beta}+1}; \quad (2.46a)$$

for columnar ice ($\beta > 1$)

$$m_i(D_i) = \frac{\pi}{6} \rho_i \eta D_{ia}^{\beta+2}, \quad (2.46b)$$

for planar ice ($\beta < 1$)

By substituting η with (2.3), the values of a_{mi} and b_{mi} in terms of different ice crystal shapes were indicated, respectively,

$$a_{mi} = \frac{\pi}{6} \rho_i D_{i0}^{2-\frac{2}{\beta}}, \quad b_{mi} = \frac{2}{\beta} + 1; \quad (2.47a)$$

for columnar ice ($\phi_i > 1$)

$$a_{mi} = \frac{\pi}{6} \rho_i D_{i0}^{1-\beta}, \quad b_{mi} = \beta + 2. \quad (2.47b)$$

for planar ice ($\phi_i < 1$)

$$a_{mi} = \frac{\pi}{6} \rho_i, \quad b_{mi} = 3; \quad (2.47c)$$

for spherical ice ($\phi_i = 1$)

Now the exponent in (2.45a) has become a function of β . One can see that the value of b_{mi} keeps less than 3 for non-spherical ice crystals (plates or columns). Also, the more exaggerated is the ice crystals shape, the smaller value of β will be, until they



reach the limiting values of 1 for columns or 2 for plates. The value of b_{mi} is always greater than 2 for planar ice, but it also can be less than 2 for columnar ice. Thus b_{mi} is controlled by the adaptive growth ratio.

As to a_{mi} , it turns out to be a function of β and bulk ice density ρ_i . While the ice crystals grow more exaggerated (aspherical) in shape or have hollow or voids (smaller apparent density), the value of a_{mi} will become smaller. Now the coefficients in (2.47) are controlled by β and ρ_i , the changes in terms of ice shape and density have been considered in the m - D relationship.

For A - D relationship, it is usually represented as a typical form as follows:

$$A_i(D_i) = a_{Ai} D^{b_{Ai}}, \quad (2.48)$$

The constants of a_{Ai} and b_{Ai} also can be converted into the function of β (ζ is also the function of β) like below

$$a_{Ai} = \frac{\pi}{4} D_{i0}^{-\zeta}, \quad b_{Ai} = \frac{3(\beta+1)}{\beta+2}; \quad (2.49a)$$

for columnar ice ($\phi_i > 1$)

$$a_{Ai} = \frac{\pi}{4} D_{i0}^{2\zeta}, \quad b_{Ai} = \frac{6}{\beta+2}. \quad (2.49b)$$

for planar ice ($\phi_i < 1$)

$$a_{Ai} = \frac{\pi}{4}, \quad b_{Ai} = 2; \quad (2.49c)$$

for spherical ice ($\phi_i = 1$)

In the new parameterization, the parameters used in the m - D and A - D relationships



are not constants as assumed in earlier studies. They are able to vary with the habit change of ice crystal, which makes this a more realistic approach to represent the ice crystal shape in cloud models.

2.1.7 Terminal velocity-dimension relationships

The terminal velocity v for an ice particle in diameter D is represented by a power-law velocity-dimensional relation as shown below

$$v_i(D_i) = a_{vi} D_i^{b_{vi}} \left(\frac{\rho_0}{\rho_a} \right)^{0.5} \quad (2.50a)$$

where ρ_0 is the reference air density at mean sea level for a standard atmosphere and ρ_a is air density. The fall speed parameters a_{vi} and b_{vi} are constants in most traditional microphysics scheme, thus, the fall speed of ice does not explicitly dependent on the crystal shape. This study refers to a parameterization approach proposed by Mitchell (1996), refined by Khvorostyanov and Curry (2002), and later Mitchell and Heymsfield (2005), which produced a relationship between the Reynolds number (Re) and the Best number (X) to describe ice crystal fall speed with theoretical considerations. This approach also has been applied in the new scheme of Milbrandt and Morrison (2013) for the prediction of graupel density. In Mitchell's approach, Best number (X) is related to ice mixing ratio (Q), cross-section (A), and maximum dimension (D_{max}), given by



$$X = \frac{2Q_i g \rho_a D_{\max}^2}{A_i \mu_a^2} \quad (2.50b)$$

where g is the gravity acceleration and μ_a is the dynamic viscosity of air. With the relations of m - D and A - D introduced in last section, the Best number is integrated by size spectra and indicated as an modal value of M_X ,

$$M_X = \int \frac{2a_{mi} D_i^{b_{mi}} g \rho_a D_{i0}^{-4\zeta} D_i^{2h_\beta}}{a_{Ai} D_i^{b_{Ai}} \eta^2} N_i(D_i) dD_i = \frac{2a_{mi} g}{a_{Ai} v^2 \rho_a D_{i0}^{4\zeta}} M_{b_{mi}+2h_\beta-b_{Ai}} \quad (2.51a)$$

for columnar ice

$$M_X = \int \frac{2a_{mi} D_i^{b_{mi}} g \rho_a D_{i0}^{2\zeta} D_i^{2g_\beta}}{a_{Ai} D_i^{b_{Ai}} \eta^2} N_i(D_i) dD_i = \frac{2a_{mi} g D_{i0}^{2\zeta}}{a_{Ai} v^2 \rho_a} M_{b_{mi}+2g_\beta-b_{Ai}} \quad (2.51b)$$

for planar ice

where v is kinetic viscosity. In addition, the power-law v - D relation is revised as

$$v_i(D_i) = \frac{a_1 v}{D_i} \left(\frac{2a_{mi} D_i^{b_{mi}} g D_{\max}^2}{\rho_a v^2 a_{Ai} D_i^{b_{Ai}}} \right)^{b_1} \quad (2.52)$$

By relating (2.52) to (2.50), a_{vi} and b_{vi} are separately expressed as follows:

$$a_{vi} = a_1 v^{1-2b_1} \left(\frac{2a_{mi} g}{D_{i0}^{4\zeta} a_{Ai} \rho_a} \right)^{b_1}; \quad b_{vi} = b_1(b_{mi} + 2h_\beta - b_{Ai}) - 1 \quad (2.53a)$$

for columnar ice

$$a_{vi} = a_1 v^{1-2b_1} \left(\frac{2a_{mi} g D_{i0}^{2\zeta}}{a_{Ai} \rho_a} \right)^{b_1}; \quad b_{vi} = b_1(b_m + 2g_\beta - b_{Ai}) - 1 \quad (2.53b)$$

for planar ice

The equations of a_l and b_l below are adopted from Mitchell and Heymsfield (2005)'s

Eq. 6 and Eq. 7

$$a_1 = \frac{C_2[(1 + C_1 M_x^{0.5})^{0.5} - 1]^2 - a_0 M_x^{b_0}}{M_x^{b_1}} \quad (2.54)$$

$$b_1 = \frac{C_1 M_x^{0.5}}{2[(1 + C_1 M_x^{0.5})^{0.5} - 1](1 + C_1 M_x^{0.5})^{0.5}} - \frac{a_0 b_0 M_x^{b_0}}{C_2[(1 + C_1 M_x^{0.5})^{0.5} - 1]^2} \quad (2.55)$$

where $C_1 = 4/(\delta_0^2 C_0^{0.5})$ and $C_2 = \delta_0^2 / 4$; δ_0 and C_0 are non-dimensional surface roughness parameters and are set as $\delta_0 = 5.83$ and $C_0 = 0.6$ which are appropriate for ice particles (Mitchell, personal communication). Both a_0 and b_0 are set to zero because appropriate values are uncertain for ice particles (Mitchell and Heymsfield, 2005).

Figure 2.3 is the variation of ice fall speed with its size and habit (or shape) at a fixed ice density of 500 kg m^{-3} . It indicated that the fall speed of pristine ice increases with the equivalent diameter. Also, with equal mass, ice crystal fall speed tended to be small as it gets more aspherical because of its larger geometric cross-section and thus higher resistance from the air.

Finally, in a bulk method, the bulk fall speed (for the whole spectrum) can be derived by integrating over the whole size spectra. Thus, the mass-weighted mean fall speeds is given by,

$$v_{Qx} = \frac{\int v_x(D_x) \cdot m_x(D_x) \cdot N_x(D_x) dD_x}{\int m_x(D_x) \cdot N_x(D_x) dD_x} = a_{vx} \left(\frac{\rho_0}{\rho_a} \right)^{\frac{1}{2}} \frac{M_{x,b_{vx}+b_{mx}}}{M_{x,b_{mx}}}, \quad (2.56)$$

whereas the number-weighted mean fall speed is



$$v_{Mx} = \frac{\int v_x(D_x) \cdot N_x(D_x) dD_x}{\int N_x(D_x) dD_x} = a_{vx} \left(\frac{\rho_0}{\rho_a} \right)^{\frac{1}{2}} \frac{M_{x,b_{vx}}}{M_{x,0}} \quad (2.57)$$



Also, the volume-weighted and shape-weighted mean fall speeds of pristine ice category are derived as follows:

$$v_{V_i} = \frac{\int v_i(D_i) \cdot m_i(D_i) \cdot N_i(D_i) dD_i}{\int m_i(D_i) \cdot N_i(D_i) dD_i} = a_{vi} \left(\frac{\rho_0}{\rho_a} \right)^{\frac{1}{2}} \frac{M_{i,b_{vx}+3}}{M_{i,3}}, \quad (2.58)$$

$$v_{\phi_i} = \frac{\int v_i(D_i) \cdot m_i(D_i) \cdot N_i(D_i) dD_i}{\int m_i(D_i) \cdot N_i(D_i) dD_i} = a_{vi} \left(\frac{\rho_0}{\rho_a} \right)^{\frac{1}{2}} \frac{M_{i,b_{vx}+3\zeta+3}}{M_{i,3\zeta+3}}. \quad (2.59)$$

2.1.8 Ventilation effect

As the diameter of ice crystal reaches hundreds of micrometers, the effect of ventilation becomes more significant. Beard and Pruppacher (1971) expressed the overall ventilation effect for the whole particle in the form of

$$\bar{f} = f_{b1} + f_{b2} X^{f_{b3}}, \quad (2.60)$$

where f_{b1} , f_{b2} , and f_{b3} are constants. $X = S_C^{1/3} N_{Re}^{1/2}$ is a function of the Schmidt number S_C and the Reynolds number N_{Re} of the particle. Hall and Pruppacher (1976) reported that $f_{b1} = 1.0$, $f_{b2} = 0.14$, $f_{b3} = 2$ for $X \leq 1$ and $f_{b1} = 0.86$, $f_{b2} = 0.28$, $f_{b3} = 1$ for $X > 1$. By applying v in (2.50a) into the definition of N_{Re} as follows:

$$N_{Re} = \frac{v_i D_i}{\nu} = \frac{a_{vi} D_i^{b_{vi}} D_{max}}{\nu} \left(\frac{\rho_0}{\rho_a} \right)^{0.5} \quad (2.61)$$

and the bulk ventilation effect is expressed as

$$f_{vi} = \int \left[f_{b1} + f_{b2} S_C^{f_{b3}/3} \left(\frac{a_{vi} D_i^{b_{vi}} w D_{\max}}{v} \right)^{0.5 f_{b3}} \right] N_i(D_i) dD_i \quad (2.62)$$

where $w = (\rho_0/\rho_a)^{0.5}$. By incorporating (2.62) into the ice deposition growth equations of mass (2.9) and shape moment (2.20), the two equations are revised as

$$\frac{dm}{dt} = \frac{2\pi D_v \Delta \rho_v}{D_{i0}^{3f(\beta)}} \left[\begin{array}{l} f_{b1} M_{i,3f(\beta)+1} + \\ f_{b2} S_C^{f_{b3}/3} \left(\frac{\omega a_{vi}}{v} \right)^{0.5 f_{b3}} D_{i0}^{-\zeta \gamma} M_{i,3f(\beta)+0.5b_{vi}f_{b3}+0.5h_{\beta}f_{b3}+1} \end{array} \right] \quad (2.63a)$$

$$\frac{dM_{\phi}}{dt} = \frac{12D_v \Delta \rho_v (\gamma+1)}{\rho_{i,dep} D_{i0}^{3f(\beta)+3\zeta}} \left[\begin{array}{l} f_{b1} M_{i,3f(\beta)+3\zeta+1} + \\ f_{b2} S_C^{f_{b3}/3} \left(\frac{\omega a_{vi}}{v} \right)^{0.5 f_{b3}} D_{i0}^{-\zeta f_{b3}} M_{i,3f(\beta)+3\zeta+0.5b_{vi}f_{b3}+0.5h_{\beta}f_{b3}+1} \end{array} \right] \quad (2.64a)$$

are for columnar ice;

$$\frac{dm}{dt} = \frac{2\pi D_v \Delta \rho_v}{D_{i0}^{3f(\beta)}} \left[\begin{array}{l} f_{b1} M_{i,3f(\beta)+1} + \\ f_{b2} S_C^{f_{b3}/3} \left(\frac{\omega a_{vi}}{v} \right)^{0.5 f_{b3}} D_{i0}^{0.5 \zeta f_{b3}} M_{i,3f(\beta)+0.5b_{vi}f_{b3}+0.5g_{\beta}f_{b3}+1} \end{array} \right] \quad (2.63b)$$

$$\frac{dM_{\phi}}{dt} = \frac{12D_v \Delta \rho_v (\gamma+1)}{\rho_{i,dep} D_{i0}^{3f(\beta)+3\zeta}} \left[\begin{array}{l} f_{b1} M_{i,3f(\beta)+3\zeta+1} + \\ f_{b2} S_C^{f_{b3}/3} \left(\frac{\omega a_{vi}}{v} \right)^{0.5 f_{b3}} D_{i0}^{0.5 \zeta f_{b3}} M_{i,3f(\beta)+3\zeta+0.5b_{vi}f_{b3}+0.5g_{\beta}f_{b3}+1} \end{array} \right] \quad (2.64b)$$

are for planar ice.

Figure 2.4 is the variation of ice ventilation effect with its size and habit (or shape) at a fixed ice bulk density of 900 kg m^{-3} . It showed that the ventilation effect for a population of ice crystals became increasingly obvious (more than 3 times) either for the prolate or oblate crystal while their mean equivalent diameter exceeded about 1 mm.



2.1.9 3-moment closure technique

As introduced above, the size spectrum of the hydrometeor is described by an analytic gamma distribution function in (1.1) for the bulk scheme. Hence the k th moment of the distribution is given by

$$M_k \equiv \int D^k N(D) dD = N_0 \frac{\Gamma(1 + \alpha + k)}{\lambda^{1+\alpha+k}} = \frac{N\Gamma(1 + \alpha + k)}{\Gamma(1 + \alpha)\lambda^k}, \quad (2.65)$$

where N_0 is the intercept parameter and is expressed as

$$N_0 = N \frac{1}{\Gamma(1 + \alpha)} \lambda^{1+\alpha}, \quad (2.66)$$

λ is the slope parameter and can be derived as

$$\lambda = \left[\frac{\Gamma(1 + b_m + \alpha)}{\Gamma(1 + \alpha)} \frac{a_m N}{\rho_a Q} \right]^{1/b_m}. \quad (2.67)$$

where Γ the complete gamma function, ρ_a air density, a_m and b_m are the coefficients of m - D relationship addressed in Section 2.1.6. So the modal values in terms of the zero-moment and the 3rd-moment are separately represented as

$$M_0 = \int D^0 n(D) dD = N; \quad (2.68)$$

$$M_3 = \int D^3 n(D) dD = \frac{N\Gamma(\alpha + 4)}{\Gamma(\alpha + 1)\lambda^3}. \quad (2.69)$$

These two moments are usually utilized as the prognostic variables corresponding to the quantities of number and mass (when the density is specified) for the hydrometeor which is so-called the two-moment bulk approach. In such an approach, the parameters of N_0 and λ both are prognostic while the parameter of α is held constant. The size



spectrum is able to evolve against different slope and intercept but with fixed spectral index. In this study, three parameters are used to represent the size spectrum, and this permit the size spectrum to evolve more flexibly. Therefore, in addition to the moments of mass (or volume) and number, one new moment of cross-section proportional to the 2nd-moment has been included.

One advantage of including the shape factor for cloud ice crystals in this study is that it allows a derivation of the cross-section (or the 2nd-moment) from crystal shape moments. Ice crystals typically fall with their major dimension in the horizontal plane. Thus, the geometric cross-section for columnar ice can be approximated as πac and its 2nd moment is given by

$$M_{2c} = \int D_{ia} D_{ic} N_i(D_i) dD_i = D_{i0}^{-\zeta} \int D_i^{g_\beta} N_i(D_i) dD_i = D_{i0}^{-\zeta} M_{g_\beta}, \quad (2.70a)$$

where $g_\beta = 3(\beta+1)/(\beta+2)$. Similarly, the geometric cross-section for planar ice is πa^2 , so its 2nd moment is derived as

$$M_{2p} = \int D_{ia}^2 N_i(D_i) dD_i = D_{i0}^{2\zeta} \int D_i^{h_\beta} N_i(D_i) dD_i = D_{i0}^{2\zeta} M_{h_\beta}, \quad (2.70b)$$

where $h_\beta = 6/(\beta+2)$. For spherical ice, the cross-section is πr^2 so the 2nd moment is:

$$M_2 = \int D_i^2 N_i(D_i) dD_i = \frac{N_i \Gamma(\alpha_i + 3)}{\Gamma(1 + \alpha_i) \lambda_i^2}. \quad (2.70c)$$

With the derivation of the three spectral moments, a closure can be obtained for the spectral parameters. From (2.68c), an equation for λ was obtained as



$$\lambda_i = \left[\frac{M_0(\alpha_i + 2)(\alpha_i + 1)}{M_2} \right]^{1/2}. \quad (2.71a)$$

By dividing (2.69) by (2.70c), another equation for λ_i was derived as

$$\lambda_i = (\alpha_i + 3) \frac{M_2}{M_3}, \quad (2.71b)$$

Given (2.71a) equal to (2.71b), a quadratic equation of α_i was obtained below

$$\frac{\alpha_i^2 + 3\alpha_i + 2}{\alpha_i^2 + 6\alpha_i + 9} = K, \quad \text{with } K = \frac{M_2^3}{M_3^2 M_0}. \quad (2.72)$$

Then the derivation of new α_i at each time step is accomplished by using the quadratic formula as shown below,

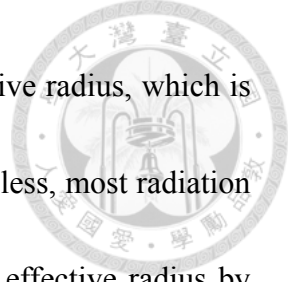
$$\alpha_{new} = \frac{6K - 3 \pm \sqrt{8K + 1}}{2 - 2K}. \quad (2.73)$$

Note that α cannot be negative, hence we take only the plus sign before the square root in (2.73).

Since α is updated by the ratio of three modal values, the parameters of λ_i and N_{0i} are also predicted at each time step. Therefore, with the three prognostic variables with respect to the category of pristine ice, the ice-three-moment parameterization has been developed. Some further comparisons and validations to the approach will be presented in Chapter 3.

2.1.10 Orientation of crystal shape

As mentioned, the crystal shape is an important factor to account for the radiation



budget. In cloud radiative calculations, a key parameter is the effective radius, which is the quantity of the 3rd-moment divided by the 2nd-moment. Nevertheless, most radiation transfer models and satellite retrieve algorithms oversimplified the effective radius by an assumption of spherical ice, given a specific crystal type, or using a temperature-dependent function to account for shape. Now our parameterization allows the effective radius to vary with the crystal shape in a realistic way. Also, since ice crystals falls with specific orientation in the atmosphere, the influence of the solar zenith angle should be considered as well.

By using (2.22) for ϕ_i and (2.70) for the 2nd-moment, the cross-section in the polar coordinate is derived as

$$A_i(D_i) = \frac{1}{1 - \cos^2 \theta_s + \overline{\phi_i^{(-2)}} \cos^2 \theta_s} \frac{\pi}{4} M_{i,2c}, \quad (2.74a)$$

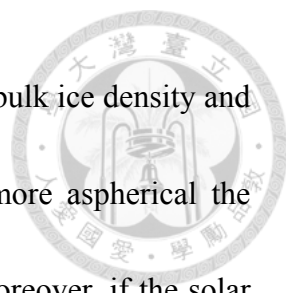
for columnar ice

$$A_i(D_i) = \frac{1}{1 - \cos^2 \theta_s + \overline{\phi_i^{-2}} \cos^2 \theta_s} \frac{\pi}{4} M_{i,2p}. \quad (2.74b)$$

for planar ice

where θ_s is the solar zenith angle. With the quantities above, the derivation of the effective radius was completed through the following equation:

$$r_e \equiv \frac{\int D^3 N(D) dD}{\int D^2 N(D) dD} = \frac{3\overline{Q}_i}{4\overline{\rho}_i A_i}. \quad (2.75)$$




Here the effective radius has been converted into a function of bulk ice density and the cross-section area. One can see from this equation that the more aspherical the crystal evolves in shape, the smaller the effective radius will be. Moreover, if the solar zenith angle deviated from 0 degree, the effective radius will become larger. Accordingly, the influences of the crystal shape, density, and orientation are included on the effective radius in our parameterization.

2.1.11 Remarks

In the ice adaptive habit parameterization, two new ice moments of shape and volume have been proposed and extended to all cloud ice crystal-related microphysical processes. The initiations of ice crystals, including primary and secondary productions, are assumed to be isometric with an initial density of 910 kg m^{-3} and an initial diameter of $6 \text{ }\mu\text{m}$. The moments of shape and volume disappear immediately during their conversion to other hydrometeors (with volume replaced by mass). These arrangements are listed in **Table 2**.

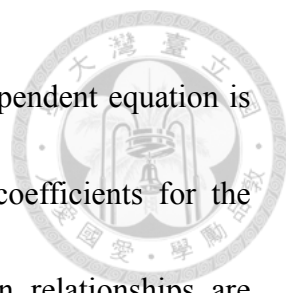
2.2 A new multi-moment microphysics scheme

The new multi-moment microphysics scheme predicts the mixing ratios, number concentrations, habit, and density (the last two variables are predicted for cloud ice



hydrometeor alone) with respect to six hydrometeor categories of cloud, rain, ice, snow, graupel, and hail, together with tracking three condensation nuclei (CN) groups (dry or interstitial CN, rain CN, and cloud CN) and a specified number of ice nuclei (IN) species. **Figure 2.5** is a schematic plot to describe the conversions of hydrometeor categories in the new microphysics scheme.

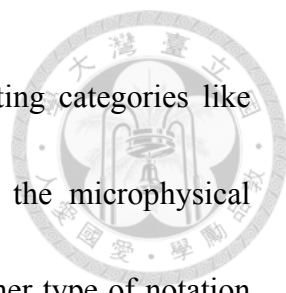
The aqueous hydrometeor categories consist of cloud droplets and raindrops with an “implied” threshold diameter of 100 μm (note: rain embryos a bit smaller than 100 μm is allowed). The ice-phase particles include pristine ice crystals, snow-aggregates, graupel and hail. The pristine ice crystals have no upper size limit as done in earlier studies, whereas the snow particles are produced solely from the aggregation among pristine ice. The graupel particle initiates from riming of ice crystals and snow-aggregates, while the hail is formed by the freezing of super-cooled raindrops with high-density and graupel growth during heavy riming. In traditional bulkwater schemes the definitions of cloud ice, snow and even graupel are somewhat ambiguous. In our new definition, the snow category is limited to aggregates while rimmed ice crystals and rimmed snow are immediately converted to the graupel category. The size spectrums of all hydrometeors are represented in the three-parameter gamma distribution functions described in (1.1). The scheme can also be reduced to a 2-moment option by using fixed α_i . Also, except for pristine ice, the other particles are assumed to



be spherical with individual fixed bulk densities, whereas a size-dependent equation is used to diagnose the bulk density of the snow-aggregates. The coefficients for the spectral index, the mass-dimension, and the fall speed-dimension relationships are summarized in **Table 3**.

For microphysical processes, the aerosol activation and time-splitting technique is inherent from Cheng et al. (2007; 2010). For ice deposition-nucleation mechanism, options of schemes from Chen et al. (2008), Hoose et al. (2010), and DeMott et al. (2010) are available. The liquid-phase statistical parameterization are adopted from Chen and Liu (2004) whereas most of the equations in mixed- and solid- phases are modified from various existing scheme such as Milbrandt and Yau (2005b), Morrison et al. (2009), and so on. The dry and wet growth modes for the hailstone are also included based on the approach of Chen and Lamb (1994b). The detail modifications and simplifications made for these parameterizations will be illustrated in the following sub-sections. The overall source/sink terms in the continuity equations are listed in **Appendix A** and the collection efficiencies among interacting hydrometeors are arranged in **Table 4**.

The notation for the terms involving two interacting categories are denoted by BMP_{xy} , where B is the prognostic variable, MP represents the microphysical processes, and the subscripts x and y indicated that quantity of B is being transferred from

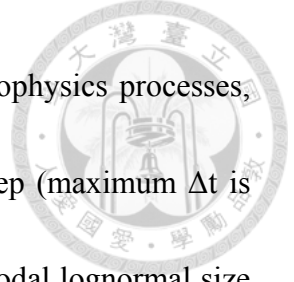


hydrometeor category x to y . If the terms involving three interacting categories like three-component freezing, a three-letter subscript of xyz follows the microphysical process extra with the destination hydrometeor category of z . Another type of notation denoted by QH_{omp} is only used for the change rate of hailstone mixing ratio, and o indicates whether the dry- (denote d) or wet- (denote w) growth mode is occurred. All notations utilized in the new microphysics scheme are listed in **Table 5** with brief definitions, and coefficients of the formulas adopted from Chen and Liu (2004) are arranged in **Table 6**.

2.2.1 Activation/deactivation

$(QAC_{ac}, QAC_{ar}, QAC_{cv}, QAC_{rc}, NAC_{ac}, NAC_{ar}, NAC_{cv}, NAC_{rc})$

In the new scheme, a technique of time splitting integration in a Lagrangian framework is adopted from Cheng et al. (2007, 2010). This approach treats each grid box as an ascending/descending air parcel and resolves the changes in CN and thermodynamics fields caused by activation and diffusional growth in a smaller time step (minimum Δt is 0.01 s, which may be relaxed as the time variation becomes slower) thereby with a finer spatial resolution. Thus the maximum supersaturation can be explicitly resolved and the number of activated cloud droplets or raindrops can be more accurately simulated. The grown particles will be placed to an appropriate vertical



location during the advection procedure. As to the remaining microphysics processes, they are calculated in an Eulerian framework with a larger time step (maximum Δt is 20s). Also, aerosol is assumed to be ammonium sulfate with a tri-modal lognormal size distribution. There are several CN types for selection, including marine, clean, average, and urban from Whitby (1978) (see **Figure 2.6**). CN related parameters are listed in **Table7**. The cutoff size of CN to be activated into cloud drops depending on supersaturation according to Köhler equation, and prognostic dry or interstitial CN, rain CN, and cloud CN mass are tracked.

Deactivation of cloud drops back into CN is treated according to Chen and Liu (2004, hereafter CL04) (see their Table 1) which are the fitting results from different sceneries of bin mode simulations. The number and mass conversion rates for cloud drop deactivation are

$$NAC_{cv} = -\exp[a_{N1} + b_{N1} \ln N_c + c_{N1} \ln R_c + d_{N1} \cdot \ln(-\Delta S_w)] \quad (2.76a)$$

$$QAC_{cv} = NAC_{cv} \cdot 4.1888 \times 10^{-15} \quad (2.76b)$$

where R_c is cloud droplet mean volume radius and ΔS_w is supersaturation ratio with respect to water. The value of 4.1888×10^{-15} is represented the minimum size $2 \mu\text{m}$ of cloud droplet. Also, the number and mass conversion rates for cloud drop formation from raindrop evaporation are

$$NAC_{rc} = \Delta S_w \cdot A_{DK} \cdot \exp(a_{N2} + b_{N2} \ln N_r + c_{N2} \ln R_r) \quad (2.77a)$$



$$QAC_{rc} = NAC_{rc} \cdot 5.236 \times 10^{-10} \quad (2.77b)$$

where R_r is raindrop mean volume radius, the value of 5.236×10^{-10} is corresponding to the minimum size $100 \mu\text{m}$ of rain drop, and A_{DK} is a function of air temperature and pressure:

$$A_{DK} \equiv \frac{TR_v}{D_v e_{sw}} + \frac{L_v}{Tk_a} \left(\frac{L_v}{TR_v} - 1 \right) \quad (2.77c)$$

where e_{sw} is saturation vapor pressure, R_v is gas constant of water vapor, k_a is thermal conductivity of air, and L_v is latent heat of vaporization.

2.2.2 Nucleation/multiplication

$$\left(\begin{array}{l} QND_{vi}, QNM_{ci}, QNM_{rh}, QNC_{ci}, QHO_{ci}, QHO_{rh}, QFZ_{ci}, QFZ_{rh}, QIM_{ii}, NND_{vi}, \\ NNM_{ci}, NNM_{rh}, NNC_{ci}, NHO_{ci}, NHO_{rh}, NFZ_{ci}, NFZ_{rh}, NIM_{ii}, FND_{vi}, FNM_{ci}, \\ FNC_{ci}, FHO_{ci}, FFZ_{ci}, FIM_{ii}, VND_{vi}, VNM_{ci}, VNC_{ci}, VHO_{ci}, VFZ_{ci}, VIM_{ii} \end{array} \right)$$

The formation of ice particles includes homogeneous freezing, heterogeneous nucleation, and ice multiplication (so-called ice secondary production). In this study, homogeneous freezing of cloud droplets is adopted from DeMott et al. (1994). They give the number of droplets that freeze in time Δt at a given temperature as

$$NHO_{ci} = \int [1 - \exp(-J_{hof} V_c \Delta t)] N_c(D_c) dD_c \quad (2.78a)$$

where $J_{hof} = 10^{-606.3952 - 52.6611 \times T_c - 1.7439 \times T_c^2 - 0.0265 \times T_c^3 - 1.536e-4 \times T_c^4}$ and V_c is the mean droplet volume.

Also, the homogeneous mass, shape, and volume production rates are given by

$$QHO_{ci} = \int [1 - \exp(-J_{hof} V_c \Delta t)] Q_c N_c(D_c) dD_c \quad (2.78b)$$

$$FHO_{ci} = QHO_{ci} / a_{mi0} \quad (2.78c)$$

$$VHO_{ci} = QHO_{ci} / \rho_{i0}. \quad (2.78d)$$

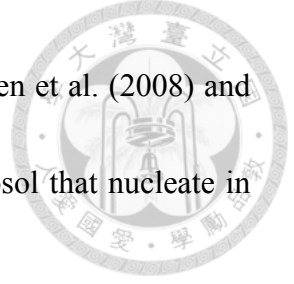


Where $a_{mi0} = \pi\rho_{i0}/6$. In addition, the homogeneous freezing of raindrop mass and number will be converted to hail immediately upon the temperature below -40°C .

The ice heterogeneous nucleation mechanisms include deposition, condensation, contact-freezing, and immersion-freezing. In the new scheme, there are eight options available for deposition/condensation nucleation from traditional empirical parameterization of Fletcher (1962), Cooper (1986), Huffman (1973), Meyers et al. (1992), Yankofsky (1981), Field (2006) to a relatively sophisticated parameterization of Chen et al. (2008) which is based on a classical nucleation theory (CNT). In CNT, the rate of heterogeneous nucleation per aerosol particle and time is given by

$$J_{dep} = A_{NU} r_N^2 \sqrt{f_g} \exp\left(\frac{-\Delta g^{\#} - f_g \Delta g_{g,dep}}{kT}\right) \quad (2.79a)$$

where A_{NU} is one ambient term, r_N is the aerosol particle (nucleus) radius, f_g is a geometric term containing information about the aerosol's ice nucleation ability, $\Delta g^{\#}$ is the aerosol-dependent activation energy, $\Delta g_{g,dep}$ is the homogeneous energy of germ formation derived from labs-measurement, k is the Boltzmann constant, and T is the air temperature in K . The parameters of contact angle, activation energy, and aerosol radius



in terms of soot, Saharan dust, and Asian dust are adopted from Chen et al. (2008) and Hoose et al. (2010) listed in the **Table 8**. Thus, the number of aerosol that nucleate in time Δt is given by

$$NND_{vi} = N_{in} [1 - \exp(-J_{dep} \Delta t)] \quad (2.79b)$$

Moreover, another implicit parameterization of ice primary production recently proposed by DeMott et al. (2010) has been implemented into the new microphysics scheme for optional use. They aggregated the multi-study dataset into 3°C temperature interval for fitting the relation between N_{in} and N_{aer} . A power law coefficients were then used to determine the overall size and temperature dependencies of ice nuclei active under mixed-phase cloud conditions, represented as follows:

$$NND_{vi} = a(T_0 - T)^b (N_{aer,0.5})^{c(T_0 - T) + d} \quad (2.79c)$$

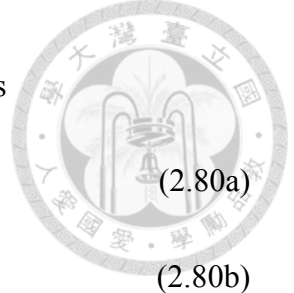
where $a = 0.0000594$, $b = 3.33$, $c = 0.0264$, $d = 0.0033$, $N_{aer,0.5}$ is the number concentration of aerosol particles with diameters larger than 0.5 μm , and N_{in} is ice nuclei number concentration at T . Also, the mass, shape, and volume nucleation rates are listed below

$$QND_{vi} = NND_{vi} \cdot m_{i0} \quad (2.79d)$$

$$FND_{vi} = QND_{vi} / a_{mi0} \quad (2.79e)$$

$$VND_{vi} = QND_{vi} / \rho_{i0} \quad (2.79f)$$

where $m_{i0} = a_{mi0} D_{i0}^3$ is the initial ice crystal mass. Both the immersion freezing of cloud



droplets and raindrops are adopted from Bigg (1953) and indicated as

$$NNM_{xy} = \frac{\pi}{6} B' \exp[A'(T_0 - T) - 1] M_{x,3} \quad (2.80a)$$

$$QNM_{xy} = \frac{\pi a_{mw}}{6} B' \exp[A'(T_0 - T) - 1] M_{x,6} \quad (2.80b)$$

where $x = c$, $y = i$ for the cloud droplets freezing to pristine ice, $x = r$, $y = h$ for the raindrops freezing to hail particles, $A' = 0.66$, and $B' = 100$. Also, the shape and volume freezing rates of cloud droplets are the same to (2.79e) and (2.79f). The contact freezing of cloud droplets follows Young (1974) and Cotton et al. (1986) including the collision mechanisms of Brownian movements, thermophoresis, and diffusiophoresis.

Ice multiplication, initiated from the splintering of graupel and snow-aggregates during riming at temperatures between -3°C and -8°C , is based on Hallet and Mossop (1974). They reported that approximately 350 ice splinters are produced for every 10^{-3} grams of rimed crystals around -5°C and proposed a parameterization as follows:

$$NIM_{ii} = 3.5 \times 10^8 f(T_c) (QRM_{cs} + QRM_{cg} + QRM_{rs} + QRM_{rg}) \quad (2.81)$$

where $f(T_c)$ is 0 for $T < 265$ K and $T > 270$ K, 1.0 for $T = 268$ K, and decreases linearly from 268 K separately to two temperature limits above. The riming terms of QRM will be described in Section 2.2.4. The splintering ice crystal is assumed to be isometric with an initial mass of m_{i0} , and the shape and volume production rates are the same to (2.79e) and (2.79f).



2.2.3 Vapor diffusion/evaporation

$$\left(QVD_{vc}, QVD_{vr}, QVD_{vi}, QVD_{vs}, QVD_{vg}, QVD_{vh}, QSB_{iv}, QSB_{sv}, QSB_{gv}, QSB_{hv}, QEV_{cv}, \right. \\ \left. QEV_{rv}, QEV_{sv}, QEV_{gv}, QEV_{hv}, NSB_{iv}, NSB_{sv}, NSB_{gv}, NSB_{hv}, FVD_{vi}, FSB_{iv}, VVD_{vi}, VSB_{iv} \right)$$

All hydrometeor categories undergo vapor diffusional growth in an environment supersaturated. For aqueous particles, the diffusional growth rates are referred to CL04 and indicated below

$$QVD_{vc} = \frac{\Delta S_w}{A_{DK}} \exp(a_{Q1} + b_{Q1} \ln N_c + c_{Q1} \ln R_c) \quad (2.82a)$$

$$QVD_{vr} = \frac{\Delta S_w}{A_{DK}} N_r \exp[a_{Q2} + b_{Q2} (\ln R_r)^2 + c_{Q2} (\ln R_r)^3] \quad (2.82b)$$

For frozen particles, a formulation was adopted from Morrison scheme (Morrison et al. 2005) based on the work of Khvorostyanov (1995) and Khvorostyanov et al. (2001). The diffusional growth rates for pristine ice with shape effect have been introduced in (2.63), and for the other solid hydrometeors they are in the form of

$$QVD_{vx} = 2\pi N_{0x} f_{vx} \frac{D_v \rho_a (Q_v - Q_{vsi})}{AB_i} \quad (2.82c)$$

where $x \in \{i, s, g, h\}$. $AB_i = 1 + dQ_{vsi}/dT^*(L_s/c_{pm})$ is a latent heating correction function; $dQ_{vsi}/dT = L_s Q_{vsi}/R_v T^2$; c_{pm} is the specific heat of moist air; Q_{vsi} is the water vapor mixing ratio at ice saturation; $Q_v - Q_{vsi}$ is supersaturation with respect to ice, and f_{vx} is the mass-weighted ventilation factor.

In the condition of sub-saturation with respect to ice, the value of QVD_{vx} will become negative because of sublimation loss. The loss rate of frozen particle number is



derived by a mean-size assumption as follows:

$$NSB_{xv} = QSB_{xv} \cdot N_x / Q_x \quad (2.82d)$$

where $x \in \{i, s, g, h\}$. For particles undergoing a sub-saturated environment with respect to water, the hydrometeors are inclined to evaporate. The mass loss rates are

$$QEV_{xv} = 2\pi N_{0x} f_{vx} \frac{D_v \rho_a (Q_v - Q_{vsw})}{AB_w} \quad (2.82e)$$

where $x \in \{c, r, s, g, h\}$. $AB_w = 1 + dQ_{vsw}/dT * (L_v/c_{pm})$ is a latent heating correction function;

$dQ_{vsw}/dT = L_v Q_{vsw} / R_v T^2$; Q_{vsw} is the water vapor mixing ratio at water saturation; $Q_v - Q_{vsw}$ is supersaturation with respect to water.

2.2.4 Accretion/aggregation

$$\left(\begin{array}{l} QCL_{cr}, QCL_{ir}, QCL_{ii}, QCL_{is}, QCL_{ig}, QCL_{ih}, QCL_{sr}, QCL_{sh}, QCL_{gr}, QCL_{irg}, QCL_{irh}, \\ QCL_{srs}, QCL_{srg}, QCL_{srh}, QCL_{grg}, QCL_{grh}, QRM_{ci}, QRM_{cs}, QRM_{cg}, QRM_{ch}, QRM_{ri}, \\ QRM_{rs}, QRM_{rg}, QRM_{rh}, NCL_{cc}, NCL_{cr}, NCL_{rr}, NCL_{ir}, NCL_{ii}, NCL_{is}, NCL_{ig}, NCL_{ih}, \\ NCL_{sr}, NCL_{ss}, NCL_{sh}, NCL_{gr}, NCL_{irg}, NCL_{irh}, NCL_{srs}, NCL_{srg}, NCL_{srh}, NCL_{grg}, \\ NCL_{grh}, NRM_{ci}, NRM_{cs}, NRM_{cg}, NRM_{ch}, NRM_{ri}, NRM_{rs}, NRM_{rg}, NRM_{rh}, FCL_{ir}, \\ FCL_{is}, FCL_{ig}, FCL_{ih}, FRM_{ci}, VCL_{ir}, VCL_{is}, VCL_{ig}, VCL_{ih}, VRM_{ci} \end{array} \right)$$

In the new scheme, the warm-rain collection processes came from CL04 which are the physically-based fitting bulk water equations from the simulation results with a multi-moment bin model under different environment conditions. The accretion rates of cloud droplets by raindrops are shown

$$NCL_{cr} = N_c \cdot N_r \exp(a_{N3} + b_{N3} \cdot \ln R_r + c_{N3} \cdot \ln R_c) \cdot g(R_r, \rho_a) \quad (2.83a)$$

$$QCL_{cr} = N_c \cdot N_r \exp(a_{Q3} + b_{Q3} \cdot \ln R_r + c_{Q3} \cdot \ln R_c) \cdot g(R_r, \rho_a) \quad (2.83b)$$

where $g(R_r, \rho_a)$ is auxiliary functions for terminal velocity adjustment. Also, the self-collection rates among cloud droplets and raindrops are separately given by

$$NCL_{cc} = \exp[a_{N4} + b_{N4} \cdot \ln N_c + c_{N4} \cdot (\ln R_c)^3] \cdot g(R_c, \rho_a) \quad (2.84a)$$

$$NCL_{rr} = \exp[a_{N5} + b_{N5} \cdot \ln N_r + c_{N5} R_r^{-1}] \cdot g(R_r, \rho_a) \quad (2.84b)$$

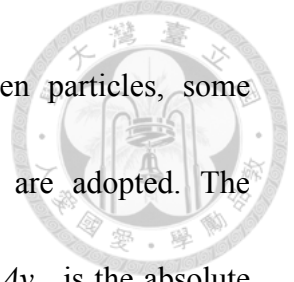
where $g(R_c, \rho_a)$ is auxiliary functions for terminal velocity adjustment as well.

The collection processes involving ice particles are classified as dry collection among frozen particles alone and wet collection among liquid and frozen particles (so-called riming). Two general equations with respect to mixing ratio and number concentration for particle category x collecting y are listed below

$$QCL_{yx} = \frac{\pi \Delta v_{yx} E_{yx} a_{my}}{4 \rho_a} \left(M_{x,2} M_{y,b_{my}} + 2 M_{x,1} M_{y,b_{my}+1} + M_{y,b_{my}+2} \right) \quad (2.85a)$$

$$NCL_{yx} = \frac{\pi \Delta v_{yx} E_{yx}}{4 \rho_a} \left(M_{x,2} + 2 M_{x,1} M_{y,1} + M_{y,2} \right) \quad (2.85b)$$

where $x \in \{s, g, h\}$, $y \in \{i, s\}$ are for dry collection (the accretion of pristine ice with shape by other frozen particles has been introduced in Section 2.1.4), and $x \in \{i, s, g, h\}$, $y \in \{c, r\}$ are for wet collection (the riming growth of pristine ice with shape has been introduced in Section 2.1.3). E_{yx} is the bulk collection efficiency between two interacting hydrometeor categories of x and y . For wet collection, some approximate empirical formulas which are the functions of mean volume diameter or Stokes number



are used from previous studies. For dry collection among frozen particles, some temperature-dependent equations following Ferrier et al. (1995) are adopted. The equations of E above and their references are listed in the **Table 4**. Δv_{yx} is the absolute difference of fall speeds in term of two interacting hydrometeor particles, and an approximation proposed by Murakami (1990) is given by

$$\Delta v_{yx} \equiv |v_x(D_x) - v_y(D_y)| \approx \sqrt{(v_{Qx} - v_{Qy})^2 + 0.04v_{Qx}v_{Qy}} \quad (2.85c)$$

where v_{Qx} is the mass-weighted fall speed for category x . For the collection number equations, v_Q shall be replaced with the number-weighted fall speed of v_N . The determinations of v_Q and v_N for frozen particles have been described in (2.58) and (2.59), whereas CL04 also provided parameterization formulas for the group fall speeds of cloud droplets and raindrops (not shown).

For self-collection processes, the aggregation among pristine ice to snow-aggregates has been introduced in Section 2.1.5. The decrease rate of aggregation among snow-aggregate particles is parameterized by Passarelli (1978) as follows:

$$NCL_{ss} = \frac{1108a_{vs}E_{ss}}{4.720\rho_a} \left(\frac{\rho_0}{\rho_a} \right)^{0.5} \pi^{\frac{1-b_{vs}}{3}} \rho_s^{\frac{-2-b_{vs}}{3}} \rho_a^{\frac{2+b_{vs}}{3}} Q_s^{\frac{2+b_{vs}}{3}} N_s^{\frac{4-b_{vs}}{3}} \quad (2.86a)$$

where a_{vs} and b_{vs} are the parameters of v - D relation for snow-aggregate particles. ρ_s is the bulk density of snow-aggregates which is given by Passarelli and Srivastava (1978):

$$\overline{\rho_s} (\text{kgm}^{-3}) = 150 \overline{D_s}^{-0.6} \quad (2.86b)$$



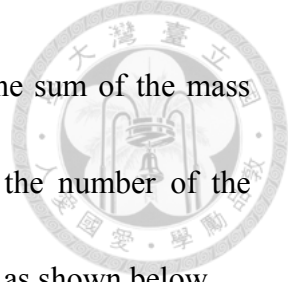
where D_s is the mean volume diameter for snow-aggregates. The aggregation efficiency (E_{ss}) among snow-aggregates is using the maximum value between Chen and Lamb (1994b) (left) and Ferrier et al. (1995) (right) as shown below

$$E_{ss} = \max\left(1 - \frac{\overline{\rho_s}}{\rho_{i0}}, 0.005e^{0.17c}\right), \quad (2.86d)$$

For collisional freezing, it means that collections of mass and number between the raindrop and a solid hydrometeor contribute to a third frozen category through freezing. A method proposed by Milbrandt and Yau (2005b) for this three-component freezing was adopted. They assumed water is distributed evenly throughout the volume of the colliding frozen particle during contact, which increases its mass and bulk density but not volume. A new frozen category z is produced with the density of ρ_z from the collision between a raindrop and a frozen particle x , which is expressed as

$$\frac{\pi}{6}(\rho_w D_r^3 + \rho_x D_x^3) = \frac{\pi}{6}(\rho_z D_z^3) \quad (2.87a)$$

where $x \in \{i, s, g\}$, the destination category $z \in \{s, g, h\}$, and $D_z = \max(D_x, D_r)$. The destination particle is then classified as belonging to the frozen category with the closest bulk density to ρ_z . It means that the new frozen particle will be classified as snow-aggregates if $\rho_z \leq 0.5(\rho_s + \rho_g)$, as graupel if $0.5(\rho_s + \rho_g) < \rho_z \leq 0.5(\rho_g + \rho_h)$, and as hail if $\rho_z > 0.5(\rho_g + \rho_h)$ with $D_r > 2.5$ mm. The sink terms for the mass and number of raindrops and hydrometeor x are derived by the collection equations described above.



The source term for the mass of the destination hydrometeor z is the sum of the mass sink terms for the two colliding categories. The source term for the number of the destination category z is calculated using the mean mass diameter D_z as shown below

$$NCL_{xrz} = \frac{(QCL_{xr} + QRM_{rx})\rho_a}{a_{mz}D_z^{b_{mz}}} \quad (2.87b)$$

where a_{mz} is the parameter of m - D relation for the category z .

2.2.5 Auto-conversion/ initiation of graupel/breakup

$$\left(\begin{array}{l} QCN_{cr}, QCN_{is}, QCN_{gh}, QIN_{ig}, QIN_{sg}, QBK_{rc}, NCN_{cr}, NCN_{is}, NCN_{is1}, NCN_{gh}, MIN_{ig}, \\ NIN_{sg}, NBK_{rc}, NBK_{rr}, FCN_{is}, FIN_{ig}, VCN_{is}, VIN_{ig} \end{array} \right)$$

The auto-conversion of mass and number from cloud droplets to raindrops is adopted from CL04 and listed below

$$NCN_{cr} = N_c^2 \exp(a_{N6} + b_{N6}R_c + c_{N6}/R_c)g(R_c, \rho_a) \quad (2.88a)$$

$$QCN_{cr} = N_c \exp(a_{Q4} + b_{Q4}Q_c/N_c) \quad (2.88b)$$

where $g(R_c, \rho_a)$ is auxiliary functions for terminal velocity adjustment. As to the auto-conversion from pristine ice with shape to snow-aggregates, i.e. through the process of cloud ice self-collection/aggregation, the equations for the conversion rates of mass and number have been illustrated in Section 2.1.5. The conversion of graupel to hail is adopted from the scheme of Milbrandt and Yau. They assumed this process to occur when the graupel particles growing by accretion reach a critical diameter of



Shumann-Ludlam limit (SLL, Young 1993). The diameter of SLL is a function of cloud, rain, and ice mass contents derived by Ziegler (1985):

$$D_{SLL} = 0.01 \left\{ \exp \left[\frac{-T_C}{1.1 \times 10^4 (Q_c + Q_r) \rho_a - 1.3 \times 10^3 Q_i \rho_a + 1} \right] - 1 \right\} \quad (2.89a)$$

and the conversion rates of mass and number from graupel to hailstone are indicated

$$NCN_{gh} = N_{0g} \lambda_g^{-1} e^{-D_{SLL} \lambda_g} / \Delta t \quad (2.89b)$$

$$QCN_{gh} = a_{mg} N_{0g} e^{-D_{SLL} \lambda_g} \left(\frac{D_{SLL}^3}{\lambda_g} + \frac{3D_{SLL}^2}{\lambda_g^2} + \frac{6D_{SLL}}{\lambda_g^3} + \frac{6}{\lambda_g^4} \right) / \Delta t \quad (2.89c)$$

where $\exp(-D_{SLL} \lambda_g)$ represents the tail of the graupel spectrum.

The initiation of graupel particles is from the riming of pristine ice and snow-aggregates, i.e. rimed crystals belong to the graupel category alone in this scheme.

The mass conversion rates to graupel are equal to the riming collection rates of pristine ice with shape in (2.31, 2.36) and snow-aggregates in (2.85a).

$$QIN_{xg} = QRM_{cx} \quad (2.90a)$$

where $x \in \{i, s\}$. Also, the mean-size assumption is employed for the determination of number conversion rates to graupel, as well as a mean-density assumption to derive the sink term of pristine ice volume moment.

$$NIN_{xg} = QIN_{xg} \times \frac{N_x}{Q_x} \quad (2.90b)$$

$$VIN_{ig} = QIN_{ig} / \rho_i \quad (2.90c)$$

It should be noted that an arbitrary size for graupel embryo is not required.



Cloud droplet formation process from the collision-break-up of raindrops is adopted from CL04, and the mass and number conversion rates are

$$NBK_{rc} = NCL_{rr} \exp(a_{N7} + b_{N7}R_r + c_{N7}R_r^2) \quad (2.91a)$$

$$QBK_{rc} = \exp[a_{Q5} + b_{Q5} \ln(NBK_{rc}) + c_{Q5} \ln R_r] \quad (2.91b)$$

where NCL_{rr} is self-collection among raindrops in (2.84b). In addition, the formation rate of raindrops from the spontaneous break-up is

$$NBK_{rr} = NCL_{rr} \exp(a_{N8} + b_{N8}R_r + c_{N8}R_r^2) \quad (2.91c)$$

2.2.6 Hailstone growth/Shedding

$(QH_{drm}, QH_{wml}, QH_{wsh}, NH_{wsh})$

Both the dry- and wet-growth modes of hailstone are considered in the new scheme, except for spongy growth due to the usage of a fixed bulk density to hail category. A method from Chen and Lamb (1994b) is adopted and modified to decide which growth mode is occurring. We define a total heat by the sum of the conduction heat, latent heat, and sensible heat integrated from a reference state at melting point to be the criterion as follows:

$$H_h(T) > H_h(T_0) \equiv 0, \quad (2.92a)$$

where $H_h(T)$ is the specific total heat of hailstone particle and $H_h(T_0)$ is the specific total heat of hailstone at 0°C . (2.90a) can be expressed as a heat budget listed below

$$H_h(T) - H_h(T_0) = \frac{dH_{dcd}}{dt} + \frac{dH_{dqv}}{dt} + \frac{dH_{drm}}{dt} + \frac{dH_{dcl}}{dt} \quad (2.92b)$$

where

$$\frac{dH_{dcd}}{dt} = 2\pi N_{0h} k_a \rho_a f_{vh} (T - T_0) \quad (2.92c)$$

$$\frac{dH_{dqv}}{dt} = 2\pi N_{0h} D_v \rho_a f_{vh} [Q_v - Q_{vsi}(T_0)] L_s / AB_i \quad (2.92d)$$

$$\frac{dH_{drm}}{dt} = \frac{dM_w}{dt} [L_f + c_{pw} (T - T_0)] \quad (2.92e)$$

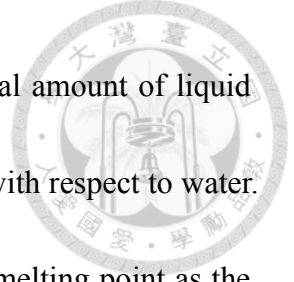
$$\frac{dH_{dcl}}{dt} = \frac{dM_i}{dt} c_{pi} (T - T_0) \quad (2.92f)$$

where k_a is the thermal conductivity of air, D_v is diffusivity of water vapor in air, $Q_{vsi}(T_0)$ is the saturated water vapor mixing ratio with respect to ice at 0°C, L_s is latent heat of sublimation, L_f is latent heat of freezing, c_{pw} is specific heat of liquid water, c_{pi} is specific heat of ice, and $dM_w/dt (=QRM_{ch} + QRM_{rh})$ and $dM_i/dt (=QCL_{ih} + QCL_{sh})$ are the collecting rates of liquid drops and ice particles mixing ratio separately by the hailstone.

If the result of heat budget in (2.92b) is less than 0, the growth of hailstone will be in the dry-mode with riming growth rate, QH_{drm} , equal to the collecting rates of liquid drops as follows:

$$QH_{drm} = \frac{dM_w}{dt} = QRM_{ch} + QRM_{rh} \quad (2.93)$$

Otherwise, the heat budget large than 0 means that the total heat of the particle exceeds that of a bulk ice particle with the same mixing ratio at 0°C. Thus, the growth of hailstone will be switched to the wet-mode. In this mode, both the bulk dry collection efficiencies for CL_{ih} and CL_{sh} become unity because melting water might accumulate on



the surface of the hailstone and form a layer of water skin. The total amount of liquid water is then determined by reexamining the total heat of hailstone with respect to water.

The heat of dH_{dcl}/dt shall be zero since we use the thermodynamic melting point as the reference state. Hence, the refined total excess heat divided by the latent heat of freezing at 0°C will be the total mass of water surrounding the hailstone, which is expressed as

$$m_w = \frac{H'_h(T) - H'_h(T_0)}{L_f(T_0)} \quad (2.94a)$$

If the amount of m_w is larger than the collecting mass of liquid drops (dM_w/dt), the extra water must be supplied from the partial melting of hailstone ice core. So the fraction of water from the melting of hailstone ice core is shown

$$QH_{wml} = \frac{dM_w}{dt} - m_w \quad (2.94b)$$

where m_{core} is the hailstone ice core for the sum of hailstone mass plus the collecting mass of ice particles. Rasmussen and Heymsfield (1987a) claimed that shedding of hailstone may occur when the mass of the water torus is greater than a critical mass shown

$$m_w^* = 0.268 \pm 0.1389m_{core} \quad (2.95a)$$

Also, an empirical fit to Fig. 8 of Rasmussen et al. (1984) is used to determine the amount of water shed:

$$QH_{wsh} = m_w - \frac{m_t}{1 + 10.67(D_h - 0.9) - 10.81(D_h - 0.9)^2 + 10.26(D_h - 0.9)^3} \quad (2.95b)$$

where m_t is the total mass of the particle and D_h is the mean volume diameter of the



hailstone in centimeter. The water that is shed is then turned into raindrops. The change in number due to shedding is derived by assuming a mean size for the shed drops which has been observed to be from 0.5 to 2.0 mm in diameter with a modal size of 1 mm (Rasmussen and Heymsfield 1987b). Thus, the number of shedding raindrops is obtained by

$$NH_{wsh} = \frac{QH_{wsh}}{a_{mr} D_{shed}^3} \quad (2.95c)$$

where a_{mr} is the parameter of m - D relation for raindrops and diameter of shed raindrops, D_{shed} , is assumed to be 1 mm.

2.2.7 Melting of frozen particles

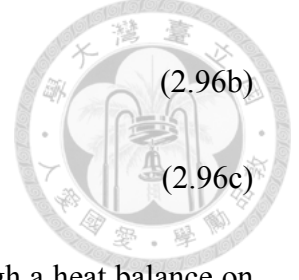
($QML_{ir}, QML_{ic}, QML_{sr}, QML_{gr}, QML_{hr}, NML_{ir}, NML_{ic}, NML_{sr}, NML_{gr}, NML_{hr}, FML_{ir}, FML_{ic}, VML_{ir}, VML_{ic}$)

The melting of frozen hydrometeors, especially for large particles, is a major source of the production of raindrops with associated cooling due to the fusion of latent heat. In the new scheme, pristine ice with the bulk mean volume diameter $> 100 \mu\text{m}$ instantaneously melts to raindrops, and others melts to cloud droplets, upon falling into regions of air temperature larger than the melting point at 273.15K. Hence the sink rates of mass, shape, and volume moments are indicated, respectively

$$QML_{ir}, QML_{ic} = -1 \times Q_i / \Delta t \quad (2.96a)$$

$$FML_{tr}, FML_{lc} = -1 \times F_i / \Delta t \quad (2.96b)$$

$$VML_{tr}, VML_{lc} = -1 \times V_i / \Delta t \quad (2.96c)$$



For the other frozen particles, the melting rates are calculated through a heat balance on the surface of hydrometeor, including the diffusion of heat to the surface of the melting particles and the transfer of sensible heat during riming collection of cloud and rain water. The evaporation of melting frozen particles is separately calculated in (2.82e) in the condition of sub-saturation with respect to water above the melting point. As a result, the sink rate of mixing ratio is resulted from the sum of conduction heat and sensible heat as follows:

$$QML_{xr} = [2\pi N_{0x} k_a \rho_a f_{vx} (T_0 - T) + c_{pw} (T_0 - T) (QRM_{cx} + QRM_{rx})] / L_f \quad (2.97a)$$

where $x \in (s, g, h)$. The bulk collection efficiencies of QRM_{cx} and QRM_{rx} in this condition are turned to be unity because a layer of water skin is formed surrounding the frozen particles. The derivation of number lost rate is by assuming a steady mean particle mass during melting process as shown below

$$NML_{xr} = QML_{xr} \frac{N_x}{Q_x} \quad (2.97b)$$

where $x \in (i, s, g, h)$. The number concentration of small pristine ice particles melting to cloud droplets is identical to (2.97b).



2.2.8 Remarks

In addition to the prediction of pristine ice shape and density, some major modifications on microphysical processes have been made in the new multi-moment bulk scheme, including

- 1) The aerosol dependence of ice deposition-nucleation;
- 2) Auto-conversion of pristine ice to snow-aggregates;
- 3) Rimed crystals initiated to graupel particles;
- 4) The wet growth mode of hailstone.

In traditional bulk schemes, cloud ice is assumed to be the small non-precipitation particle because it tends to be converted to other large ice particles like auto-conversion with a fixed threshold size. Actually, these threshold sizes are not realistic and might bring about some inappropriate interpretations to their simulation results. Thus, in the new bulk scheme, there are none arbitrary size used for the formation of large solid-phase particle embryo. The aggregation among pristine ice crystals is classified as the category of snow-aggregates, and the rimed amount of pristine ice or snow-aggregates are immediately converted into the graupel hydrometeor. The separation of ice-phase hydrometeors currently is by formation mechanisms, not by size anymore. Moreover, the diameter of pristine ice is allowed to grow to thousands of microns, but an upper limit of 5000 μm in mean size which is not likely to occur but is

imposed for numerical stability. These modifications contribute to a clear separation among hydrometeor categories and the possible further development in the bulk microphysics scheme.

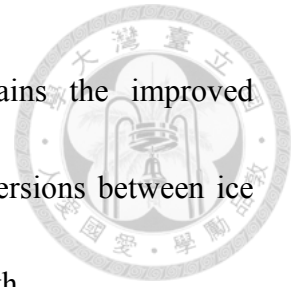


2.3 Summary

In this chapter, both the bulk ice adaptive habit parameterization and the new-multi moment bulk microphysics scheme have been proposed and summarized here. Two new pristine ice moments of shape and volume have been proposed in the ice adaptive habit parameterization, and the new approach also has been extensively applied to all ice-related microphysical processes from the initiation of ice particles, deposition growth, accretion collection, riming growth, self-aggregation, following the m - D , A - D , and v - D relationships, then the sedimentation and ventilation effect, to the three-moment closure method, as well as the orientation of pristine ice.

Besides, the new microphysics scheme predicts the mixing ratios, number concentrations, habit, and density (volume) with respect to six hydrometeor categories of cloud, rain, ice, snow, graupel, and hail, together with tracking some aerosol species. The microphysical processes of activation, nucleation, multiplication, vapor diffusion, accretion, aggregation, auto-conversion, breakup, hailstone growth, shedding, and melting are all considered. In addition to the predictions of pristine ice bulk habit and

density, some other major features to the new scheme contains the improved ice-deposition nucleation parameterizations, treatment on the conversions between ice particles, and the shedding of raindrops from the hailstone wet growth.

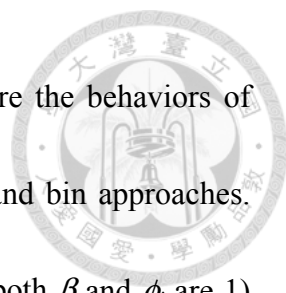




3. Zero-dimension calculations

A bulk adaptive ice habit parameterization with the 3-moment closure method has been developed and some fundamental validations are required. Many studies have demonstrated the advantages of the 2-moment over the 1-moment method, thus this study will focus on the superiority of the 3-moment method over the 2-moments methods. In this chapter, some sets of calculations in zero-dimension (i.e., parcel mode) will be conducted for validation with the bin methods. The setup for the bin method is to divide the size spectrum used for the bulk method into 100 discrete bins. The concept of initial spectrum setup for the bulk and bin methods is depicted in **Figure 3.1**.

At first, in view of the importance of spectral index, the 2-moment and the 3-moment closure bulk methods will be applied on the adaptive ice habit parameterization and validated their calculation results with the bin method as well. In the following, two distinct habit-favored growth regimes (columnar and planar) will be given at different time periods to examine the adjustment of adaptive growth ratio to changing environment using the bulk and bin methods. Furthermore, in order to distinguish a unique “shape-inertia effect” in our parameterization, some comparisons to ice crystal growth behaviors from two different initial diameters of 1 μm and 10 μm with the bulk 3-moment method will be presented. In Section 3.4, some calculations of



ice growth with the ventilation effect will be performed to compare the behaviors of large ice crystals in a high supersaturated environment with bulk and bin approaches. These calculations are performed with initially spherical particles (both β and ϕ_i are 1) with a time step of 1 second and a size spectrum with $\alpha_i = 3$. Furthermore, an off-line calculation of cloud optical depth against ice habit and solar zenith angle will be presented to examine the effect of ice shape orientation to the radiation flux.

3.1 The role of ice crystal shape and spectral index

The spectral index α is held constant (or zero) in most bulk cloud schemes whose predictions of hydrometeor distribution are limited to two moments. However, with the extension of ice crystal habit to be the third moment and the 3-moment closure technique, α_i has become prognostic in our parameterization. Thus, it is worthy to calculate the diffusional growth of shape ice under the same environment (inherent growth ratio $\Gamma(T)$ is 2.0) and initial size distribution separately with the 3-moment (α_i is prognostic) and 2-moment (α_i is fixed at 3.0) bulk methods to assess the role of α_i . Another calculation using the bin method is performed under the same condition and determines the moment values by integrating 100 bins for validation. Because no collision process is considered, the binned (size discretized) calculation represents the true results.

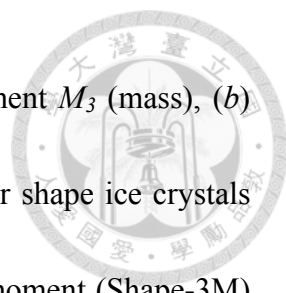
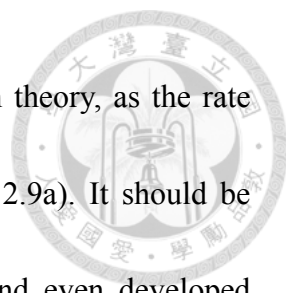
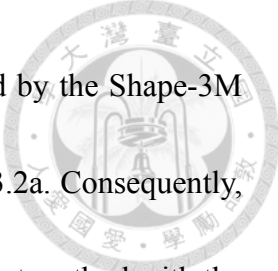


Figure 3.2 indicated the calculation results of (a) the 3rd-moment M_3 (mass), (b) the bulk aspect ratio ϕ_i , and (c) the bulk adaptive growth ratio β for shape ice crystals with the bin (Shape-bin), bulk 2-moment (Shape-2M), and bulk 3-moment (Shape-3M) methods, as well as two calculations for spherical ice separately with the bulk (Sphere-2M) and bin (Sphere-bin) approach to be the control cases. Fig. 3.2a shows that the mass moment calculated with the Shape-3M method is closer to the result of Shape-bin as compared to the other calculations. Also, the three calculations with the shape effect obviously produced larger crystals than those assuming spherical ice. Comparison between the Shape-2M (9.0×10^{-11}) and Sphere-2M (4.4×10^{-11}) shows that the difference is still very pronounced (by about a factor of two) when the number of moments used are the same. This comparison clearly reveals the ice enhanced shape effect on the mass deposition growth, so as to the comparing results of the Shape-bin and Sphere-bin.

Besides the shape effect, the difference between the bin and the bulk approaches can be attributed mainly to the restriction of the gamma size spectrum in the bulk method. **Figure 3.3** shows the evolution snapshots of all size spectrums (with the α_i value indicated for the bulk methods) at the starting 200 seconds with the interval of 40 seconds. One can see that both the spectrums with the bin methods gradually become narrowed, and the growth of bins with the shape effect (in solid black) is even more




significant. This feature is in accordance with the diffusion growth theory, as the rate change of size is inversely proportional to the size itself (cf. Eq. 2.9a). It should be noted that the spectrum of Shape-bin becomes uneven at 120s and even developed spike-like feature at 200s. This unique feature is due to the fact that smaller ice crystals have less spherical-shape memory and thus can grow faster than the originally largest particles. When the smaller crystals catch up with the larger ones, the number density (number divided by the size width) will increase dramatically. Further illustrations of this will be given in Fig. 3.6. For the bulk 2-moment calculations, the α value and thus the spectral widths are held constant, which violates the requisite of spectral narrowing during diffusional growth. This is one of the major error sources for the 2-moment gamma distribution (as well as the Marshall-Palmer distribution). On the other hand, the Shape-3M spectrum does become narrower within 80s, which can also be realized from the increase in the value of α from 3.0 to 100 which is the maximum value that yields stable solution to Eqs. (2.63) and (2.64) under the precision of our numerical method. After 80s, the growth of spectrum is not able to get narrower anymore due to the upper limit of α at 100. At this time, the calculation is essentially the same as the 2-moment method. Actually, a higher limiting value of α may be allowed by implying better numerical methods, which permits the spectrum to evolve narrower. But this contributes little to the mass moment value (figure not shown). Above results



demonstrate that Shape-bin has the most flexible spectrum, followed by the Shape-3M and the Shape-2M, according to the results of mass moment in Fig. 3.2a. Consequently, it suggests that the accuracy can be obtained by applying the 3-moment method with the adaptive habit parameterization.

As for the bulk adaptive growth ratio β , in the three Shape runs, it can rapidly adjust to the given value of $\Gamma(T)$ with a remarkable agreement, and the adjusting speed for Shape-bin is a little bit faster than that of the Shape-bulk due to its advantage of highly flexible spectrum. Note that the final β values of Shape-bin (~ 1.93) and Shape-3M (~ 1.92) are both slightly less than 2.0, indicating the inertia (memory) of their originally spherical shape. **Figure 3.4** shows β in each bin for Shape-bin calculation at the starting, 1000s, and 5000s, respectively. The values of β from bin 1 to bin 20 at smaller size reached 2.0 in both Fig. 3.4b and Fig. 3.4c, while the rest of the bins show decreasing β with increasing initial size. This also indicates that the initially larger spherical ice crystals would require longer time to change its habit. Moreover, the β in the Shape-2M run continuously rises to 2.0 due to its unrealistic broadening in the spectrum, which brings some error to the moment values (some demonstrations will be given in Section 3.4). The above results also revealed a size-dependent crystal growth rate in the adaptive habit parameterization, and will be elaborated further in the following sections. For the bulk aspect ratio ϕ_i , the differences in mass moments



between the Shape-bin and the Shape-bulk calculations are reduced evidently. In our ice habit parameterization, the derivation of ϕ_i is to divide M_ϕ by M_3 , and both moments are the 3rd-moment-weighted quantities. Thus, the errors arise from the numerical limitation of M_ϕ and M_3 tend to cancel out when calculating the ϕ_i . The minor differences among them will be discussed in more detail in Section 3.4.

Accordingly, the mass moments of non-spherical ice crystals are apparently larger than that in spherical ice calculations, and this enhancement in diffusional growth rate due to the enlargement of electrostatic capacitance is well captured by our scheme. Also, with the more flexible spectrum, the 3-moment results are obviously matching better to the Shape-bin's than the 2-moment calculations. Accordingly, the spectral index α_i does play an important role and the bulk 3-moment approach is desirable in our ice adaptive habit parameterization.

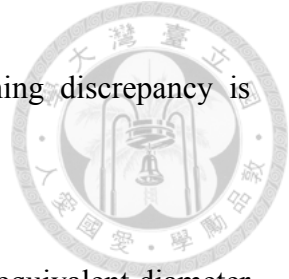
3.2 Adaptive growth

A main objective of this study is to develop a method to allow realistic transition of ice habit according to changes in environmental conditions. To test this effect, two distinct growth regimes are assigned for different growth stages: column regime with $\Gamma(T)=2.0$ before the 200 seconds and plate regime with $\Gamma(T)=0.5$ after the 200 seconds. Three calculations were conducted, one with the bin method (Shape-bin), and

the others with the bulk method using 2-moment (Shape-2M) and 3-moment (Shape-3M) representations.



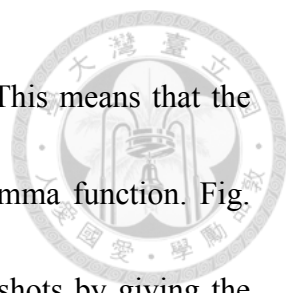
Figure 3.5 shows that both the bulk methods produced transition of shape (indicated by both ϕ and β) similar to that produced by the bin method. In the early stage the values of β instantly jumped from spherical to columnar types and reached the peak aspect ratio at 200s (1.85 for Shape-2M and 1.82 for Shape-3M), and then decreased gradually toward the 0.5 value in response to switch of environment condition $\Gamma(T) = 0.5$. Also, the final bulk aspect ratios were just less than 1.0 as planar ice (0.95 for Shape-bin; 0.85 for Shape-3M; 0.82 for Shape-2M). The higher the peak β was (such as in Shape-bin), the slower it decreases. At the end of 5000s, β reached 0.92 for Shape-2M and 0.94 for Shape-3M as comparing to the 0.98 for Shape-bin calculation. Note that the value of β is expected to decrease continuously toward 0.5 if infinite time is given. The same conclusion will hold if the environment switches from a planar regime to a columnar one. Thus, in our ice habit parameterization, β is not only the prognostic variable but also retains the growth history of the ice crystal. It means that a larger (and more aspheric) columnar ice crystal will take more time to evolve into a planar ice, which we called the shape inertia (or shape memory) effect. Although the adaptive growth in both Shape-bulk runs are a bit slower than that in the Shape-bin run, the overall performance of Shape-3M is still significantly better than Shape-2M from



the moment values mentioned above. The reason for the remaining discrepancy is explained below.

Fig. 3.6a and 3.6b exhibit the Shape-bin's calculation of β and equivalent diameter D_i for each bin at 200s and 5000s. At 200s, the D_i increased gradually from 16.3 μm at bin 1 to 26.4 μm at bin 100, consistent with the original size order. Note that the values of β for the first 23 bins were already kept at 2.0 because of the small shape memory (they are almost instantaneously adjusted to 2.0 after the diameter reaches $> 6 \mu\text{m}$, figure not shown) and then reduced steadily to 1.13 at bin 100. It revealed that the β of small ice particle is more easily adjusted to the given value of $\Gamma(T)$ than the larger crystals. A unique feature worthy of mentioning is the nonlinear distribution of particles size at 5000s, with 98.5 μm in the first bin, reduced to 86 μm around bin 40, and slightly rise to 87 μm in the last bin. The spectrum of β has a similar variation, with the maximum of 1.1 at bin 1 and the minimum of 0.82 near bin 90. These results again demonstrated the shape inertia effect, as the smallest ice crystals adapt more easily with environment changes and, in this case, developed a more aspherical shape during the later stage of growth. More aspherical shape means higher growth enhancement factor $f(\beta)$ and thus allowing faster growth. This also implied a growth dependence on the initial size of crystal, as demonstrated next.

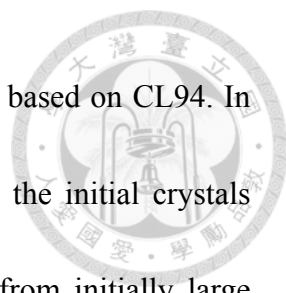
In Fig. 3.6b, one may notice that the originally smaller particles overrun those in



the higher bin numbers in the size axis during deposition growth. This means that the size distribution becomes twisted and does not follow well the gamma function. Fig. 3.6c depicts the evolution of Shape-bin spectrum at five time snapshots by giving the number density values of 100 individual bins (see caption for more detailed description). It clearly shows an extreme condition of size narrowing from bin 21 to 40 (in orange triangle) at 200s, resulting in a peak number density above 10^{11} m^{-4} . Also, the sizes of bin 1 to 20 (in red circle) overrun the other bins at 1000s, and thereby formed a twisted and folded spectrum. After that period, bin 1 to 40 keep growing to even large sizes, while the rest of the bins tend to stay in the similar sizes. The above results are consistent with the two-tailed-peaks of bin spectrum in Fig3.6b. Therefore, the gamma distribution assigned to Shape-3M calculation cannot adequately represent the true size distribution, and this is the main reason why there is still an obvious discrepancy in the Shape-3M results than the binned calculation as shown in **Figure 3.5**, as well as in Fig. 3.2 and Fig. 3.9. We can call this the inherent error for the gamma distribution when dealing with the peculiar “size overrun” phenomenon.

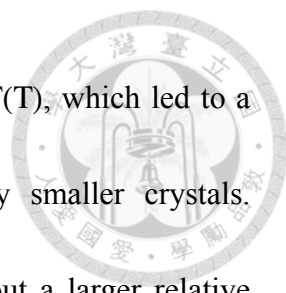
3.3 Ice growth dependence on initial size

The previous analyses indicated that the ice growth behavior is sensitive to the initial size of crystal. Sheridan et al. (2009) simulated the ice crystal evolution and



predicted the ice size spectrum using a considering the shape effect based on CL94. In their results, more exaggerated shapes were shown to result when the initial crystals were small, whereas more isometric shapes were found to result from initially large crystals. **Figure 3.7** is a schematic reproduced from their paper to depict the increase in aspect ratio over certain time steps due to vapor diffusional growth for two ice particles with different initial sizes. A larger increase in aspect ratio for the initially smaller sphere was obtained because of the larger relative increase in volume (dV/V). Hence similar calculations should be conducted in this study for comparisons.

Figure 3.8 represents growth history for two groups of initially isometric crystals with bulk mean volume diameters of $1 \mu\text{m}$ and $10 \mu\text{m}$, respectively, under the given the condition of $\Gamma(T) = 2.0$ using the 3-moment bulk method (without the isometric growth restriction under $6 \mu\text{m}$). It shows that the initially smaller particles produce larger and more aspheric particles at the end. The increases in ϕ_i for the large spheres were from 1.0 to 5.26, whereas the bulk value of ϕ_i for small spheres was significantly increased to 13.3. Also, the D_i for the initially small spheres was eventually become larger ($109 \mu\text{m}$) than the one for the large spheres ($98 \mu\text{m}$) in the end of calculations. Moreover, the starting change rate of the bulk β was faster (slower) for the initially smaller (larger) crystal even when there was no obvious difference between them at the end. In our ice habit parameterization, new depositional growth volume was disproportionally added to



the crystal faces of D_{ia} and D_{ic} through the partition according to $\Gamma(T)$, which led to a larger relative increase in bulk volume (dV/V) for the initially smaller crystals. Moreover, the larger relative increase in bulk volume brought about a larger relative increase in bulk aspect ratio ($d\phi_i/\phi_i$), as well as the increase in β . Since β of the initially smaller crystals got raised, the mass deposition growth rate accelerated through the increase in the shape-induced growth enhancement factor $f(\beta)$ shown in **Figure 2.1**. These results from grouped ice particles using the bulk method developed in this study are consistent with those of Sheridan et al. (2009) for a single particle.

These above results demonstrates that the influence of bulk ice aspect ratio on the evolution of crystal size spectra and the growth dependence on their initial mean size during vapor depositional growth, and such interactions can be well-captured by our ice habit parameterization.

3.4 Ice growth with ventilation effect

For simplicity, the above calculations were done for a moderately supersaturated environment, and the growth of ice particle diameter was limited to below 100 μm . In this size region, the effect of ventilation is minor so the f_{vi} was assumed to be unity. However, in the real atmosphere, ice crystal can grow to hundreds and even thousands of micrometers for which the effect of ventilation is expected to be significant.

Therefore, some calculations with the ventilation effect in (2.60) are conducted in the same environment conditions given in Section 3.1 except for a five times supersaturation over ice.



Figure 3.9 depicted the calculation results of (a) the 3rd-moment M_3 , (b) the bulk aspect ratio ϕ_i , (c) the bulk adaptive growth ratio β , and (d) the mean volume diameter D_i for shape ice crystals with the bin (Shape-bin), bulk 2-moment (Shape-2M), and bulk 3-moment (Shape-3M) methods, as well as a calculation for spherical ice with the bulk approach to be a control case (Sphere-2M). On the contrary to **Figure 3.2**, the mass moments of the bulk-with-shape calculations (Shape-2M and Shape-3M) are larger than those from the binned calculations, with Shape-3M being closer. It should be noted that in Shape-2M its β is straightly adjusted to 2.0 near 1800 seconds (unsmooth curves are attributed to the upper limit of 2.0 that β has reached here), whereas the values in Shape-3M and Shape-bin are approximately retained to 1.8 due to the shape-inertia effect. It looks that the adjusting strength of β obviously becomes stronger for the Shape-2M when considering the effect of ventilation. This is because that the ventilation effect is stronger for larger particles, yet the unrealistic broadening of the Sphere-2M spectrum created unrealistic larger particles (the extended tail of fixed spectrum in Fig. 3.3). Hence, this unreal forcing from the ventilation effect enhances the adjusting strength of β , and thereby results in the overestimated mass moments and bulk

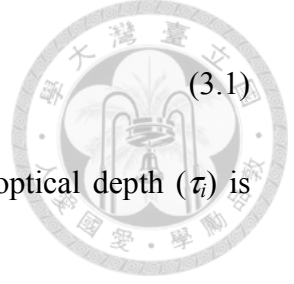


ϕ_i . By allowing α to vary, the Shape-3M method avoided the artificial broadening of the size spectrum and the overestimation of the ventilation effect, so its results corresponded better with the binned calculations.

Again, both the mass moment values of the Shape-bulk ice crystals are larger than the one of Sphere-2M inclusion of the ventilation effect. Part of the cause is the “size overrun” effect discussed in Section 3.2. But the results of Shape-3M is still close to those of the Shape-bin’s, indicating that the “size overrun” effect can be reduced with an extra moment (to allow α to vary). Note that, the ice shape effect on the fall speed was included in **Figure 2.3**, but the ventilation coefficients for falling ice crystals has not been considered explicitly yet in our ice habit parameterization.

3.5 Ice crystal shape effect on radiation flux

In the radiation schemes, the effective radius of hydrometeor particles is an important parameter on their flux calculation. For an example of the Goddard radiation scheme, Chou and Suarez (2002) parameterized the bulk extinction coefficient (β_v), single-scattering albedo (w_v), and asymmetry factor (g_v) of ice particles to be a function of the effective particle size (r_e) from a mixture of ice habits, ice water amount, and spectral band with an improved geometric optics method. In their scheme for WRF version 3.4.1, β_v is a function of r_e as shown below



$$\beta_v = a_0 + a_1 r_e^{-1} \quad (3.1)$$

where $a_0 = -6.59 \times 10^{-3}$ and $a_1 = 1.65$. Furthermore, the cloud ice optical depth (τ_i) is derived from the product of β_v , Q_i , and z as follows:

$$\tau_i = \beta_v Q_i z \quad (3.2)$$


where Q_i is cloud ice mixing ratio, and z is the geometric thickness of a cloud layer.

However, in their scheme, the effective radius of ice crystals is oversimplified to be a function of air temperature like

$$r_e = 125 + (T - 243.16) \times 5 \quad (3.3)$$

A better calculation of ice crystal r_e should be based on the detailed size distribution, and can be easily derived as M_3/M_2 . Of course, both M_2 and M_3 can be affected by crystal shape. The derivation of r_e related to crystal habit and solar zenith angle has been proposed earlier in this study. An off-line calculation was conducted by using (2.75), (3.1), and (3.2) to examine the relationship of oriented ice shape to the radiation flux.

Figure 3.10 depicted the larger value of cloud ice optical depth near noontime ($\theta_s \sim$ zero) as the ice crystals shape deviate significantly from a sphere. Given the specific conditions of ice equivalent diameter ($100 \mu\text{m}$), mass ($4.71 \times 10^{-6} \text{ kg}$), number (10^4 m^{-3}), bulk density (900 kg m^{-3}) and size distribution (see caption for detail setup), the optical depth varies from 10^{-3} for a sphere to 10 for extreme shapes of ice even before the effect



of ice habit on β_i is considered. For real-case simulations discussed in the next chapter, the value of r_e is determined with the new microphysics scheme and coupled with the Goddard radiation scheme in the WRF model. Preliminary simulation results of surface radiation flux will be discussed in Section 4.1.

3.6 Summary


Some key findings in the theoretical validation of proposed ice adaptive habit parameterization are summarized as follows:

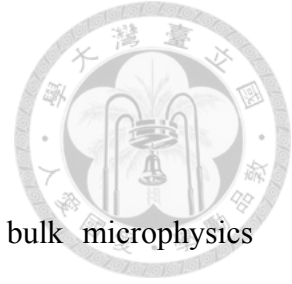
1) The enhanced ice diffusional growth rate by crystal shape effect is demonstrated by the adaptive habit parameterization for the bin and bulk methods both, as well as the realistic transition of ice habits in response to changing environmental conditions

2) Although the gamma distribution cannot adequately represent the true size spectrum, the results of Shape-3M are close to those of the Shape-bin's in all the calculations.

It indicates that α_i does play an important role and suggests using the 3-moment method in the ice habit parameterization.

3) The influence of ice crystal aspect ratio on the evolution of ice size spectra and the growth dependence on its initial size during vapor depositional growth are considered in the ice habit parameterization, and the calculation results are consistent with the conclusion of Sheridan et al. (2009).

- 
- 4) The bulk methods would result in an overestimated moment values when considering the ventilation effect and the discrepancy is much stronger for the 2-moment calculation because of the fixed spectral index.
- 5) The effect of ice habit on the optical depth is significant in our calculation, even that the shape effect on the bulk extinction coefficient (β_v) has not been explicitly considered yet.

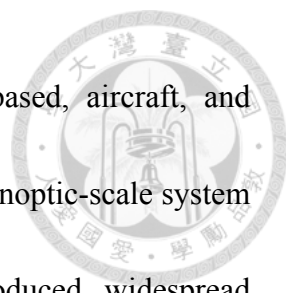


4. The WRF model simulation results

The above discussed 6-class hydrometeors and 2-moment bulk microphysics scheme with gamma-type size distribution and an additional growth-habit moment for pristine ice have been implemented into the WRF model version 3.4.1. In this chapter, applications of this new microphysics scheme are demonstrated and validated with observations. A synoptic snowfall event of C3VP in Canada and a cold-front case of DIAMET in England both are selected for simulations, and they are separately introduced in Section 4.1 and 4.2.

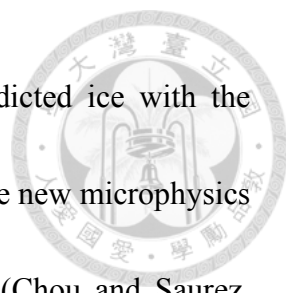
4.1 C3VP synoptic snowfall event

The parameterization of ice-phase microphysics is known to contain many uncertainties in bulk cloud schemes. In particular, the effect of ice crystal habit was largely ignored. This effect is expected to be significant for high-latitude storm systems in which the precipitation is dominant by solid-phase particles. Hence a snowfall event on 22 January 2007 observed during the field campaign of the Canadian *CloudSat*/Cloud-Aerosol Lidar and Infrared Pathfinder Satellite Observation (CALIPSO) Validation Project (C3VP) is selected for simulation with observational validation. The C3VP campaign took place in South-central Ontario in Canada for the purpose of



validating *Cloudsat*/CALIPSO retrieval algorithm using ground-based, aircraft, and remote-sensing observations. The snowfall event was caused by a synoptic-scale system with a surface low moved across the C3VP region and produced widespread light-to-moderate precipitation. A numerical study by Shi et al. (2010) has revealed the features of weak vertical velocity and therefore the absence of large liquid precipitating particles in this case. Although their WRF model simulation results using the Goddard microphysics scheme in 1 km horizontal resolution captured the cloud macrostructure well, the statistical comparisons between observed and simulated radar echoes showed a high bias of several reflectivity decibels in the model results. Hence they suggested additional research is needed to improve the current cloud microphysics scheme for simulating cloud and precipitation formation in such a high-latitude cold environment. A follow-up study was done by Iguchi et al. (2012) who used a spectral bin microphysics scheme in the WRF model, in which fixed relationships between bulk density and equivalent radius were assumed for six ice-phase hydrometeor categories. More detail descriptions to the campaign and the above two numerical studies can be accessed at <http://pmm.nasa.gov/node/128>. Here, we re-examine this event using the new microphysics scheme to evaluate the importance of ice crystal shape.

Three simulations were designed: (1) ice crystals are assumed to be spherical with a fixed bulk density of ρ_{i0} (referred as Sphere-2M run), (2) habit-predicted ice with the



2-moment method (referred as Shape-2M run), and (3) habit-predicted ice with the 3-moment method (referred as Shape-3M run). The detail setup in the new microphysics and the Goddard Space Flight Center (GSFC) radiation schemes (Chou and Saurez, 1999) with respect to these three model runs are provided in **Table 9**.

4.1.1 Model setup

The time of simulations were all from 21 to 23 January, running for 48 hours with a spin up time of 6 hours utilizing the National Centers for Environmental Prediction (NCEP) final analysis 1×1 degree data for the initial and boundary conditions. Three nested domains were constructed with horizontal grid resolutions of 20, 4, and 1.33 km and corresponding number of grid points of 90×75, 141×141, and 154×154 for the outer, middle, and inner domains, respectively. In the vertical, 50 layers were used with a model top at 100 hpa in the terrain-following sigma coordinate. The model domain setup and terrain height is depicted in **Figure 4.1**.

As to the physics options, the Tiedtke cumulus scheme (Tiedtke, 1989; Zhang et al. 2011) was used but only for the outer domain; for the planetary boundary layer parameterization, the Yonsei University (YSU) scheme (Hong et al. 2006) was applied for three domains; the GSFC longwave and shortwave schemes (Chou and Saurez, 1999; Shi et al. 2010) were employed for radiation calculations performed every 20 minutes.

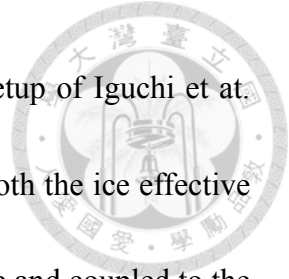


The physics options used for this case are summarized in **Table 10**.

Also, in such a high-latitude cold environment, the usage of the over-simplified collection efficiency among pristine ice in (2.44) may not be appropriate, because the size distribution, fall speed, and habit of ice particles are not considered explicitly. Furthermore, most of the current schemes assume that the collection efficiency in (2.44) consists of only the temperature-dependent function of E_c . This simple empirical equation tends to bring about unexpectedly strong snow-aggregates formation even among very small cloud ice crystals at high altitudes. Thus, for simplification, the self-collection efficiency E_{ii} among pristine ice is set as zero in this case study. Some further improvements on the ice aggregation process are required for future work.

For aerosol initial condition, the CN composition was assumed to be ammonium sulfate with a tri-modal lognormal size distribution in the clean continental type from Whitby (1978), and was horizontally homogeneous and to decrease exponentially in the vertical with a scale height of 3.57 km except for the lowest three sigma levels or below 850 hPa, where constant aerosol number concentration was assumed (cf. Cheng et al. 2007). The primary production of ice crystals follows the implicit parameterization of DeMott et al. (2010) for deposition and condensation-freezing nucleation with a given potential ice nuclei number concentration of 500 per liter. Immersion freezing of supercooled liquid drops was based on Bigg (1953), while the contact-freezing

nucleation was turned off in the simulations following the model setup of Iguchi et al. (2012). Homogeneous freezing of liquid drops also was included. Both the ice effective radius and bulk aspect ratio were derived in the microphysics scheme and coupled to the GSFC radiation scheme with inclusion of the crystal orientation.

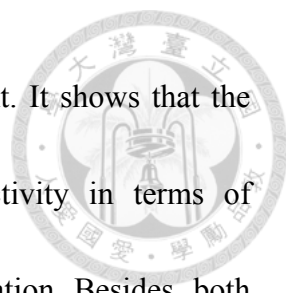


4.1.2 Simulation results

a. Precipitation and radar reflectivity

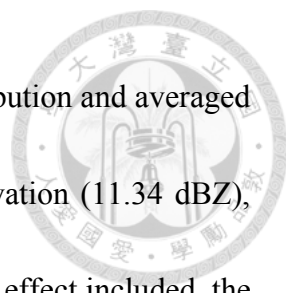
Figure 4.2 shows simulated total precipitation over the inner domain. One can see some major differences in the spatial distribution of accumulated snowfall, in particular the area with total precipitation > 3.6 mm (in red). The Shape-3M simulation evidently produced more snowfall with the domain mean of 3.04 mm around the southwest region as compared to the other two model runs (2.69 mm for Sphere-2M and 2.73 mm for Shape-2M). Also, the difference in the time series of domain-mean surface precipitation among the three model runs is obvious. The peak precipitation rate in Shape-3M (0.470 mm hr^{-1}) got stronger and occurred earlier than in the other two runs (0.421 mm hr^{-1} for Sphere-2M and 0.408 mm hr^{-1} for Shape-2M). Above preliminary results revealed that the crystal shape effect with the 3-moment bulk approach is quite significant on accumulated snowfall in this case study.

Figure 4.3 exhibits the snapshots of maximum radar reflectivity vertical profile



from the three model runs and from the C-band radar measurement. It shows that the Shape-3M simulation has the best performance in radar reflectivity in terms of horizontal distribution and echo intensity comparing to the observation. Besides, both the simulation results of Sphere-2M and Shape-2M runs look somewhat overestimated in the northwest region. Moreover, as depicted in **Figure 4.4**, the overall patterns of the latitudinal averaged radar reflectivity showed more consistency with radar observations in the two Shape model runs, particularly in the vertical distribution (echo top at 5~6 km) and echo intensity (maximum dBZ within 10~20). Although the simulation result of Sphere-2M run also got similar pattern in vertical distribution, the overall echo intensity was clearly overestimated by 5~10 dBZ. Thus, the overall cloud macrostructure of this weak snowstorm was generally captured in the model results, in particular in the Shape-3M run.

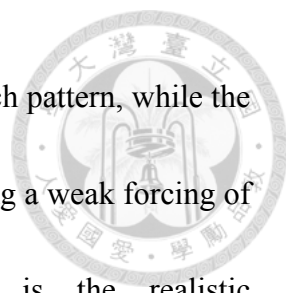
A statistical comparison of radar reflectivity using the Contoured Frequency with Altitude Diagram (CFAD) between the three model runs and observation is displayed in **Figure 4.5**. All the distributions at frequency larger than 0.2 (unit: per dBZ per km; in light green) are located in the magnitude of 0~25 dBZ, while the top altitudes of core for the model runs of Sphere-2M and Shape-2M (~6 km) are a bit higher than the 5 km in the observation. It should be noted that a certain amount of echoes within 10~25 dBZ exist in the Sphere-2M run from 6 to 3 km, and an evident overestimation between 0



and 15 dBZ in the Shap-2M run above 6 km. Also, the general distribution and averaged magnitude (13.38 dBZ) of Sphere-2M run got stronger than observation (11.34 dBZ), together with the lowest correlation of 0.783. Yet, with the ice shape effect included, the correlations of Shape-2M (0.880) and Shape-3M (0.906) runs were certainly improved, especially in the latter one which has an average magnitude of 11.01 dBZ. Many possible causes may contribute to these discrepancies between the results of model and observation. For example, the size distributions of the ice-phase precipitation may deviate significantly from the gamma distribution because of an inflexible spectral index assumed in the model. Of course, the inaccuracy in microphysical mechanisms, such as cloud ice and snow aggregation, cannot be ruled out. It is also possible that the radar observation might not have a complete spatial coverage owing to its limitation in scanning angle and attenuation. Nevertheless, above comparisons indicated that the adaptive habit with the 3-moment method tends to reduce the high bias in strong echoes, and thereby produced more consistent results to the measurement shown in Fig. 4.5(d).

b. Pristine ice growth habit

Figure 4.6 shows a few time slices of the limited domain-averaged pristine ice aspect ratio around the passing period of leading snowstorm from the Shape-2M and Shape-3M model runs. Both Fig. 4.6(a1) and Fig. 4.6(b1) indicate that non-spherical



crystals are suspended mostly above 2 km in a three-layered sandwich pattern, while the height below 2 km is dominated by isometric ice (in orange) implying a weak forcing of shape on deposition growth there. Also can be noted is the realistic temperature-transition between the planar (in green or blue colors) and columnar crystals (in red or pink colors). But some randomness of the growth habit regime can be found between altitudes of 2 km to 6 km, indicating the shape memory effect. With the air mass subsiding, both the layers in columnar type are getting lower in the altitudes of 0.2-5 km which is within the plate-favored temperature region of -11°C to -20°C as show in Fig. 4.6(a3) and Fig. 4.6(b3). It should be noted a distinct discrepancy exist in the columnar crystals initially existed above the -20°C height between these two model runs. In the Shape-2M run, these columns are gradually evolved into planar ice (Fig. 4.6-a4), whereas they remain as the columnar type in the Shape-3M run (Fig. 4.6-b4) because of the more accurate shape memory effect. The comparison is consistent with the conclusion given from the adaptive growth calculation in Section 3.2, and also implies a different and even opposite result may be obtained with different bulk approaches for ice shape.

Consequently, these model results initially demonstrated the capability of adaptive ice habit simulation in the new microphysics scheme, besides, the bulk ice shapes are able to evolve freely from 0.1 to 8.0 in the simulation results, not merely a fixed value

assumed in some early studies.



c. Hydrometeors and production rates

Some inner-domain-averaged vertical profiles of the hydrometeor mass mixing ratio, number concentration, effective radius, and production rate are illustrated from **Figure 4.7** to **Figure 4.10**, respectively. Although this is a weak snowstorm case, Fig. 4.7, Fig. 4.8, and Fig. 4.10 still evidently show the enhanced effect by crystal shape on the mass mixing ratio, number concentration, and deposition rate in the Shape-2M and Shape-3M runs. The shape enhanced effect in the Shape-2M is a bit weaker than in the Shape-3M run due to restriction of the fixed spectral width, as demonstrated in the calculations shown in Section 3.1. The ice shape effect also obviously contributes to the high values of pristine ice maximum bulk effective radius (ranging from 80 μm to 130 μm) below 2 km, together with a reduction above 3 km in the Shape-3M run because a higher amount of ice number concentration is produced there. Also, with the larger size (or geometric cross-section) of aspherical pristine ice, the collisions between ice crystals and the other hydrometeors would get enhanced (disregard of the effect on terminal velocity), and thereby lead to lower mixing ratio and number concentration of cloud droplets, rain drops, graupel, and hail particles together with smaller bulk sizes. This is why the ice shape effect either with the 2-moment or 3-moment method is able to



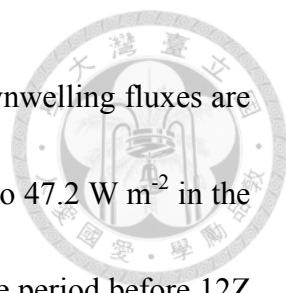
reduce the strong echoes and produced a better pattern correlation ratio as listed in Fig.

4.5.

Since the collection efficiency among ice crystals has been set as zero in this case, no aggregate-relevant information is shown. The enhanced riming growth rates of the Shape-2M and Shape-3M runs could be simply a result of extended geometric cross-section when considering ice crystal shape. However, this shape enhanced effect in the Shape-3M run is also limited below 3 km due to the limited amount of cloud droplets over there. Also, the lower ice multiplication production (ice splintering) rates in the Shape-2M and Shape-3M runs are resulted from the weaker riming of graupel due to its smaller size. The increased deposition-nucleation rate and reduced freezing rate around 5 km might be resulted separately from a higher supersaturation and a warmer temperature due to the release of latent heat from the enhanced ice deposition growth over there. The above results suggested that the ice habit does have significant impact on the microphysical processes particularly in the deposition growth and riming collection. This mechanism affects the mass, number, and size of all hydrometeor particles in this case study.

d. Surface radiation fluxes

Figure 4.11 is the time series of the inner-domain-averaged surface radiation

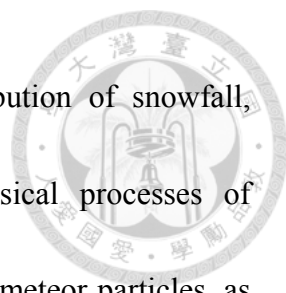


fluxes. It looks that the fluctuations in shortwave upwelling and downwelling fluxes are moderated by crystal shapes with the maximum differences of 23.3 to 47.2 W m⁻² in the Shape-2M run and -24.1 to -43.6 W m⁻² for the Shape-3M run for the period before 12Z 22 January. With the getting away of the snowstorm on the second day (22 January), some distinct differences with peak values about 45.4-89.4 W m⁻² (28.3%~25.9%) and 62.3-112.7 W m⁻² (38.9%~32.6%) are found for the Shape-2M and for the Shape-3M runs, respectively. Also, the surface longwave radiations between the Sphere-2M and the two Shape runs are depicted within 4 W m⁻² for upwelling and 40 W m⁻² for downwelling fluxes. These results reveal the immense impact of crystal shapes on the surface shortwave radiation fluxes in this real case simulation even though the effect of ice habit onto extinction coefficient has not been considered explicitly in the GSFC radiation scheme.

4.1.3 Remarks

Some key findings from this snowfall case study are summarized as follows:

- 1) Even that the aggregation among pristine ice was turned off, the model simulation results still captured the cloud macrostructure of this weak snowstorm in particular to the fine correlation of CFAD for the aspherical ice with the 3-moment approach. .
- 2) The comparisons of the model results indicated that the ice habit with the 3-moment

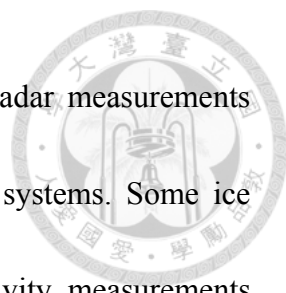


method did have some crucial impacts on the spatial distribution of snowfall, general structure in terms of the strong echoes, microphysical processes of deposition growth and riming collection, the bulk radii of hydrometeor particles, as well as the surface radiation fluxes.

- 3) The realistic transition between columnar and planar crystals is initially depicted in the model simulations, as well as the adaptive habits of ice crystals. These demonstrations suggest that the implementation of our bulk adaptive ice habit parameterization is crucial. Some further validations with observation will be performed in next section.

4.2 DIAMET cold-front event

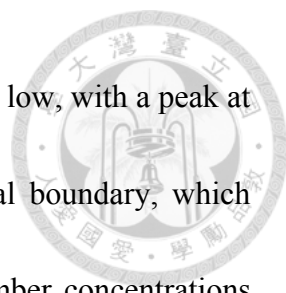
Mid-latitude cold fronts that are associated with high-impact mesoscale features of narrow rainband are difficult to forecast accurately. In such cold fronts, the mixed phase processes are critical to precipitation formation, so they are quite suitable for testing the performance of a microphysics scheme. Thus, a cold front passed through the United Kingdom (UK) on 29 November 2011 within an intensive observation period of the DIAMET (DIAbatic influences on Mesoscale structures in ExtraTropical storms) field campaign is selected as the second simulation case in this study. The DIAMET project conducted four UK-based field campaigns between September 2011 and August 2012,



providing a comprehensive set of both *in-situ* and ground-based radar measurements related to the microphysics and dynamics of a variety of frontal systems. Some ice microphysics observations provided by aircraft and radar reflectivity measurements derived from a steerable 3 GHz dual-polarization Doppler S-band Chilbolton Advanced Meteorological Radar (CAMR, 51.15°N, 1.44°W) with a narrow 0.28° beam width will be used to validate the numerical model results simulated with the new microphysics scheme.

A low pressure center at the Northeast Iceland with the associated cold front extended down across the length of UK advanced from the west. The UK Met Office rainfall radar revealed the evolution of a well-defined cold-front rainband with peak precipitation rate above 32 mm hr⁻¹ as the cold front passed through the UK. An aircraft equipped with some *in-situ* microphysics instruments like the Cloud Droplet Probe (CDP; Lance et al. 2010), Cloud Ice Probe (CIP-15, CIP-100; Baumgardner et al. 2001) and a two-dimensional stereo probe (2D-S; Lawson et al. 2006) took off at 1407 UTC and proceeded to fly legs back and forth around Exeter (50.85°N, 2.63°W) and Chilbolton (51.2°N, 1.2°W) only along the 253° (westsouthwest) radial because of air-traffic control restrictions; while the front was over land, before landing back at Exeter at 1610 UTC.

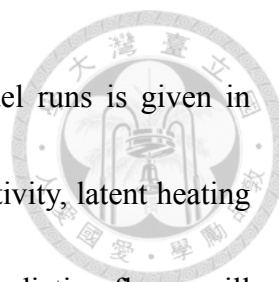
Some key points to the microphysics observations for this case study are



summarized here. The cloud droplet number concentration was quite low, with a peak at 100 cm^{-3} within the region of strong vertical motion at the frontal boundary, which implied a relatively clean air mass. In contrast, the ice crystal number concentrations were relatively high for the temperature regime within 0°C and -10°C with peak values up to 85.6 L^{-1} , whereas ice crystal concentrations were much lower (typically 1 L^{-1}) at cloud top. In addition, observations from the surface meteorological station showed that the surface cold front reached Chilbolton at 1600 UTC as indicated by the clear drop in temperature at this time, making the transition from the warm sector to cold sector air. Also, the precipitation occurred ahead of the front. More detailed descriptions to the field campaign and the cold front event can be accessed from Dearden et al. (2014), Crosier et al. (2013), and the website <https://www.ncas.ac.uk/index.php/en/diamet-introduction/>.

4.2.1 Model setup

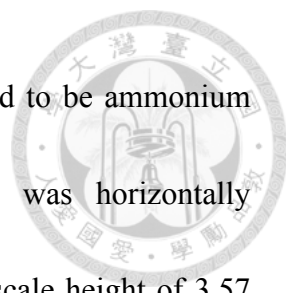
Two simulations were conducted. First with the assumption of spherical ice crystals with a fixed bulk density of ρ_{i0} (referred as the Sphere-2M run), and the other with habit-predicted crystals using the 3-moment method (referred as the Shape-3M run). The results were compared and validated with the aforementioned observations to evaluate the relative importance of crystal shape. The detailed setup in the new



microphysics and the GSFC radiation schemes to above two model runs is given in

Table 11. The model simulation results of precipitation, radar reflectivity, latent heating rate, pristine ice shape, hydrometeors, production rate, and surface radiation fluxes will be presented in Section 4.2.2, as well as some validations with observations provided by Dr. Christopher Dearden at University of Manchester.

Both simulations were integrated from 00Z to 18Z 29 November 2011 for 18 hours with a spin up length of 6 hours and utilized the European Centre for Medium-Range Weather Forecasts (ECMWF) reanalysis data for the initial and boundary conditions. Three simulation domains were constructed with horizontal grid intervals of 30, 6, and 2 km and corresponding grid points of 110×75 , 231×176 , and 301×250 for the outer, middle, and inner domains, respectively. The model was performed with 50 vertical layers and a model top of 50 hpa using the terrain-following sigma coordinate. The model domain setup and terrain height are depicted in **Figure 4.12**. As for the physics options, the Kain–Fritsch cumulus scheme (Kain, 2004) was only used for the parent domain, while the planetary boundary layer parameterization was the Yonsei University (YSU) scheme (Hong et al. 2006) for three domains. Also, the GSFC longwave and shortwave schemes (Chou and Saurez, 1999; Shi et al. 2010) were employed for radiation calculations performed every 30 minutes. A list of physics options used for this case was summarized in **Table 11**.

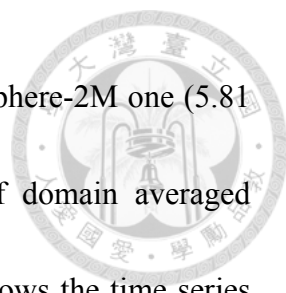


For aerosol initial condition, the CN composition was assumed to be ammonium sulfate in the clean continental type of Whitby (1978), and was horizontally homogeneous and to decrease exponentially in the vertical with a scale height of 3.57 km (cf. Cheng et al. 2007). The primary production of ice crystals was calculated with an implicit parameterization of DeMott et al. (2010) for deposition and condensation-freezing nucleation with a given potential ice nuclei number concentration of 500 per liter. Immersion freezing of supercooled liquid drops was based on Bigg (1953), while the contact-freezing nucleation was tuned off in the simulations. Homogeneous freezing of liquid drops was also included. The ice crystals are initiated as spheres with the mean diameter of 6 μm and the bulk density of 910 kg m^{-3} from either the primary or secondary ice production. Both the ice effective radius and bulk aspect ratio derived from the microphysics scheme are put into the GSFC radiation scheme with consideration of the crystal orientation versus the solar angles.

4.2.2 Simulation results

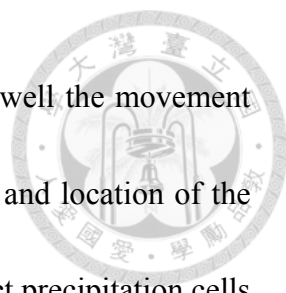
a. Precipitation and radar reflectivity

The simulation results in **Figure 4.13** depicted that the major precipitating regions were located on the coastal land area and the precipitation pattern are generally similar in these two simulations, with domain averaged accumulated precipitation reaching 5.73



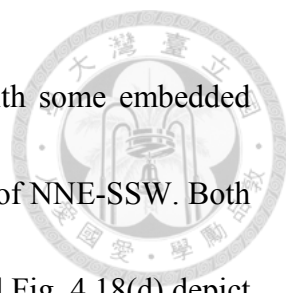
mm in the Shape-3M run, which is slightly lower than that in the Sphere-2M one (5.81 mm). Also, there is no obvious difference in the time series of domain averaged precipitation intensity between the two simulations. **Figure 4.14** shows the time series of precipitation rate at the Chilbolton surface meteorological station, and the model rainfall rates both were derived from the maximum value within the range of 0.05° around the site to minimize the spatial sampling bias. The observed onset period of precipitation began from noon till to 16 UTC with an approximated peak rate of 7 mm hr^{-1} at 14:20 UTC. The main precipitation period in both simulation results also started from 12Z to 16.5Z separately with matching peak precipitation rates at 9.6 and 7.1 mm hr^{-1} both occurred about one hour later than the observation at 15.5Z. Note that the time resolution of the observation (10 seconds) is much higher than that of the model output (30 minutes). Under the same time resolution the peak precipitation period in the model results should be even closer to the observation. Therefore, the simulations performed rather well in the timing and peak intensity of precipitation. It should be noted that a slightly weaker precipitation (around 13Z to 15Z) that was developed ahead of the narrow rain band observed from the radar images was predicted nicely in the model runs.

The observed rainfall rate (estimated from the 1 km composite radar) maps in **Figure 4.15(c)** at 14Z to **Figure 4.17(c)** at 16Z showed the passage of the rainband as it



moved eastwards across the UK. Both model simulations captured well the movement of the narrow spatial distribution of rainfall, especially the strength and location of the rainband. Also notice that embedded in the rainband are some distinct precipitation cells aligned at a NNE-SSW orientation, with rain rates above 8 mm hr^{-1} . Such distinct features can also be found in the simulation results. The precipitation rate in the model results was derived from the increased surface rainfall within an output period of 30 minutes, whereas the observed rainfall rate was estimated instantaneously by the radar at a specific scan-time period. Even that, the overall horizontal spatial distribution, the timing of movement, and the precipitation intensity of this narrow cold front system were well simulated by the new microphysics scheme. But the differences in rainfall rate between the Sphere-2M and Shape-3M runs are rather minor.

Some simulated horizontal spatial distributions of radar reflectivity at an altitude of 2 km and cross sections corresponding to the scanning path were validated with the ground-based radar observations at three time slices shown in **Figures 4.18 to 4.20**. In Fig. 4.18, the position of the narrow rainband was slanted on the northwest side about 100 km away from the CFARR radar site, with the peak intensity larger than 40 dBZ near 2.5 km within 90 and 130 km in Figs. 4.18(c) and (d). Such profiles appeared in both simulations but only the results of Shape-3M run is shown. Also, an observed wide spread of radar reflectivity with the top altitude of 6 km was correctly simulated. In Fig.



4.19, the narrow rainband just passed through the CFARR site with some embedded cores (radar reflectivity larger than 40 dBZ) and aligned in an angle of NNE-SSW. Both the simulated and observed vertical cross sections in Fig. 4.18(c) and Fig. 4.18(d) depict the distributions of > 20 dBZ cells mainly under 4 km in altitude. In addition, a bright band of peak radar signal larger than 30 dBZ randomly occurred within the altitudes of 0.5~3 km are also captured by the model. Note that the simulation produced radar echoes well above 2 km in the near distance, and below 1 km at far distance are absence in the observations due to restriction in radar scan elevation angle. At 16Z, the rainband moved to the east about 50 km from the CFARR radar site. Again, the model simulated distributions of echoes in horizontal and vertical both are corresponding to the radar observations (Fig. 4.20).

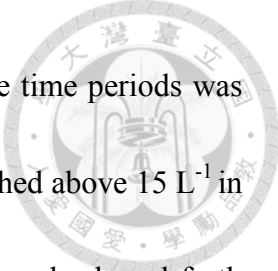
Figure 4.21 shows the radar reflectivity frequency-height distribution (CFAD) between the two model runs. The results are similar except for a higher frequency of 15 to 25 dBZ (in red) occurrence between the altitudes of 2 km and 3.5 km in the Shape-3M run. A lower occurrence (in light blue) of >40 dBZ data also was found above 2.5 km from the Shape-3M run. So, the shape effect of pristine ice tended to reduce the occurrence of high radar echoes (above 40 dBZ) and increase the medium radar reflectivity (between 15 dBZ and 25 dBZ). It is postulated that the enhanced deposition growth of cloud ice through the Wegner-Bergeron-Findeisen process tends to

depress the riming growth of graupel or snow-aggregate particles which may contribute to high radar reflectivities. Some further discussion will be illustrated in **Figure 4.31**.

To sum up, the simulation with the new microphysics scheme produced results in very good agreement with the ground-based observations for the precipitation field and the radar reflectivity. Furthermore, a major feature of the narrow rainband was well produced by the model runs in its spatial pattern, timing and intensity.

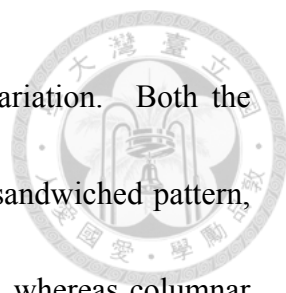
b. Pristine ice shape and latent heating rate

Some *in-situ* microphysics measurements of ice number concentration and deposition heating rate were obtained by aircraft along the flight track (see the solid black line in Fig. 4.18a for the flight track positions) from 14:14 UTC to 16:05 UTC during the DIAMET project. **Figure 4.22** and **Figure 4.23** show the vertical profiles of simulated hydrometeors along the longitudinal flight tracks in averaged between latitudes of 50.5°N ~51.5°N at the periods of 15 UTC and 16 UTC, respectively. The model simulations at 15 UTC showed that the main convective rainband located around 1~2°W has a cloud top at 9 km (about -45°C); whereas to the west there is a stratiform cloud deck with cloud top rising from about 3 km to 7 km toward the west. The convective rainband shifted eastward at 16Z (Fig. 4.23) but the overall macro-structure remained similar.



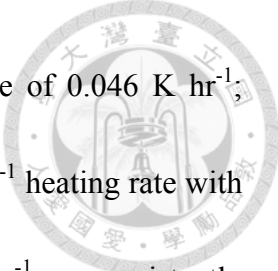
The simulated number concentration of pristine ice during these time periods was on the order of 0.01 L^{-1} to 10 L^{-1} in the convective rainband, and reached above 15 L^{-1} in the western part of the stratiform cloud. Note that the flight track was back and forth between Exeter (50.85°N , 2.63°W) and Chilbolton (51.2°N , 1.2°W), and the around-track ice number concentrations from the model are depicted in Fig. 4.24(a) and Fig. 4.24(b). These scatter plots indicate that the ice number concentration within the temperature region of $0^\circ\text{C} \sim -10^\circ\text{C}$ are relatively high, with the peak values reaching up to 212.91 L^{-1} for Sphere-2M and 82.71 L^{-1} for Shape-3M runs. The reduced ice number concentration of Shape-3M run might be attributed to the fact that more water vapor is consumed by the enhanced deposition growth of aspherical crystals which results in a lower ice supersaturation and thus weaker ice nucleation. Fig 4.24(c) presents the aircraft measurement of ice number concentration reaching to 85.62 L^{-1} around -5°C . Apparently, the Shape-3M model simulated ice crystals number concentration is more consistent with the aircraft measurements as compared to the Sphere-2M run. Besides, the simulations also produced the number of snow aggregates (typically less than 1 L^{-1} with diameters $> 1 \text{ mm}$) in good agreement with the observations (figure not shown).

In the simulated convective rainband, ice particles mean diameters are generally less than $70 \mu\text{m}$ near the cloud top above 6 km, and increased to several hundred μm within the temperature region from 0°C to -20°C (Fig. 4.22c and Fig. 4.23c). In the



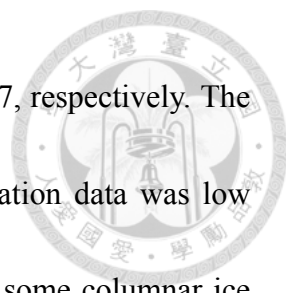
stratiform region, the ice crystal size exhibited a similar height variation. Both the simulated bulk crystal shapes in Fig. 4.22d and Fig. 4.23d show a sandwiched pattern, with planar ice dominated in the middle between -10°C and -20°C , whereas columnar ice dominated in the temperature regions above -10°C and below -20°C . There is also a limited region of plate layer just above the 0°C height. These temperature regimes agree well with the Nakaya diagram for ice crystal primary habits (Nakaya, 1954).

Latent heating is a diabatic process of immense consequence to the formation and intensification of convection. Thus, the magnitude of the latent heating rate helps to reveal the key microphysical processes that clouds impact mesoscale dynamics. **Figures 4.22e** and **4.22f** show the simulated deposition heating rates and the riming heating rates. One can see that vapor deposition is the dominant ice-phase (or mixed-phase) latent heating source, with peak heating rate reaching a few Kelvin per hour. **Figure 4.25c** presents that the derived heating rate during the flight track is between 0 and 6.176 K hr^{-1} with a mean value of 0.075 K hr^{-1} , which is dominated by the ice deposition growth (the observed heating during riming was too weak and thus is not showed here). The strongest heating ($> 3\text{ K hr}^{-1}$) occurred between the -4°C and -8°C levels, and this temperature range corresponds well with the temperature regime of the Hallett-Mossop (H-M) mechanism (i.e., -3°C to -8°C) for secondary ice production. The Sphere-2M run in Fig. 4.25(a) produced a similar heating profile, with roughly the same peak-heating



height but lower peak heating rate ($< 4 \text{ K hr}^{-1}$) with a mean value of 0.046 K hr^{-1} ; whereas the Shape-3M run in Fig. 4.25(b) produced up to 7.426 K hr^{-1} heating rate with a mean value of 0.069 K hr^{-1} . Also, heating rates of larger than 3 K hr^{-1} are consistently appeared between -4°C to -8°C in both the observed and simulated results. Consequently, the aspherical model simulation well captures the observed latent heating rate in terms of magnitude and temperature region.

In the DIAMET campaign, the aircraft was equipped with the new optical imaging instrument of 2D-S probe (Lawson et al. 2006). In this 2D-S, two orthogonal laser beams cross in the middle of the sample volume, and an overlap region is defined by the two laser beams, improving the sample volume boundaries and sizing of small particles ($< \sim 100 \mu\text{m}$) and also producing shadowgraph images with true $10\text{-}\mu\text{m}$ pixel resolution compared to conventional optical array probes. Vertical distributions (expressed in terms of temperature) of ice aspect ratio derived from the aircraft observation and model simulation were compared in **Figure 4.26**. The values of observed ice aspect ratio were interpreted from the 2D images taken within the flight track. But because the minor dimension of the planar ice crystals cannot be distinguished in the 2D images, only the columnar ice crystals with the long-axis dimension greater than $50 \mu\text{m}$ (the detection limit of the 2D probe) are compared. Despite some sampling issues, the vertical distributions of ice aspect ratio (Fig. 4.26a and 4.26c) indicated an overall agreement



from 0°C to -10°C, with comparable mean values of 1.585 and 1.817, respectively. The reliability of the low-temperature (above the -10°C height) observation data was low due to the small number of sampling. Also, it should be noted that some columnar ice do exist below -10°C in the planar ice temperature regime with a good agreement in aspect ratio values and number of sampling points (or frequency in the model) in the measurements. Furthermore, Fig. 4.26b depicts two dominant temperature regimes of simulated planar ice crystals in the vertical distribution. The more obvious regime is from -9°C to -20°C with the highest aspect ratio occurring at -16°C and the other minor one is below the -2°C height. Also can be noted the relative frequency of the planar and columnar ice crystals vary with ambient temperature, which corresponds well with the temperature transitions suggested from previous studies (Hallet and Mason 1958; Kobayashi 1961) and a recent habit diagram of Bailey and Hallet (2009).

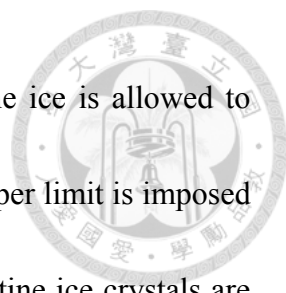
The ice crystals image taken by the 2D-S probe in **Figure 4.27** provides evidence for a large amount of columnar ice observed from the aircraft in the temperature range of 0°C to -10°C, but no aircraft observational data was made above the -14.5°C height. Also, the model simulated results in **Figure 4.22** showed a columnar ice dominant region between -1°C and -9°C. These abundant columnar crystals were produced mainly from the ice multiplication mechanism (i.e., the Hallet-Mossop secondary ice production) which is shown to occur in the temperature range of -3°C to -8°C. Both the

model and observation also showed the columns to present in the planar ice temperature regime (-9.5°C to -14.5°C), and the possible causes are the ice shape memory effect.

Note that the columnar ice crystals from the observation are mostly capped-columns, indicating a switch in the growth habit. These ice crystals were either formed earlier in the columnar temperature regime and then transported upwards from below H-M region, or they were formed in the cold columnar regime (higher than the -20°C height) and then fallen from above.

Actually, these capped-columns have been noted in the region of high differential reflectivity (Z_{DR}) identified by CAMR and appeared some form of outflow from the top of the narrow cold-front rain band from a previous cold-front case passed over the UK on 3 March 2009 (Crosier et al. 2013). Also, Crosier et al. (2013) described the major features of evidently ice multiplication with the ice particle number concentration $\sim 100 \text{ L}^{-1}$, particle sizes $\sim 400 \mu\text{m}$, particle habit of pristine columns, and temperature in the H-M regime of -3°C to -8°C. Thus, the results obtained from the model simulations and the aircraft observations in 2011's case study are well supported from the previous study of Crosier et al. (2013).

Figure 4.28 shows the simulated vertical distributions of mean diameter and apparent density as a function of ambient temperature within the flight track region. Fig. 4.28a shows that most of the pristine ice particles below -5°C height are within 1000

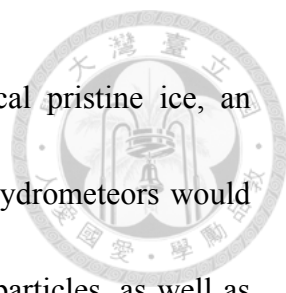


μm in diameter, but above the -5°C height, the diameter of pristine ice is allowed to reach millimeter sizes by diffusional growth because no arbitrary upper limit is imposed in the new microphysics scheme. In fact, such millimeter-sized pristine ice crystals are not uncommon in mid-latitude weather systems. In Fig. 4.28b, the ice bulk apparent density randomly varied from 100 to 910 kg m^{-3} , and lower mean apparent densities within 400 to 600 kg m^{-3} were found at above the -10°C height than below. The variation of mean bulk density with an averaged value of 646.32 kg m^{-3} is also reasonably close to the fixed value of 500 kg m^{-3} traditionally used in previous studies.

According to the above comparisons, the overall simulated ice microphysics features were quite consistent with the aircraft *in-situ* measurements, indicating a good performance of the proposed adaptive habit parameterization.

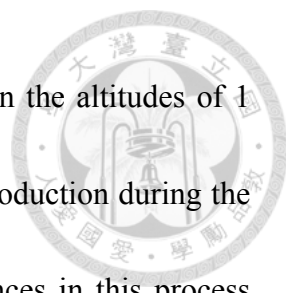
c. Hydrometeors and production rates

Some inner-domain-averaged vertical profiles of hydrometeor mixing ratio, number concentration, effective radius, and production rate are illustrated in **Figure 4.29** to **4.32**. One can see an evident enhancement in the diffusional growth (Fig. 4.32) of pristine ice crystals due to the crystal shape effect, and thereby produce not only the enhanced mass mixing ratio (Fig. 4.29) but also the bulk effective radius (Fig. 4.31). For example, the peak effective radii of cloud ice near 2 km altitude increased from $60\ \mu\text{m}$



to nearly 125 μm by one time. With the larger size of aspherical pristine ice, an enhanced collision between ice crystals and the other solid-phase hydrometeors would result in lower mixing ratio of snow-aggregates, graupel, and hail particles, as well as fewer number of snow-aggregate. The bulk effective radii of snow aggregates, on the other hand, seem to vary little possibly because the snow self-aggregation applied a mean size approximation that is not sensitive to shape in the new microphysics scheme. By using the more realistic process of ice crystal aggregation and the re-definition of snow as aggregates, the effect of shape on snow production will be more significant.

Figure 4.32 compares the domain-averaged mass production rates from the Sphere-2M and Shape-3M runs. Deposition nucleation of the Shape-3M run gets slightly larger possibly due to a higher ice supersaturation at above the 10 km height; deposition growth of cloud ice increased mainly due to shape enhancement factor in Fig. 2.1; whereas cloud ice aggregation to form snow is also significantly enhanced at above 1 km because of the extended geometric cross-section for collision. Suppressed freezing of cloud droplets around 5 km height could be due to warming caused by enhanced deposition heating. Enhancement in the riming on cloud ice in the Shape-3M run might be contributed to the extended geometric cross-section of the shaped ice crystals. Although the riming growth was not profound in this case study, its difference between the Sphere-2M and the Shape-3M runs is consistent with the assumption given in the



adaptive habit parameterization. Ice multiplication is active between the altitudes of 1 and 4 km, where the temperature range matches that for the H-M production during the riming growth of snow-aggregates or graupel. No obvious differences in this process between these two model runs. Above results suggested that ice habit does have certain impacts on the microphysical processes of deposition growth, aggregation, and riming. These changes in microphysics may affect other physical processes such as radiation and dynamics.

d. Surface radiation fluxes

No obvious difference is shown in the time series of inner-domain-averaged surface radiation fluxes between the two simulations (figure not shown), as this was a strong convection case with deep warm-cloud. Nevertheless, the effect of crystal shape on the radiation fluctuation remains significant at certain locations. **Figure 4.33** depicts the time series of averaged surface radiation fluxes around the CFARR site, and evidently maximum differences of short wave radiation fluxes (-20 W m^{-2} for upwelling and -90 W m^{-2} for downwelling) were reproduced during 10Z to 11Z 29 November 2011 between the two simulations. Also, the differences in long wave downwelling radiation fluxes reached up to 40 W m^{-2} at the periods of 8.5Z, 10.5Z, and 16.5Z. Therefore, the impact of crystal shape on the radiation fluxes is found to be great in this

case study.



4.2.3 Remarks

Some conclusions to this cold front case study are summarized as follows:

- 1) The major feature of narrow cold frontal rain band in this cold front case was well captured in the model simulation results with respect to the spatial distribution, intensity, and timing, as well as the associated embedded precipitation cores.
- 2) The columnar ice crystals initiated within the temperature region of H-M secondary ice production was clearly simulated and confirmed with aircraft observations. Also, both results are consistent to the finding of Crosier et al. (2013).
- 3) The modeling vertical distributions of planar and columnar ice crystals with specific temperature transition regimes agreed well with the diagrams for ice crystal primary habits. Furthermore, the observed capped-columns presenting in the planar ice temperature regime is also correctly simulated by the adaptive habit parameterization through the ice shape memory.
- 4) The comparisons of simulation results demonstrated the effect of crystals shape on various microphysical growth rates including the enhanced cloud ice deposition growth, formation of snow by cloud ice aggregation, and riming growth of ice crystals, together with the transmission of radiation fluxes.



4.3 Summary

In this chapter, the model simulations separately captured the cloud macrostructure of the snowstorm in the first study case and well produced the precipitation features of the narrow cold-frontal rain band in the second case. The effect of ice habits on surface precipitation was quite obvious in the solid-phase-dominant snowfall event but not in the liquid-phase-dominant cold-front system.

Both cases have showed the ice shape effect on the enhancement of deposition growth rate resulted in the larger size of pristine ice, and thereby induced the enhanced collision between ice particles and other hydrometeors. Also, above processes tended to lower the occurrence of strong echoes by the reduction of graupel or snow-aggregate size. Thus, the impact of ice habits on the microphysical structure is crucial.

The realistic evolution of ice crystals through the adaptive growth habit has been demonstrated in the snowfall simulations, while the simulated vertical distributions of pristine ice with the temperature transition regimes are quite consistent with the habit-diagram and the observations in the cold-front case. Furthermore, the observed capped-columns present in the plate-favored temperature regime are implicitly simulated by the adaptive habit parameterization as indicated by the retained ice shape memory.

At last, the simulated pristine columns initiated within the H-M secondary ice production region were quite consistent to the aircraft observations in terms of ice number concentration, latent heating rates, and aspect ratio.





5. Conclusions

5.1 Summary

This study has developed the bulk adaptive habit parameterization for pristine ice based on CL94 and also introduced the 6-class double-moment bulk microphysics scheme in gamma distribution. Both new approaches have been implemented into the WRF model forming the new multi-moment bulk microphysics scheme.

In the adaptive habit parameterization, two pristine ice moments of shape and volume have been proposed for the predictions of crystal habit and apparent density. Also, the adaptive habits are extensively incorporated into the ice-related processes from diffusional, riming, to aggregation, following the m - D , ν - D relationships, and ventilation effect, as well as the 3-moment closure method. After a lengthy effort, the improvements of ice deposition-nucleation, conversions between ice-phase particles, and hailstone wet growth have been made on the new microphysics scheme.

The zero-dimension calculations have shown the important role of spectral index, ice shape enhanced effect on the deposition growth rate, the size-dependent adaptive growth habit against distinct environmental conditions, and the influence of ice aspect ratio on the evolution of size spectra. In addition, the validations with the bin method have revealed that using the 2-moment approach inevitably produced certain errors due



to the sticking spectrum, thus, the 3-moment method is recommended to be applied in the ice habit parameterization.

The new microphysics scheme has shown good performances in the simulations of cloud structures and precipitation patterns with two real-case studies. The ice shape effect on the specific microphysical processes is exhibited to be crucial. Furthermore, the realistic evolution, rational vertical distribution, and retained shape memory of ice crystals simulated with the adaptive habit parameterization were nicely demonstrated. Also, the observed main features of the H-M secondary ice production are well captured by the simulations.

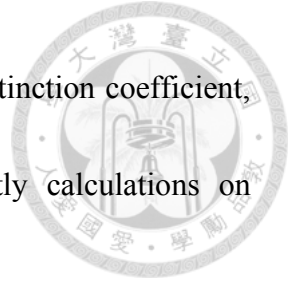
Finally, after the theoretical and observational validations, the bulk adaptive ice habit parameterization in the new microphysics scheme is ready for further applications.

5.2 Future perspective

Some potential research studies separately for model developments and further applications are recommended to advance as follows:

a. Model developments

- 1) Improving some oversimplified ice-related bulk collection efficiencies between different hydrometeor categories through theoretical approaches together with observational constrains if possible.



2) Parameterizing the ice habit on some optical parameters of extinction coefficient, single-scattering albedo, and asymmetry factor for explicitly calculations on radiation fluxes.

3) Increasing prognostic variables of bulk shape and density for the other solid-phase hydrometeors, or separating the ice crystals into two categories of columnar and planar types to track individually.

b. Further applications

1) Implementation of the new multi-moment bulk microphysics scheme to a global model for long-term simulations so as to evaluate the ice shape effect on the radiation budget and large-scale precipitation process.

2) Applying the ice adaptive habit parameterization to an algorithm of remote-sensing observations like satellites and cloud radars since the ice crystal is almost assumed to be spherical in their retrieval hydrometeor products.



References

- Avramov, A., and J. Y. Harrington, 2010: Influence of parameterized ice habit on simulated mixed phase Arctic clouds, *J. Geophys. Res.*, **115**, D03205.
- Baumgardner, D., H. Jonsson, W. Dawson, D. O'Connor, and R. Newton, 2001: The cloud, aerosol and precipitation spectrometer: a new instrument for cloud investigations, *Atmos. Res.*, **59**, 251–264.
- Bailey, M.P., and J. Hallett, 2009: A comprehensive habit diagram for atmospheric ice crystals: confirmation from the laboratory, AIRS II, and other field studies, *J. Atmos. Sci.*, **66**, 2888–2899.
- Beard, K. V., and H. R. Pruppacher, 1971: A wind tunnel investigation of the rate of evaporation of small water drops falling at terminal velocity in air. *J. Atmos. Sci.*, **28**, 1455–1464.
- Bigg, E. K., 1953: The supercooling of water. *Proc. Phys. Soc. London.*, **B66**, 688–694.
- Byers, H. R., 1965: *Elements of Cloud Physics*. The University of Chicago Press, 191 pp.
- Chen, J.-P., and D. Lamb, 1994a: The theoretical basis for the parameterization of ice crystal habits: Growth by vapor deposition. *J. Atmos. Sci.*, **51**, 1206–1221.
- , and ———, 1994b: Simulation of cloud microphysical and chemical processes using a multi-component framework. Part I: Description of the microphysical model, *J. Atmos. Sci.*, **51**, 2613–2630.
- , and S.-T. Liu, 2004: Physically-based two-moment bulk-water parameterization for warm cloud microphysics, *Q. J. Royal Meteor. Soc.*, **130**, 51–78.
- , A. Hazra, and Z. Levin, 2008: Parameterizing ice nucleation rates using contact angle and activation energy derived from laboratory data. *Atmos. Chem. Phys.*, **8**, 7431–7449.
- , I.-C. Tsai, and Y.-C. Lin, 2013: A statistical-numerical aerosol parameterization scheme. *Atmos. Chem. Phys.*, **13**, 10483–10504.
- Cheng, C.-T., W.-C. Wang, and J.-P. Chen, 2007: A modeling study of aerosol impacts on cloud microphysics and radiative properties. *Q. J. R. Meteorol. Soc.*, **133**, 283–297.
- , ———, and ———, 2010: Simulation of the effects of increasing cloud condensation nuclei on mixed-phase clouds and precipitation of a front system, *Atmos. Res.*, **96**, 461–476.
- Chou, M. D., and Suarez, M. J., 1999: A solar radiation parameterization for atmospheric studies. *NASA Tech. Memo*, 104606, 40.

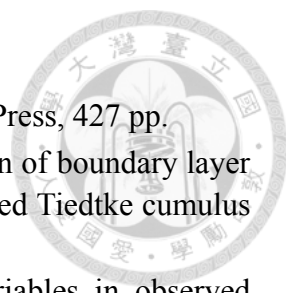
- 
- , K.-T. Lee, and P. Yang, 2002: Parameterization of shortwave cloud optical properties for a mixture of ice particle habits for use in atmospheric models, *J. Geophys. Res.*, **107**, 4600.
- Clark, T.L., 1974: A study in cloud phase parameterization using the gamma distribution. *J. Atmos. Sci.*, **31**, 142–155.
- Cober, S. G., and R. List, 1993: Measurements of the heat and mass transfer parameters characterizing conical graupel growth. *J. Atmos. Sci.*, **50**, 1591–1609.
- Cooper, W. A., 1986: Ice initiation in natural clouds. *Precipitation Enhancement—A Scientific Challenge, Meteor. Mongr.*, **43**, Amer. Meteor. Soc., 29–32.
- Cotton, W. R., et al. 1982: “The Colorado State University three-dimensional cloud/mesoscale model-1982. Part II: An ice phase parameterization.” *J. Rech. Atmos.*, **16.4**, 295–320.
- , G. J. Tripoli, R. M. Rauber, and E. A. Mulvihill, 1986: Numerical simulation of the effects of varying ice crystal nucleation rates and aggregation processes on orographic snowfall. *J. Climate Appl. Meteor.*, **25**, 1658–1680.
- Dearden, C., P. J. Connolly, G. Lloyd, J. Crosier, K. N. Bower, T. W. Choullarton, and G. Vaughan, 2014: Diabatic heating and cooling rates derived from *in-situ* microphysics measurements: A case study of a wintertime UK cold front. *Mon. Wea. Rev.*, in press.
- DeMott, P. J., M. P. Meyers, and W. R. Cotton, 1994: Parameterization and impact of ice initiation processes relevant to numerical model simulations of cirrus clouds. *J. Atmos. Sci.*, **51**, 77–90.
- , A. J. Prenni, X. Liu, S. M. Kreidenweis, M. D. Petters, C. H. Twohy, M.S. Richardson, T. Eidhammer, and D. C. Rogers, 2010: Predicting global atmospheric ice nuclei distributions and their impacts on climate. *Proceedings of the National Academy of Sciences*, **107**, 11217–11222.
- Ferrier, B. S., W. K. Tao, and J. Simpson, 1995: A double-moment multiple-phase four-class bulk ice scheme. Part II: Simulations of convective storms in different large-scale environments and comparisons with other bulk parameterizations. *J. Atmos. Sci.*, **52**, 1001–1033.
- Field, P. R., M'ohler, O., Connolly, P., Kramer, M., Cotton, R., Heymsfield, A. J., Saathoff, H., and Schnaiter, M., 2006: Some ice nucleation characteristics of Asian and Saharan desert dust, *Atmos. Chem. Phys.*, **6**, 2991–3006.
- Fletcher, N. H., 1962: *Physics of Rain Clouds*, Cambridge University Press, 386 pp.
- Hall, W. D., and H. R. Pruppacher, 1976: The survival of ice particles falling from cirrus clouds in subsaturated air. *J. Atmos. Sci.*, **33**, 1995–2006.
- Hallett, J., and B. Mason, 1958: The influence of temperature and supersaturation on the habit of ice crystals grown from the vapor. *Proc. Roy. Soc. London*, **247A**, 440–453.
- , and S. C. Mossop, 1974: Production of secondary ice particles during the riming process. *Nature*, **249**, 26–28.
- Hashino, T., and G. J. Tripoli, 2007: The spectral ice habit prediction system (SHIPS).

- Part I: Model description and simulation of the vapor deposition process. *J. Atmos. Sci.*, **64**, 2210–2237.
- Harrington, J. Y., M. P. Meyers, R. L. Walko, and W. R. Cotton, 1995: Parameterization of ice crystal conversion processes due to vapor deposition for mesoscale models using double moment basis functions. Part I: Basic formulation and parcel model results. *J. Atmos. Sci.*, **52**, 4344–4366.
- , J. Y., K. Sulia, and H. Morrison, 2013a: A method for adaptive habit prediction in bulk microphysical models. Part I: Theoretical development. *J. Atmos. Sci.*, **70**, 349–364.
- , ———, and ———, 2013b: A method for adaptive habit prediction in bulk microphysical models. Part II: Parcel Model Corroboration. *J. Atmos. Sci.*, **70**, 365–376.
- Heymsfield, A. J., and R. G. Knollenberg, 1972: Properties of cirrus generating cells. *J. Atmos. Sci.*, **29**, 1358–1366.
- , and L. J. Donner, 1990: A scheme for parameterizing ice cloud water content in general circulation models. *J. Atmos. Sci.*, **47**, 1865–1877.
- , A. Bansemer, and C. Twohy, 2007: Refinements to ice particle mass dimensional and terminal velocity relationships for ice clouds: Part I: Temperature dependence. *J. Atmos. Sci.*, **64**, 1047–1067.
- Hong, S.-Y., J. Dudhia, and S.-H. Chen, 2004: A revised approach to ice microphysical processes for the bulk parameterization of clouds and precipitation. *Mon. Wea. Rev.*, **132**, 103–120.
- , Y. Noh, and J. Dudhia, 2006: A new vertical diffusion package with an explicit treatment of entrainment processes. *Mon. Wea. Rev.*, **134**, 2318–2341.
- , and J.-O. J. Lim, 2006: The WRF single-moment 6-class microphysics scheme (WSM6). *J. Korean Meteor. Soc.*, **42**, 129–151.
- Hoose, C., J. E. Kristjánsson, J.-P. Chen and A. Hazra, 2010: A classical-theory-based parameterization of heterogeneous ice nucleation by mineral dust, soot, and biological particles in a global climate model, *J. Atmos. Sci.*, **67**, 2483–2503.
- Huffman, P. J., 1973: Supersaturation spectra of AgI and natural ice nuclei. *J. Appl. Meteorol.*, **12**, 1080–1082.
- Iguchi, T., T. Matsui, J. J. Shi, W.-K. Tao, A. P. Khain, A. Hou, R. Cifelli, A. Heymsfield, and A. Tokay, 2012: Numerical analysis using WRF-SBM for the cloud microphysical structures in the C3VP field campaign: Impacts of supercooled droplets and resultant riming on snow microphysics, *J. Geophys. Res.*, **117**, D23206, doi:10.1029/2012JD018101.
- Jakob, C., 2002: *Ice clouds in numerical weather prediction models—Progress, problems and prospects*. Cirrus, D. Lynch et al., Eds, Oxford University Press, 327–345.
- Jayaweera, K. O. L. F., and T. Ohtake, 1974: Properties of columnar ice crystals precipitating front layer clouds. *J. Atmos. Sci.*, **31**, 280–286.
- Ji, W., and P.-K. Wang, 1999: Ventilation coefficients of falling ice crystals at

- low-intermediate Reynolds numbers. *J. Atmos. Sci.*, **56**, 829–836.
- Kain, John S., 2004: The Kain–Fritsch convective parameterization: An update. *J. Appl. Meteor.*, **43**, 170–181.
- Kessler, E., 1969: On the distribution and continuity of water substance in atmospheric circulations. *Meteor. Monogr.*, **10**, Amer. Meteor. Soc. Boston, USA.
- Khvorostyanov, V. I., 1995: Mesoscale processes of cloud formation, cloud-radiation and their modeling with explicit microphysics. *Atmos. Res.*, **39**, 1–67.
- , J. A. Curry, J. O. Pinto, M. Shupe, B. A. Baker, and K. Sassen, 2001: Modeling with explicit spectral water and ice microphysics of a two-layer cloud system of altostratus and cirrus observed during the FIRE Arctic Clouds Experiment. *J. Geophys. Res.*, **106**, 15 099–15 112.
- , V. I., and J. A. Curry, 2002: Terminal velocities of droplets and crystals: Power laws with continuous parameters over the size spectrum. *J. Atmos. Sci.*, **59**, 1872–1884.
- Kinne, S., and K. N. Liou, 1989: The effects of the nonsphericity and size distribution of ice crystals on the radiative properties of cirrus clouds. *Atmos. Res.*, **24**, 273–284.
- Kobayashi, T., 1961: The growth of snow crystals at low supersaturation. *Philos. Mag.*, **6**, 1363–1370.
- Lance, S., C.A. Brock, D. Rogers, J.A. Gordon, 2010: Water droplet calibration of the Cloud Droplet Probe (CDP) and in-flight performance in liquid, ice and mixed-phase clouds during ARCPAC, *Atmos. Meas. Tech.*, **3**, 1683–1706, DOI: 10.5194/amt-3-1683-2010.
- Lawson, R.P., D. O’Connor, P. Zmarzly, L. Weaver, B. Baker, Q. Mo, H. Jonsson, 2006: The 2D-S (Stereo) probe: design and preliminary tests of a new airborne, high-speed, high-resolution particle imaging probe, *J. Atmos. Oceanic Technol.*, **23**, 1462–1477, DOI: 10.1175/JTECH1927.1.
- Lim, K.-S. S., and S.-Y. Hong, 2010: Development of an effective double-moment cloud microphysics scheme with prognostic cloud condensation nuclei (CCN) for weather and climate models. *Mon. Wea. Rev.*, **138**, 1587–1612.
- Lin, Y. L., R. Farley, and H. D. Orville, 1983: Bulk parameterization of the snow field in a cloud model. *J. Climate Appl. Meteor.*, **22**, 1065–1092.
- Lin, Y. L., and B. A. Colle, 2011: A new bulk microphysical scheme that includes riming intensity and temperature-dependent ice characteristics. *Mon. Wea. Rev.*, **139**, 1013–1035.
- Locatelli, J. D., and P. V. Hobbs, 1974: Fall speeds and masses of solid precipitation particles. *J. Geophys. Res.*, **79**, 2185–2197.
- Mansell, E. R., C. L. Ziegler, and E. C. Bruning, 2010: Simulated electrification of a small thunderstorm with two-moment bulk microphysics. *J. Atmos. Sci.*, **67**, 171–194.
- McFarquhar, G. M., J. Heymsfield, J. Spinhirne, and B. Hart, 2000: Thin and subvisual tropopause tropical cirrus: Observations and radiative impacts. *J. Atmos. Sci.*, **57**,

- 1841–1853.
- Meyers, M. P., DeMott, P. J., and Cotton, W. R., 1992: New primary ice nucleation parameterizations in an explicit cloud model, *J. Appl. Meteorol.*, **31**, 708–721.
- Milbrandt, J. A., and M. K. Yau, 2005a: A multimoment bulk microphysics parameterization. Part I: analysis of the role of the spectral shape parameter. *J. Atmos. Sci.*, **62**, 3051–3064.
- , and ———, 2005b: A multimoment bulk microphysics parameterization. Part II: A proposed three moment closure and scheme description. *J. Atmos. Sci.*, **62**, 3065–3081.
- , and H. Morrison, 2013: Prediction of Graupel Density in a Bulk Microphysics Scheme. *J. Atmos. Sci.*, **70**, 410–429.
- Mitchell, D. L., 1996: Use of mass- and area-dimensional power laws for determining precipitation particle terminal velocities. *J. Atmos. Sci.*, **53**, 1710–1723.
- , and A. J. Heymsfield, 2005: The treatment of ice particle terminal velocities, highlighting aggregates. *J. Atmos. Sci.*, **62**, 1637–1644.
- Morrison, H., and J. O. Pinto, 2005: Mesoscale modeling of springtime arctic mixed phase clouds using a new two-moment bulk microphysics scheme. *J. Atmos. Sci.*, **62**, 3683–3704.
- , G. Thompson, V. Tatarskii, 2009: Impact of Cloud Microphysics on the Development of Trailing Stratiform Precipitation in a Simulated Squall Line: Comparison of One- and Two-Moment Schemes. *Mon. Wea. Rev.*, **137**, 991–1007.
- Murakami, M., 1990: Numerical modeling of dynamical and microphysical evolution of an isolated convective cloud—The 19 July 1981 CCOPE cloud. *J. Meteor. Soc. Japan*, **68**, 107–128.
- Nakaya, Ukichiro, 1954: *Snow Crystals: Natural and Artificial*. Harvard University Press. ISBN 978-0-674-81151-5.
- NOAA, cited 2001: National Oceanic and Atmospheric Administration Changes to the NCEP Meso Eta Analysis and Forecast System: Increase in resolution, new cloud microphysics, modified precipitation assimilation, modified 3DVAR analysis. [Available online at <http://www.emc.ncep.noaa.gov/mmb/mmbp11/eta12tpb/>.]
- Passarelli, R. E., 1978: An approximate analytical model of the vapor deposition and aggregation growth of snowflakes. *J. Atmos. Sci.*, **35**, 118–124.
- , and R. C. Srivastava, 1978: A new aspect of snowflake aggregation theory. *J. Atmos. Sci.*, **36**, 484–493.
- Pruppacher, H. R., and J. D. Klett, 1997: *Microphysics of Clouds and Precipitation*, vol. 18, Kluwer Academic Publishers, Dordrecht, the Netherlands.
- Sheridan, L. M., J. Y. Harrington, D. Lamb, and K. Sulia, 2009: Influence of ice crystal aspect ratio on the evolution of ice size spectra during vapor depositional growth, *J. Atmos. Sci.*, **66**, 3732–3743.
- Shi, J. J., and Coauthors, 2010: WRF simulations of the 20–22 January 2007 snow events over eastern Canada: Comparison with in situ and satellite observations, *J. Appl. Meteorol. Climatol.*, **49**, 2246–2266.

- Straka, Jerry M., and Edward R. Mansell., 2005: A bulk microphysics parameterization with multiple ice precipitation categories, *J. Applied Meteorology*, **44.4**, 445–466.
- Rasmussen, R. M., V. Levizzani, and H. R. Pruppacher, 1984: A wind tunnel and theoretical study of the melting behavior of atmospheric ice particles. II: A theoretical study for frozen drops of radius < 500 μm . *J. Atmos. Sci.*, **41**, 374–380.
- , and A. J. Heymsfield, 1985: A generalized form for impact velocities used to determine graupel accretional densities. *J. Atmos. Sci.*, **42**, 2275–2279.
- , and ———, 1987a: Melting and shedding of graupel and hail. Part I: Model physics. *J. Atmos. Sci.*, **44**, 2754–2763.
- , and ———, 1987b: Melting and shedding of graupel and hail. Part II: Sensitivity study. *J. Atmos. Sci.*, **44**, 2764–2782.
- Rutledge, S. A., and P. V. Hobbs, 1984: The mesoscale and microscale structure and organization of clouds and precipitation in mid-latitude clouds. Part XII: A diagnostic modeling study of precipitation development in narrow cold frontal rainbands, *J. Atmos. Sci.*, **41**, 2949–2972.
- Takano, Y., and K. N. Liou, 1989: Solar radiative transfer in cirrus clouds. Part I. Single-scattering and optical properties of hexagonal ice crystals. *J. Atmos. Sci.*, **46**, 3–19.
- Tao, W.-K., J. Simpson, M. McCumber, 1989: An Ice–Water Saturation Adjustment. *Mon. Wea. Rev.*, **117**, 231–235.
- , and J. S. Simpson, 1993: Goddard cumulus ensemble model. Part I: Model description. *Terr. Atmos. Ocean. Sci.*, **4**, 35–72.
- , J.-P. Chen, Z.-Q. Li, C. Wang and C.-D. Zhang, 2012: The impact of aerosol on convective cloud and precipitation. *Rev. Geophys.*, **50**, RG2001, doi:10.1029/2011RG000369.
- Thompson, G., P. R. Field, R. M. Rasmussen, and W. D. Hall, 2008: Explicit forecasts of winter precipitation using an improved bulk microphysics scheme. Part II: Implementation of a new snow parameterization. *Mon. Wea. Rev.*, **136**, 5095–5115.
- Tiedtke, M., 1989: A comprehensive mass flux scheme for cumulus parameterization in large-scale models. *Mon. Wea. Rev.*, **117**, 1779–1800.
- Wang, P. K., and W. Ji, 2000: Collision efficiencies of ice crystals at low–intermediate Reynolds numbers colliding with supercooled cloud droplets: A numerical study. *J. Atmos. Sci.*, **57**, 1001–1009.
- Whitby, K. T., 1978: The physical characteristics of sulfur aerosols. *Atmos. Environ.*, **12**, 135–159.
- Yang, P., and Q. Fu, 2009: Dependence of ice crystal optical properties on particle aspect ratio. *JQSRT*, **72**, 403–17.
- Yankofsky, S. A., Levin, Z., Bertold, T., and Sandlerman, N., 1981: Some basic characteristics of bacterial freezing nuclei, *J. Appl. Meteorol.*, **20**, 1013–1019.
- Young, K. C., 1974: The role of contact nucleation in ice phase initiation in clouds. *J.*

- 
- Atmos. Sci.*, **31**, 1735–1748.
- , 1993: *Microphysical Processes in Clouds*. Oxford University Press, 427 pp.
- Zhang, C., Y. Wang, and K. Hamilton, 2011: Improved representation of boundary layer clouds over the southeast pacific in ARW–WRF using a modified Tiedtke cumulus parameterization scheme. *Mon. Wea. Rev.*, **139**, 3489–3513.
- Ziegler, C. L., 1985: Retrieval of thermal and microphysical variables in observed convective storms. Part 1: Model development and preliminary testing. *J. Atmos. Sci.*, **42**, 1487–1509.



Tables

Table 1 The prognostic variables in terms to the current microphysics schemes in the WRF model for version 3.4.1, where Q , N , and V represents mixing ratio, number concentration, and volume whereas v , c , r , i , s , g , h , and ccn are denoted water vapor, cloud, rain, ice, snow, graupel, hail and cloud condensation nuclei, respectively.

Scheme	Mass	Number	Other	Reference
Kessler	Qv, Qc, Qr	x	x	Kessler (1969)
Purdue Lin	Qv, Qc, Qr, Qi, Qs, Qg	x	x	Lin et al. (1983)
WSM3	Qv, Qc, Qr	x	x	Hong et al. (2004)
WSM5	Qv, Qc, Qr, Qi, Qs	x	x	
Eta_MP	Qv, Qc, Qr, Qs, Qt	x	x	NOAA (2001)
WSM6	Qv, Qc, Qr, Qi, Qs, Qg	x	x	Hong and Lim (2006)
Goddard	$Qv, Qc, Qr, Qi, Qs, Qg(Qh)$	x	x	Tao et al. (1989)
Thompson	Qv, Qc, Qr, Qi, Qs, Qg	Ni, Nr	x	Thompson et al. (2008)
Milbrandt	$Qv, Qc, Qr, Qi, Qs, Qg, Qh$	Nc, Nr, Ni, Ns, Ng, Nh	x	Milbrandt and Yau (2005)
Morrison	$Qv, Qc, Qr, Qi, Qs, Qg(Qh)$	Nr, Ni, Ns, Ng	x	Morrison et al. (2009)
SBU Lin	Qv, Qc, Qr, Qi, Qs	x	$rimi^*$	Lin and Colle (2011)
WDM5	Qv, Qc, Qr, Qi, Qs	Nc, Nr	$Nccn$	Lim and Hong (2010)
WDM6	Qv, Qc, Qr, Qi, Qs, Qg	Nc, Nr	$Nccn$	
NSSL	$Qv, Qc, Qr, Qi, Qs, Qg, Qh$	Nc, Nr, Ni, Ns, Ng, Nh	$Nccn, Vg$	Mansell et al. (2010)

*: indicated ice riming intensity.

Table 2 The lists of ice shape and volume moments used in the new microphysics scheme.

Microphysical process	Shape moment	Volume moment
ice homo/hetero-geneous nucleation	isometric ($D_0 = 6 \mu\text{m}$)	$\rho_{i,0} = 910 \text{ kg m}^{-3}$
ice multiplication		
melting	none	
aggregation; initiation of large ice crystal	keep the memories of ϕ_i and ρ_i	
accretion by other particles		
deposition/sublimation growth	with forcing (2.20)	$\rho_{i,dep}$ (2.19)
riming growth	with forcing (2.30), (2.35)	$\rho_{i,rim}$ (2.33)

Table 3 The coefficients used for the spectral index (α_x), the mass-dimensional relationship (a_{mx} , b_{mx}), bulk density (ρ_x), terminal velocity-dimensional relationship (a_{vx} , b_{vx}) for all hydrometeor categories.

Category	α_x	a_m	b_m	ρ_x	a_v	b_v
Cloud	0	$\pi\rho_w/6$	3	997	3.E7	2
Rain	0				841.997	0.8
Pristine Ice	0~30	variable	1.6~3	100~910	variable	
Aggregate	0	$\pi\rho_s/6$	3	100~910	11.72	0.4
Graupel	0	$\pi\rho_g/6$		400	19.3	0.37
Hail	0	$\pi\rho_h/6$		900	206.89	0.6384

Table 4 All collection efficiencies E utilized in the new microphysics scheme. The left two columns represent interacting hydrometeor categories, where T_c is air temperature in C degree, D is the mean volume diameter, ρ_x is the bulk density, and $STOKE$ is the stoke number.

Hydrometeors		Collection Efficiencies	Reference
Cloud	Ice	$E_{ci} = f(Re_i, D_c)$	Wang and Ji (2000)
	Snow	$E_{cs} = D_c^{33333} * (1000 * D_s)^{0.5}$	Pruppacher and Klett (1997)
	Graupel	$E_{cg} = 0.55 * \log_{10}^{2.51 * STOKE}$	Cober and List (1993)
	Hail	$E_{ch} = e^{-8.68E-7 * D_c - 1.6 * D_h}$	Ziegler (1985)
Rain	Ice	$E_{ri} = 1$	Milbrandt and Yau (2005b)
	Snow	$E_{rs} = 1$	Milbrandt and Yau (2005b)
	Graupel	$E_{rg} = 0.55 * \log_{10}^{2.51 * STOKE}$	Cober and List (1993)
	Hail	$E_{rh} = 1$	Milbrandt and Yau (2005b)
Ice	Ice	$E_{ii} = \max(1 - \rho_i / \rho_{i0}, 10^{0.035T_c - 0.7})$	Chen and Lamb (1994b); Cotton et al. (1982)
	Snow	$E_{is} = 0.05e^{0.1T_c}$	Ferrier et al. (1995)
	Graupel	$E_{ig} = 0.01e^{0.1T_c}$	
	Hail	$*E_{ih} = 0.01e^{0.1T_c}$	
Snow	Snow	$E_{ss} = \max(1 - \rho_s / \rho_{s0}, 0.005e^{0.1T_c})$	Chen and Lamb (1994b); Ferrier et al. (1995)
	Hail	$*E_{sh} = 0.01e^{0.1T_c}$	Ferrier et al. (1995)

*: The values of E_{ih} and E_{sh} are switched to unity in hailstone wet-growth mode.

Table 5 All notations BMP_{xy} (or BMP_{xyz}) utilized in the new microphysics scheme, where B for the prognostic variable, MP for the microphysical process, and xyz for the hydrometeor category.

Symbol	Character	Definition	Character	Definition
B	Q	mass mixing ratio	N	number concentration
	F	shape moment	V	volume moment
xyz	v	water vapor	a	condensation nuclei or hygroscopic aerosol
	c	cloud droplet	r	raindrop
	i	pristine ice crystal	s	snow-aggregate
	g	graupel (rimmed ice)	h	hailstone
Symbol	Character	Definition		
MP	AC	activation/deactivation		
	BK	breakup of raindrops to cloud/raindrops		
	CL	collection without phase change, including self-collection		
	CN	auto-conversion processes		
	EV	evaporation loss		
	FZ	freezing, including homogeneous, contact, and immersion freezing		
	HO	homogeneous freezing of cloud drops or raindrops		
	IM	ice multiplication via snow riming and graupel riming splintering		
	IN	initiation of graupel from heavily rimed ice or snow		
	ML	melting of frozen particles		
	NC	contact freezing of cloud drops or raindrops		
	ND	ice deposition/condensation nucleation		
	NM	immersion freezing of cloud drops or raindrops		
	RM	riming processes (collection particles across liquid and ice phase)		
	SB	sublimation loss		
	SH	shedding of raindrops during hailstone wet growth		
VD	vapor diffusion growth			

Table 6 Coefficients of the formulas adopted from Chen and Liu (2004).

Item	<i>a</i>	<i>b</i>	<i>c</i>	<i>d</i>	Equ. ID
Q1	6.6793E+0	1.0090E+0	1.4095E+0	-	2.80a
Q2	9.9912E+0	-4.7678E+0	-3.1388E-2	-	2.80b
Q3	2.0090E+1	2.9626E+0	3.2358E+0	-	2.81b
Q4	-2.1370E+1	1.9899E+9	-	-	2.86b
Q5	-2.3531E+1	9.8271E-1	-1.3202E-1	-	2.88b
N1	-1.0593E+0	8.9774E-1	-2.8403E-1	1.6328E+0	2.74a
N2	8.2841E+0	9.7219E-1	-5.0808E-1	-	2.75a
N3	1.5519E+1	3.1491E+0	4.3989E-1	-	2.81a
N4	-4.3561E+0	1.9934E+0	1.6465E-2	-	2.82a
N5	-1.8239E+1	2.2956E+0	-2.3261E-4	-	2.82b
N6	-4.0731E+1	5.3720E+5	-2.0139E-5	-	2.86a
N7	-1.6185E+2	2.2786E+5	-7.6988E+7	-	2.88b
N8	-1.7431E+2	2.6031E+5	-9.3613E+7	-	2.88c

Table 7 Numbers, means, and geometric width of nucleation (Nu), accumulation (Ac), and coarse (Co) modes of three aerosol size distribution types over marine and continent types, including clean, average and urban background.

Parameter	number (m ⁻³)			mean (m)			geometric width			scale
	Nu	Ac	Co	Nu	Ac	Co	Nu	Ac	Co	height (m)
Marine	3.4e8	6.e7	3.e6	5.e-9	3.55e-8	3.1e-7	0.47	0.69	0.99	800
Clean	1.e9	8.e8	7.2e5	8.e-9	3.3e-8	4.6e-7	0.47	0.74	0.79	3570
Average	6.4e9	2.3e9	3.2e6	7.5e-9	3.8e-8	5.1e-7	0.53	0.69	0.77	3570
Urban	1.06e11	3.2e10	5.4e6	7.e-9	2.7e-8	4.3e-7	0.59	0.77	0.79	2000

Table 8 Parameters used for the ice deposition-nucleation mode.

Ice nuclei	assigned aerosol radius	contact angle	activation energy
Species	r_N (μm)	θ_{dep} (degree)	$\Delta g^\#$ (10 ⁻²⁰ J)
Soot	0.04	28.0	-20.0
Saharan dust	0.175	5.06	3.35
Asian dust	0.2	8.1	1.82

Table 9 The model setup for the new multi-moment microphysics and GSFC radiation schemes with respect to three simulations of Sphere-2M, Shape-2M, and Shape-3M. Circle was represented for available whereas cross was not.

Scheme	MP/RA setup	Sphere-2M	Shape-2M	Shape-3M
Microphysics (new multi-moment)	Crystal shape	spherical	non-spherical	non-spherical
	Apparent density	×	○	○
	Ventilation effect	○	○	○
	Closure method of spectrum function	2-moment ($\alpha_i = 3$)	2-moment ($\alpha_i = 3$)	3-moment (α_i is prognostic)
Radiation (GSFC)	Coupling of ice effective radius	○	○	○
	Orientation effect	×	○	○

Table 10 The WRF model setup and physics options used for the C3VP case.

Initial/Boundary Condition		Physics options	
NCEP FNL reanalysis data		Cumulus	Tiedtke scheme
Domain setup		PBL	YSU scheme
Domain 1	90 x 75 (20 km)	SW Radiation	GSFC scheme
Domain 2	141 x 141 (4 km)	LW radiation	
Domain 3	154 x 154 (1.33 km)	Surface layer	Monin-Obukhov
Vertical layer	50	Surface	Thermal diffusion

Table 11 The WRF model setup and physics options used for the DIAMET case.

Initial/Boundary Condition		Physics options	
ECMWF reanalysis data		Cumulus	Kain-Fritsch scheme
Domain setup		PBL	YSU scheme
Domain 1	110 x 75 (30 km)	SW Radiation	GSFC scheme
Domain 2	231 x 176 (6 km)	LW radiation	
Domain 3	301 x 250 (2 km)	Surface layer	Monin-Obukhov
Vertical layer	50	Surface	Thermal diffusion

Figures

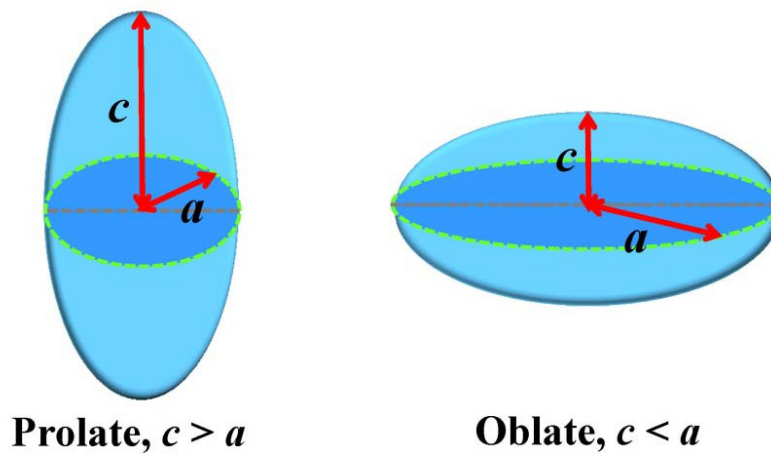


Figure 1.1 Perspective views of prolate and oblate spheroids that resemble columnar and planar ice crystals, respectively.

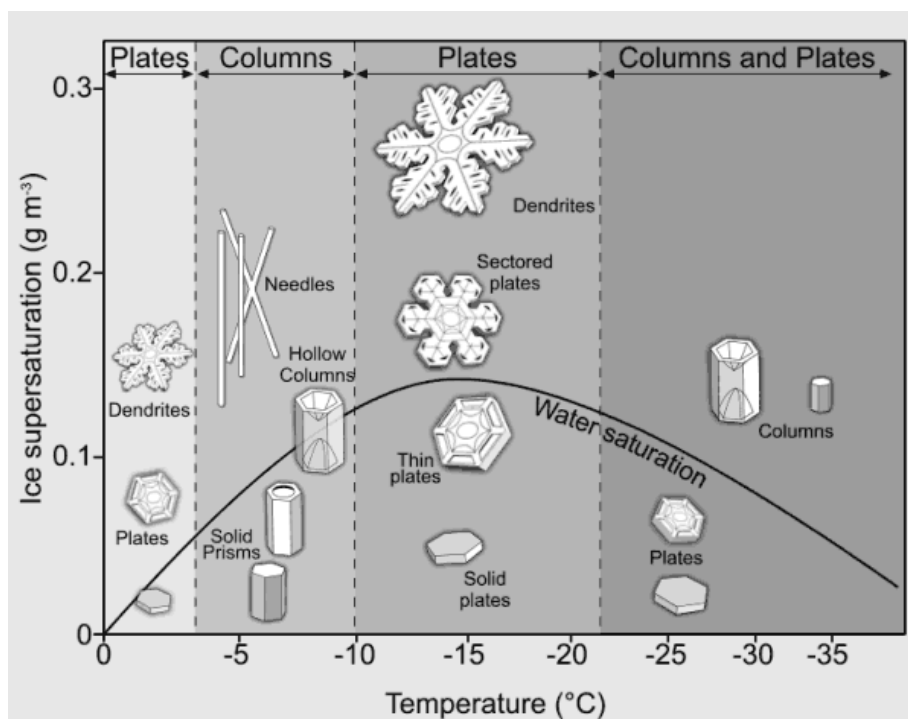


Figure 1.2 The illustration of ice crystal habit diagram as a function of both temperature and ice supersaturation. (Download from the website of www.cas.manchester.ac.uk).

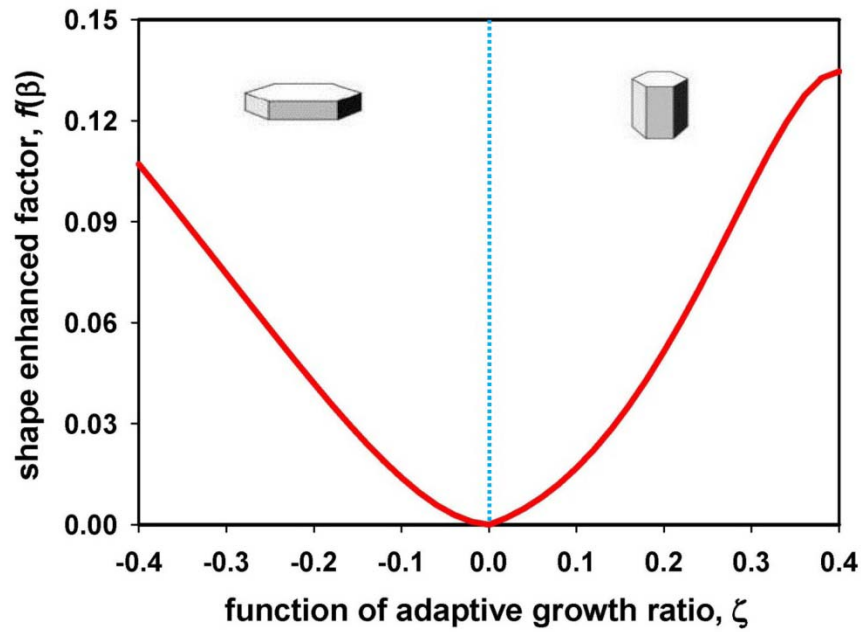


Figure 2.1 The ice shape enhanced factor (y-axis) with respect to the adaptive growth ratio (x-axis, $\zeta < 0$ for oblate while $\zeta > 0$ for prolate).

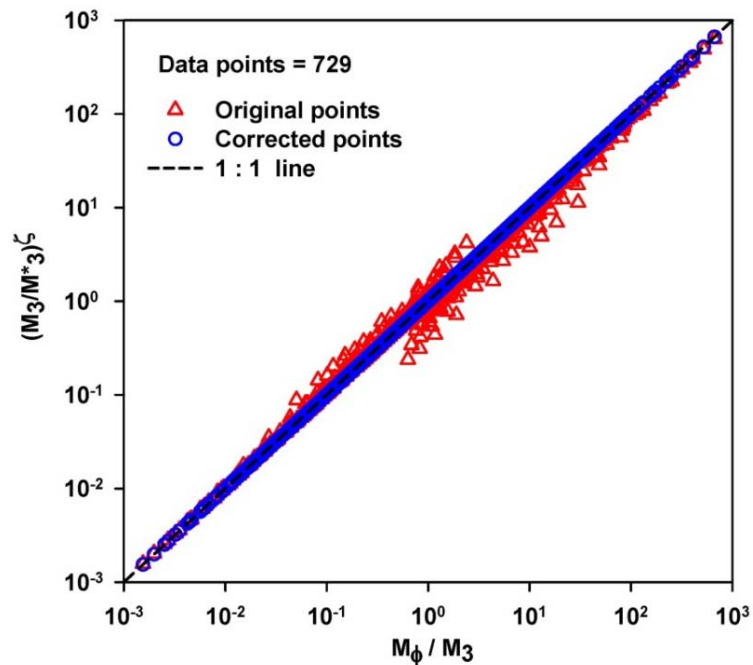


Figure 2.2 The original (in triangle red) and corrected (in circle blue) data points between $\left(\frac{M_3}{M_3^*}\right)^\zeta$ (y-axis) and $\frac{M_\phi}{M_3}$ (x-axis).

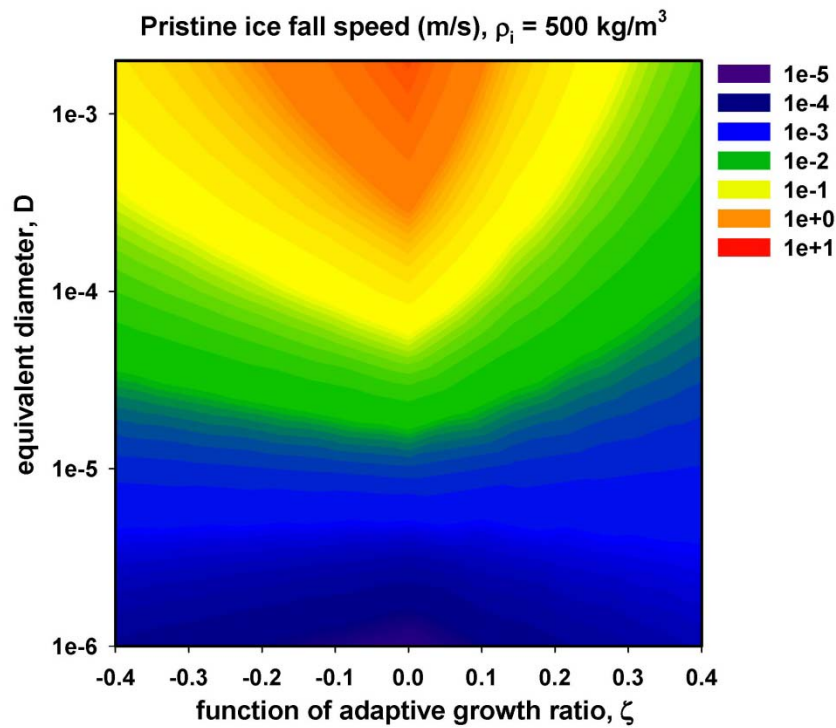
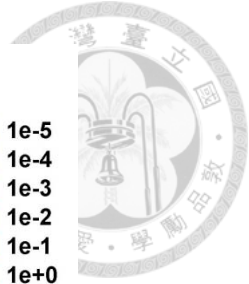


Figure 2.3 The shaded contour of pristine ice fall speed (m/s) in terms of equivalent diameters (y -axis) from $1 \mu\text{m}$ to 2 mm and adaptive growth ratios (x -axis, $\zeta < 0$ for oblate while $\zeta > 0$ for prolate) at a given density of 500 kg m^{-3} .

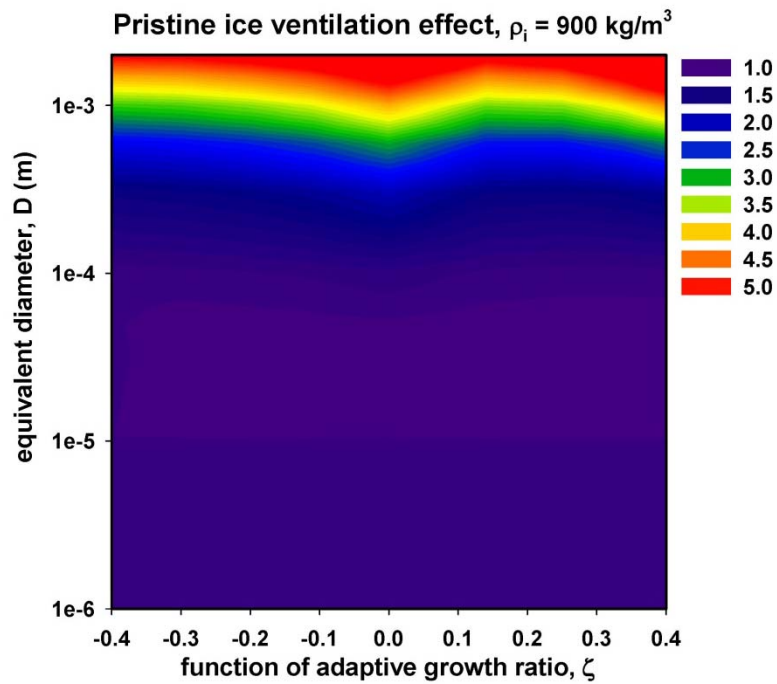
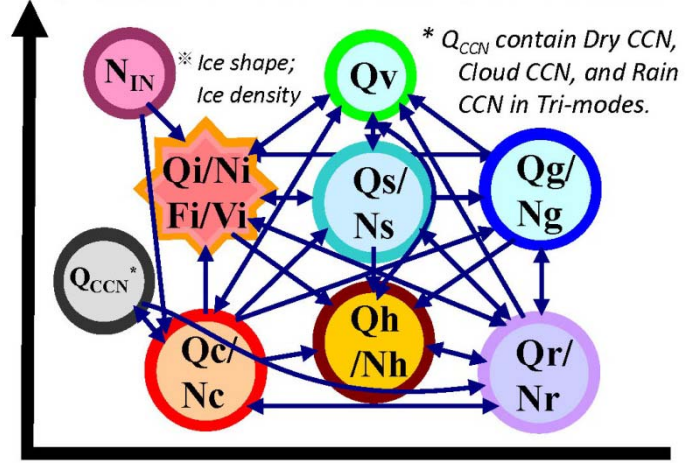


Figure 2.4 The shaded contour of pristine ice ventilation effect in terms of equivalent diameters (y -axis) from $1 \mu\text{m}$ to 2 mm and adaptive growth ratios (x -axis, $\zeta < 0$ for oblate while $\zeta > 0$ for prolate) at a given density of 900 kg m^{-3} .



New Ice-3M scheme



19 Variables

Figure 2.5 The representation of hydrometeor categories predicted in the new microphysics scheme, where Q , N , F , and V represents mixing ratio, number concentration, shape, and volume whereas v , c , r , i , s , g , h , in , and ccn are denoted water vapor, cloud, rain, ice, snow, graupel, hail, ice nuclei, and cloud condensation nuclei, respectively.

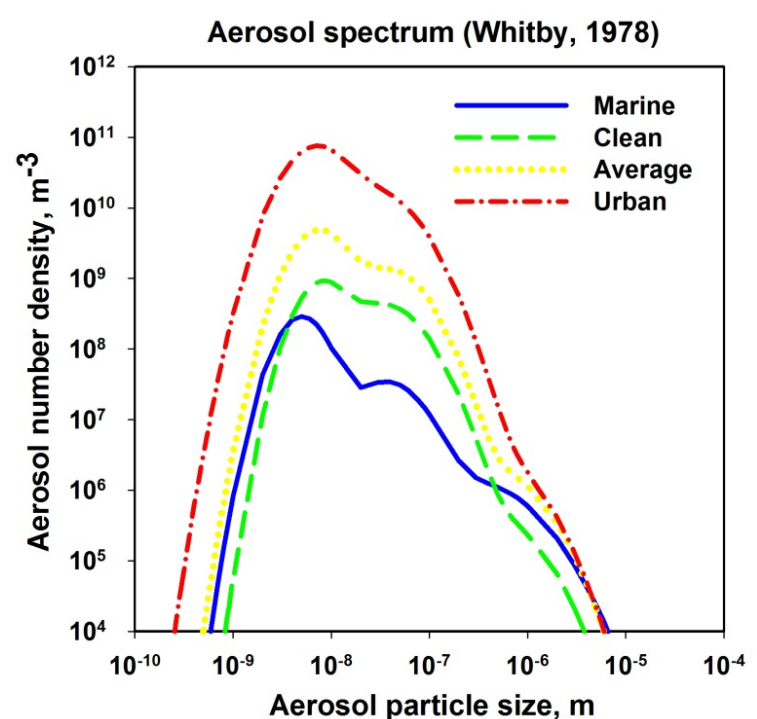


Figure 2.6 The aerosol spectrums of marine (blue), clean (green), average (yellow), and urban (red) type referred to Whitby (1978).

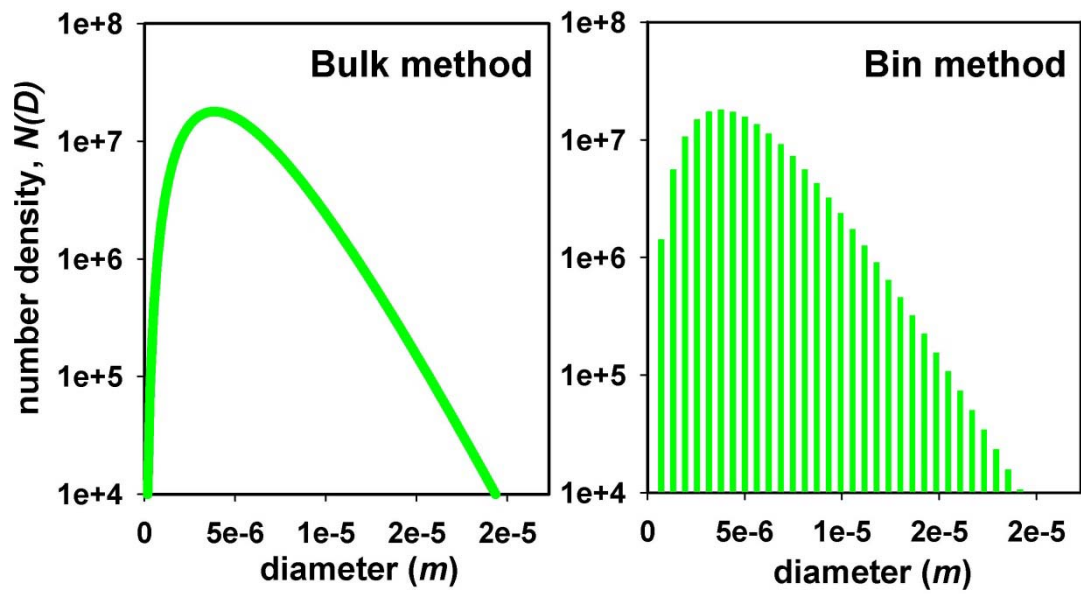


Figure 3.1 The representations of initial spectrum for the bulk (left) and bin (right) methods with the parameters of $\lambda_i = 8 \times 10^5 \text{ m}^{-1}$, $N_i = 100 \text{ m}^{-3}$, and $\alpha_i = 3$.

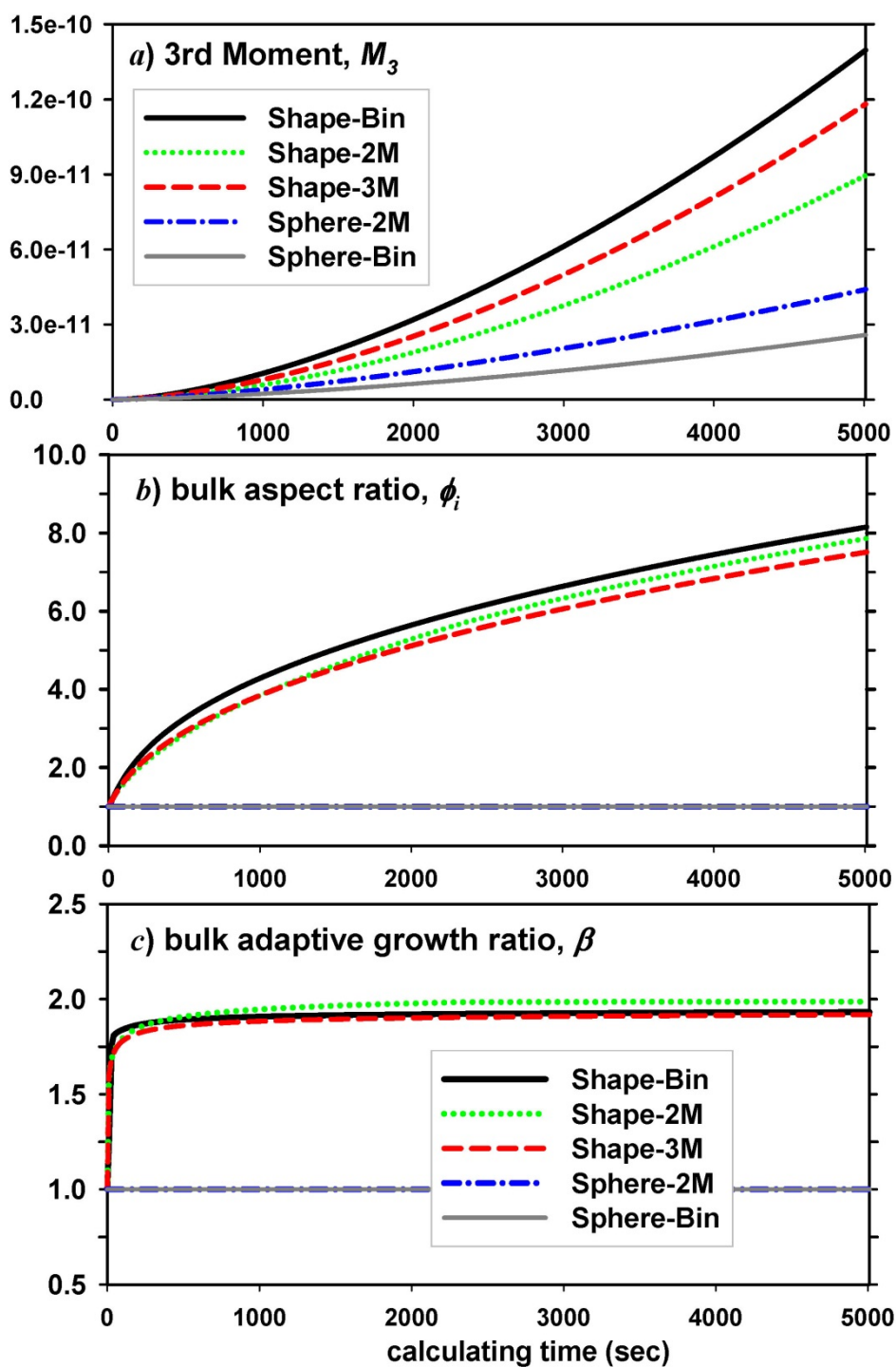
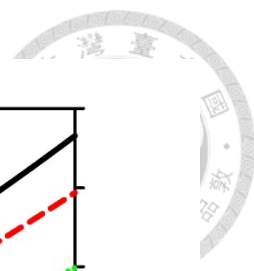


Figure 3.2 The calculation results of (a) the 3rd-moment, (b) the bulk aspect ratio, and (c) the bulk adaptive growth ratio for shape ice with the bin (in solid-black), bulk-2M (in dotted-green), and bulk-3M (in dash-red) methods, as well as for spherical ice with the bin (solid-gray) and bulk-2M methods (in dash-dot-blue). For these calculations, $T = 266\text{K}$, $P = 800\text{ hpa}$, $\Delta Q_{vi} = 10^{-5}\text{ kg kg}^{-1}$, $f_{vi} = 1$, and $\Gamma(T) = 2.0$.

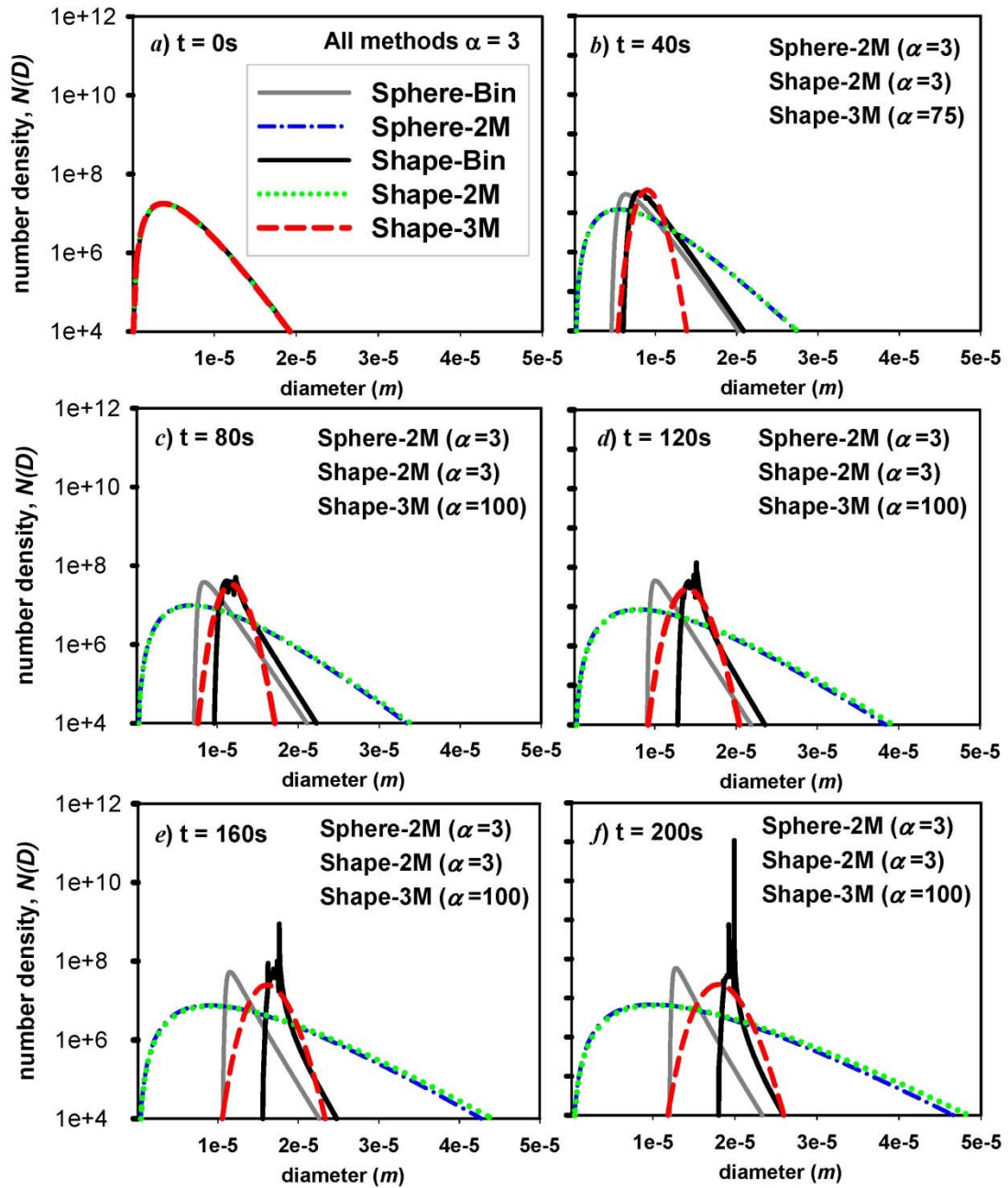


Figure 3.3 The size spectrums of the Shape-bin (in solid-black), Sphere-bin (in solid-gray) Shape-3M (in dash-red), Shape-2M (in dotted-green), and Sphere-2M (in dash-dot-blue) with an indicator of α_i individually at the starting 200 seconds with an interval of 40s depicted from panel (a) to (f).

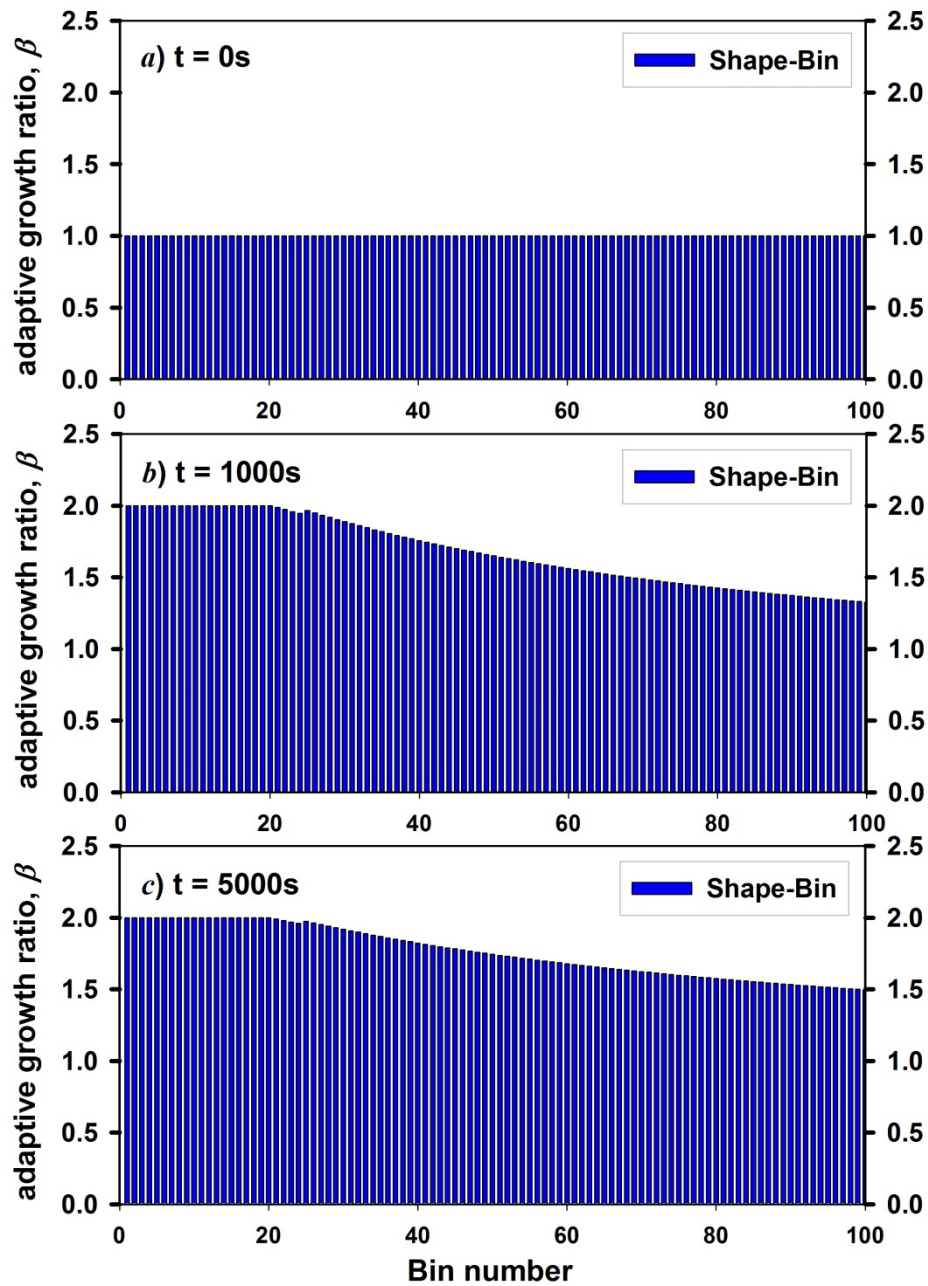
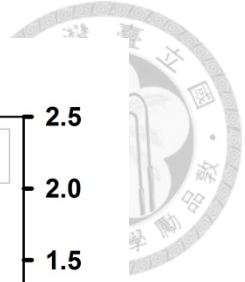


Figure 3.4 The bar chart plots of β in each bin for Shape-bin calculation at the (a) zero, (b) 1000, and (c) 5000 seconds, respectively. The x-axis denoted the number of bin from 1 to 100 and the y-axis was the representation of β .

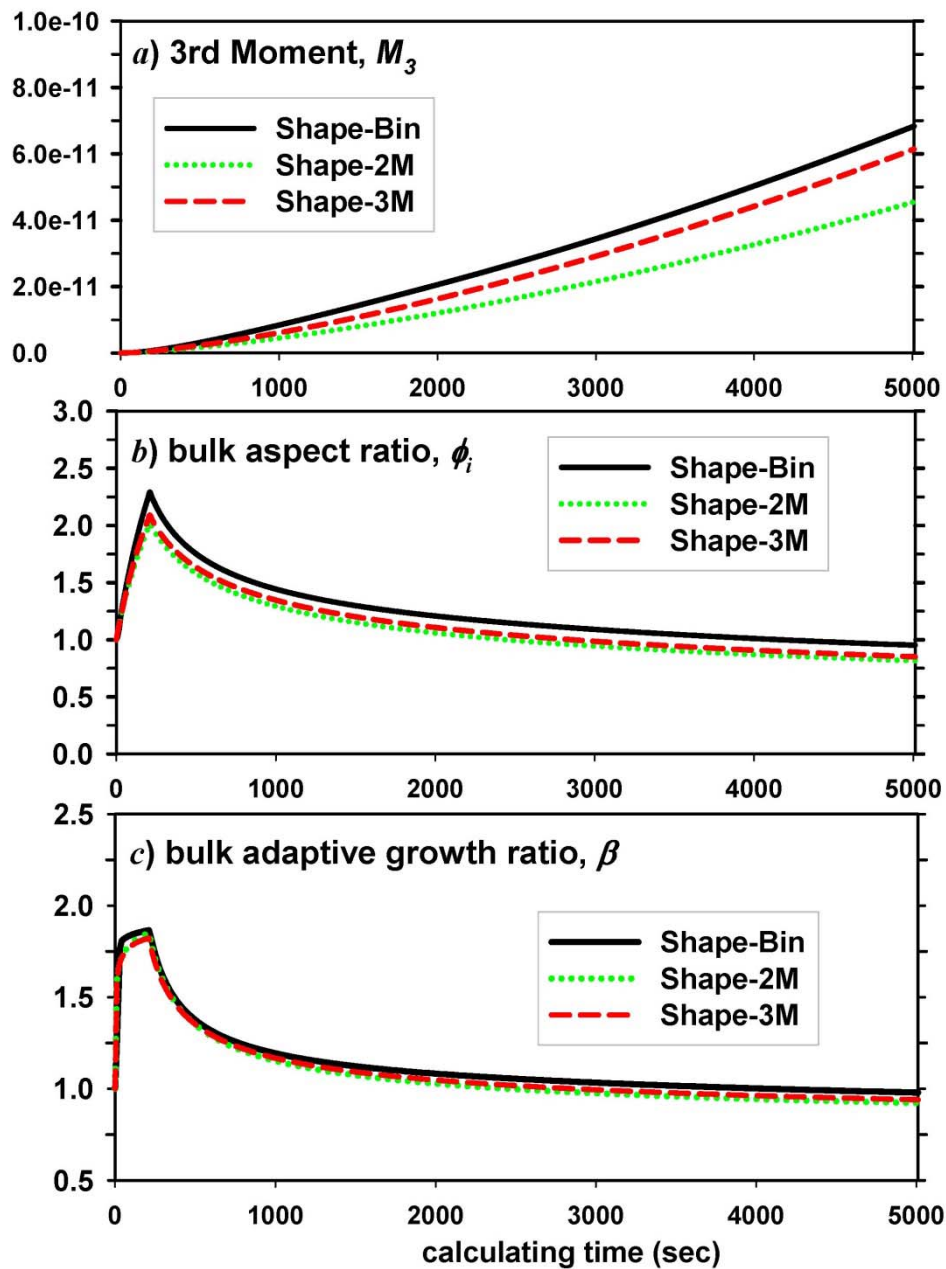
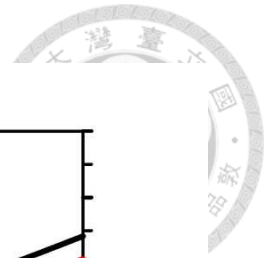


Figure 3.5 The calculation results of (a) the 3rd-moment, (b) the bulk aspect ratio, and (c) the bulk adaptive growth ratio for shape ice with the bin (in solid-black), bulk-2M (in dotted-green), and bulk-3M (in dash-red) methods. For these calculations, the environment was the same to Figure 3.2 except for $\Gamma(T)=0.5$ after 200 seconds.

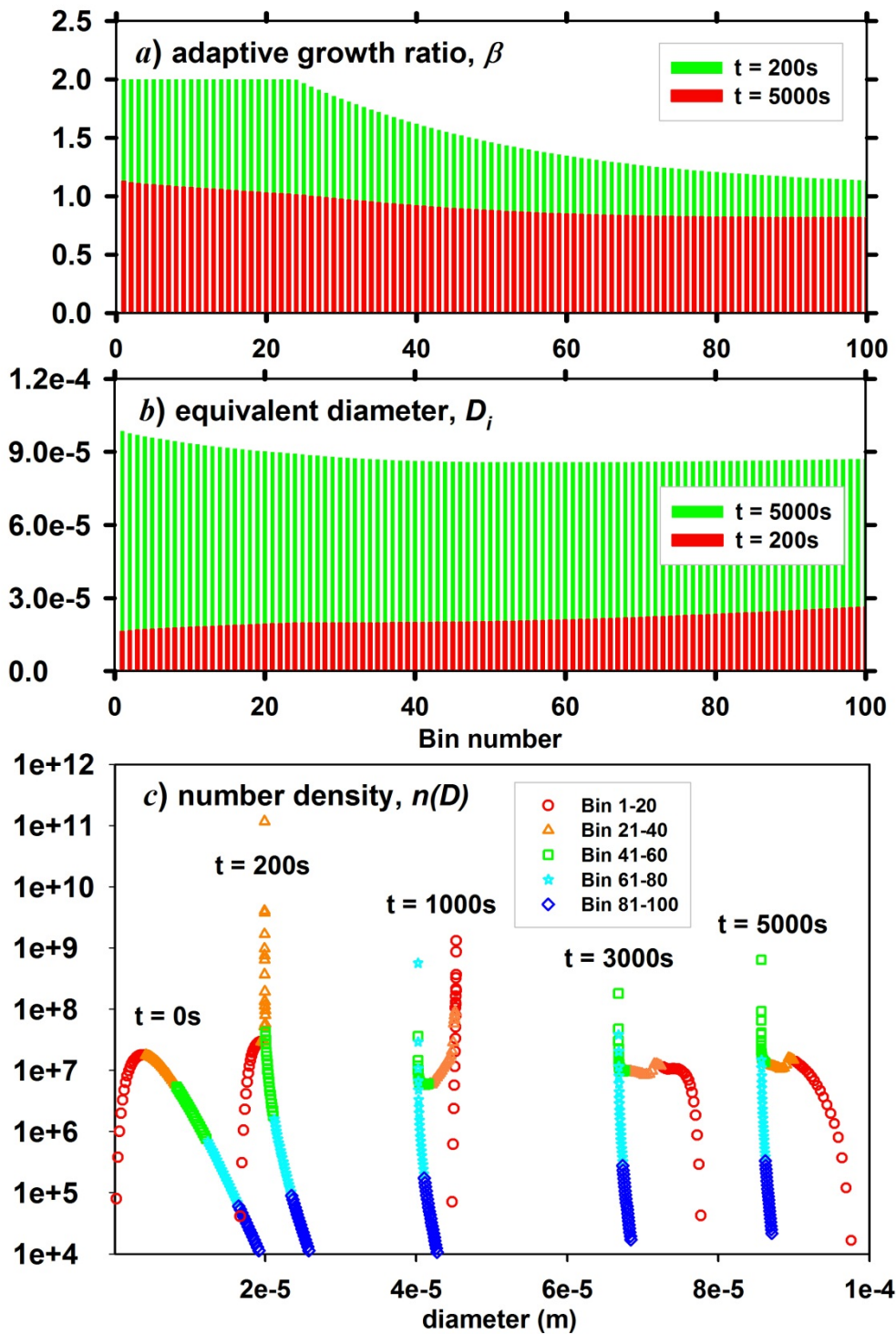
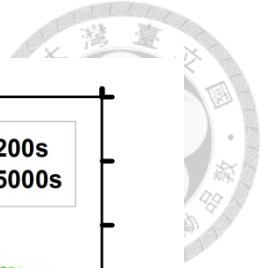


Figure 3.6 The bar chart plots of the Shape-bin's calculation results over (a) the adaptive growth ratio and (b) the equivalent diameter (m) for each bin at the 200 and 5000 seconds. The x -axis was the bin number from 1 to 100. Panel (c) represented the number density for each bin (bin 1-10 in red circle, bin 21-40 in orange triangle, bin 41-60 in green square, bin 61-80 in light blue star, and bin 81-100 in blue diamond) at the 0, 200, 1000, 3000, and 5000 seconds.

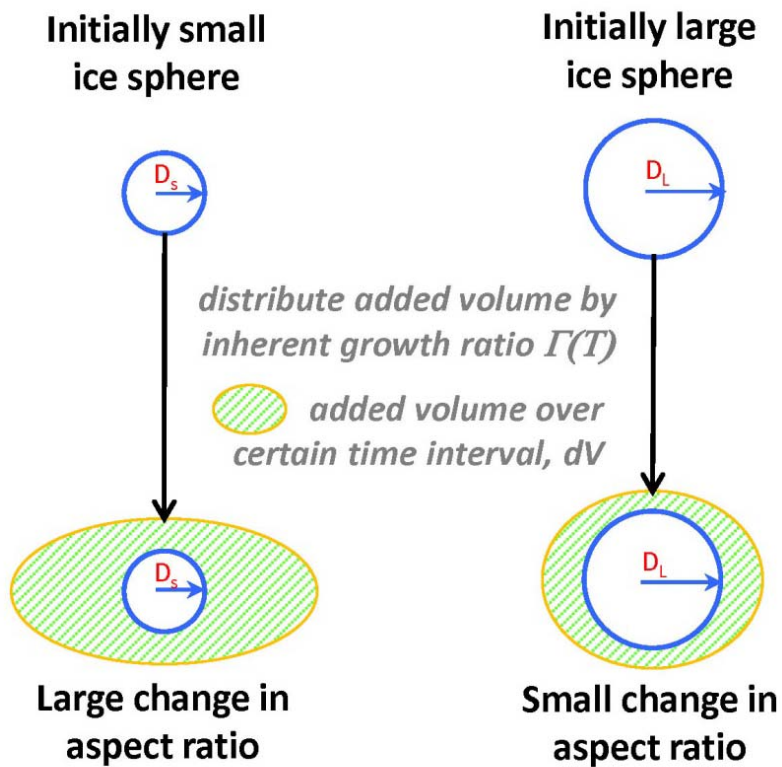


Figure 3.7 The illustration of the aspect ratio increase over certain time steps due to vapor diffusional growth for two ice particles with an initially small sphere (left) and an initially large one (right). While the increase in volume (in shaded green) is bigger for the initially larger particle ($dV_L > dV_S$), the relative increase in volume (dV/V) is larger for the smaller sphere. This new volume is distributed over the a and c axes by inherent growth ratio $\Gamma(T)$, causing a larger increase in aspect ratio for the initially smaller sphere. (This plot was reproduced from the Figure 3. in Sheridan et al. 2009).

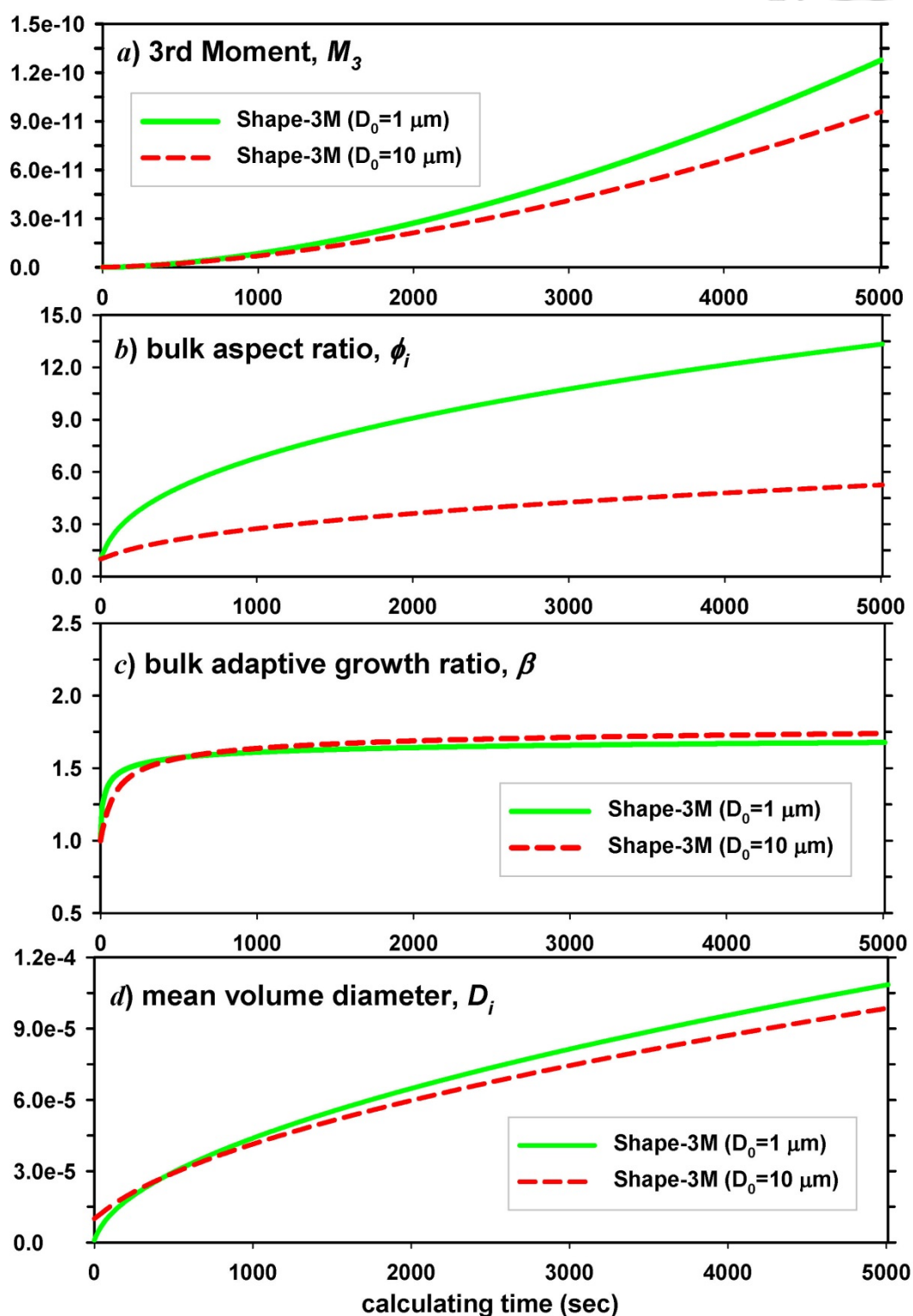
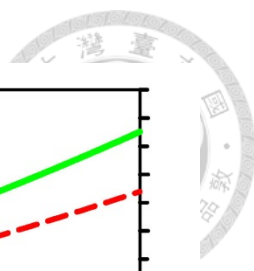


Figure 3.8 The calculation results of (a) the 3rd-moment, (b) the bulk aspect ratio, (c) the bulk adaptive growth ratio, and (d) the mean volume diameter with the initial mean volume diameters of 1 μm (in solid-green) and 10 μm (in dash-red) both with the bulk 3-moment method. For these calculations, the environmental conditions were the same to Figure 3.2.

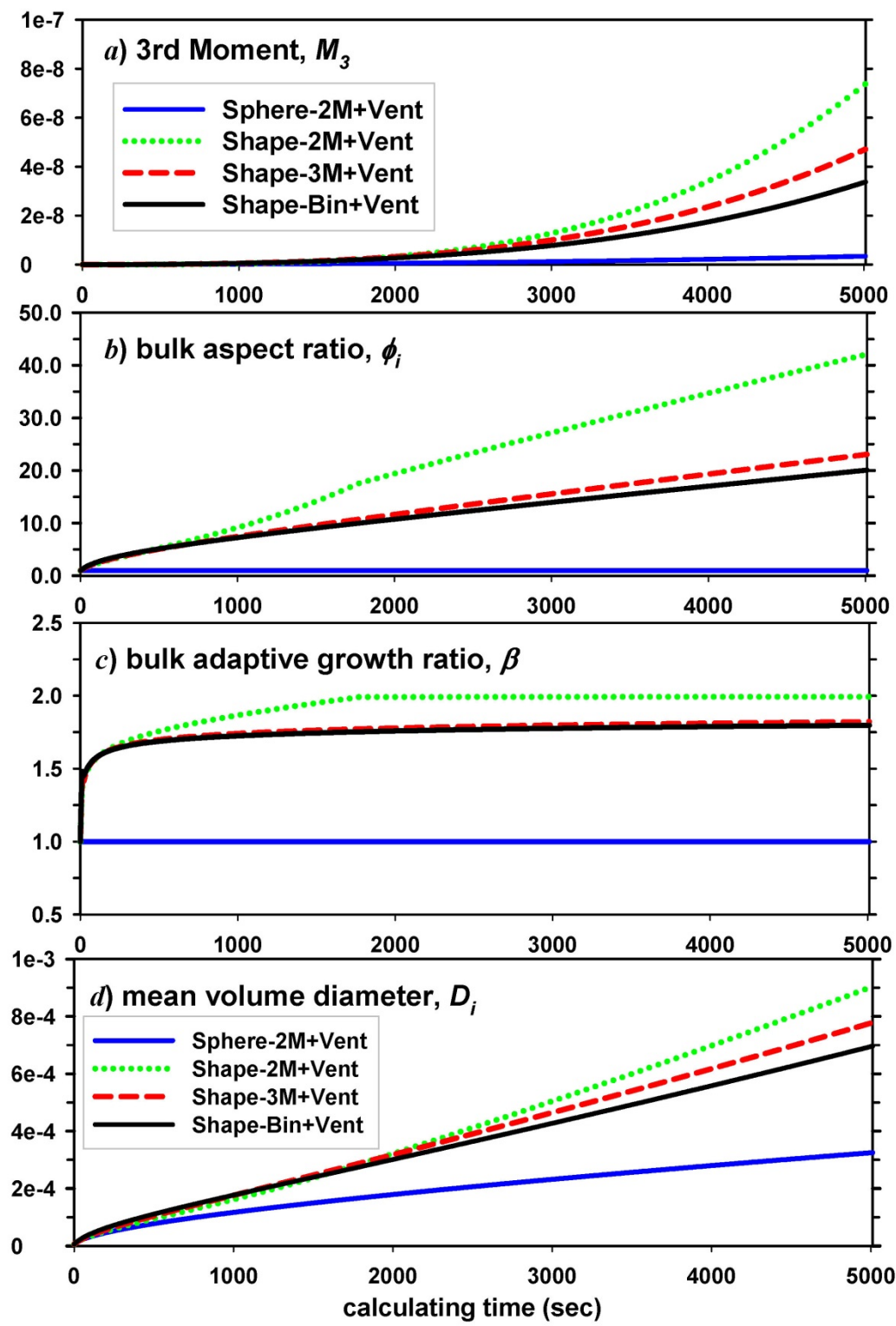
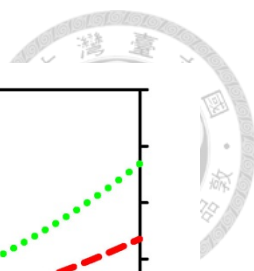


Figure 3.9 The calculation results of (a) the 3rd-moment, (b) the bulk aspect ratio, and (c) the bulk adaptive growth ratio for shape ice with the bin (in solid-black), bulk-2M (in dotted-green), and bulk-3M (in dash-red) methods, as well as for spherical ice with the bulk method (in solid-blue). For these calculations, $T=266\text{K}$, $P=800\text{ hpa}$, $\Delta Q_{vi}=5 \times 10^{-5}\text{ kg kg}^{-1}$, and $\Gamma(T)=2.0$.

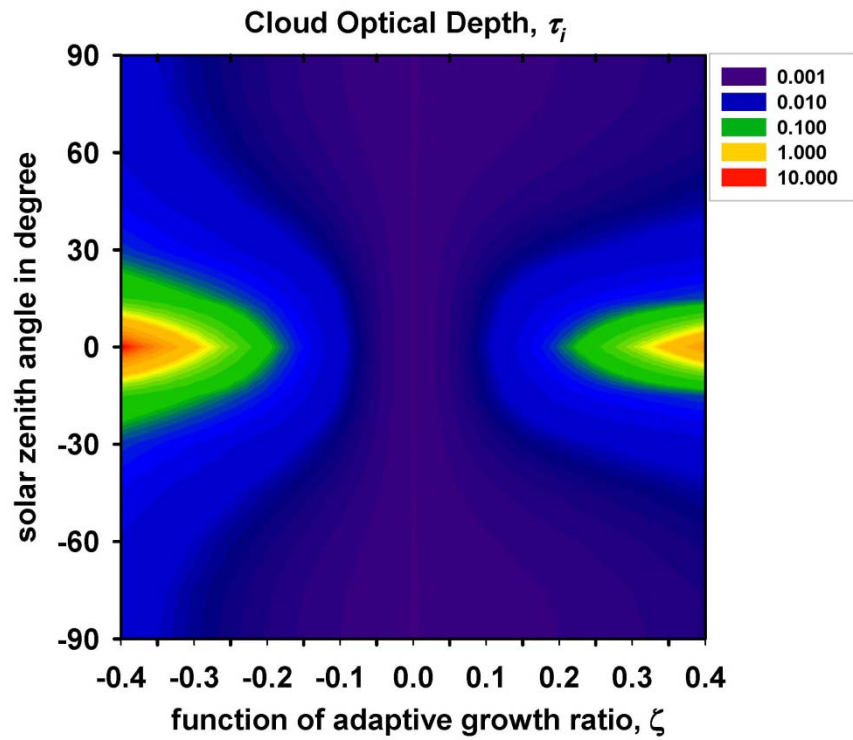
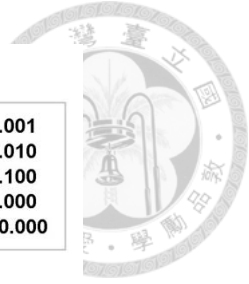


Figure 3.10 The shaded contour plot of ice optical depth (τ_i) against the adaptive growth ratio (ζ , x -axis) and solar zenith angle (θ_s , y -axis). In this calculation, the ice equivalent diameter (D_i) was assumed to be $100 \mu\text{m}$, $Q_i = 4.71 \times 10^{-6} \text{ kg}$, $\lambda_i = 4.93 \times 10^4 \text{ m}^{-1}$, $N_i = 10^4 \text{ m}^{-3}$, $\alpha_i = 3$, $z = 10^4 \text{ m}$, and $\rho_i = 900 \text{ kg m}^{-3}$.

C3VP(2007) domain setup and terrain height

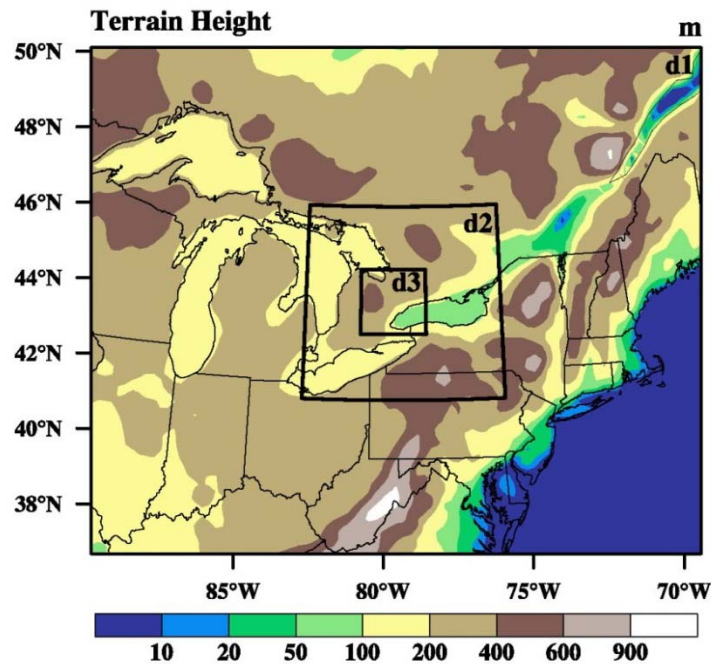


Figure 4.1 The model domain setup and terrain height (m) for C3VP case.

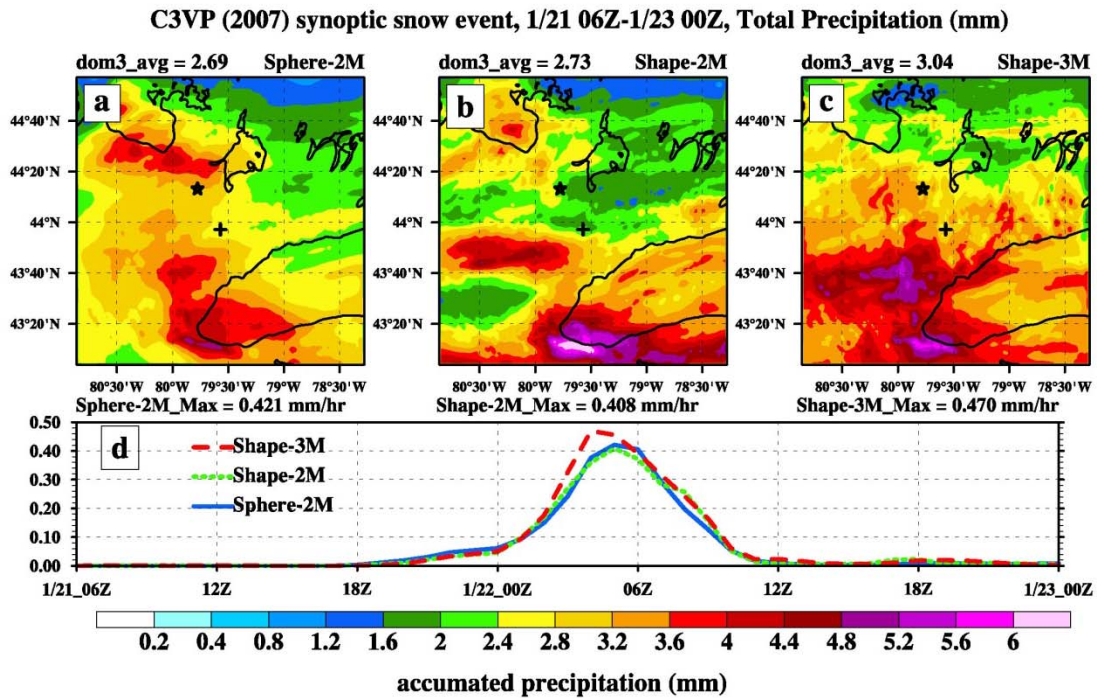
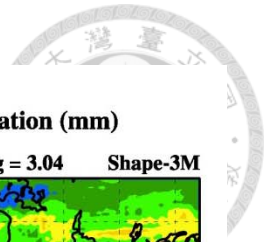
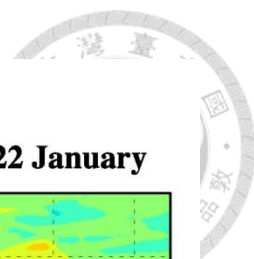


Figure 4.2 The simulation results of accumulated precipitation (mm) for (a) Sphere-2M, (b) Shape-2M, (c) Shape-3M runs, and a time series plot of domain-averaged precipitation intensity (mm hr^{-1}) depicted in (d) separately for Sphere-2M (in solid blue), Shape-2M (in dotted-green), and Shape-3M (in dash-red) runs over the inner domain within the simulation period from 06Z 21 January to 00Z 23 January 2007. The cross and star symbols represented the locations of the Centre for Atmospheric Research Experiments (CARE, 44.23°N , 79.78°W) site and the King City radar (43.96°N , 79.57°W).



C3VP(2007) vertically maximum of radar reflectivity at 00Z 22 January

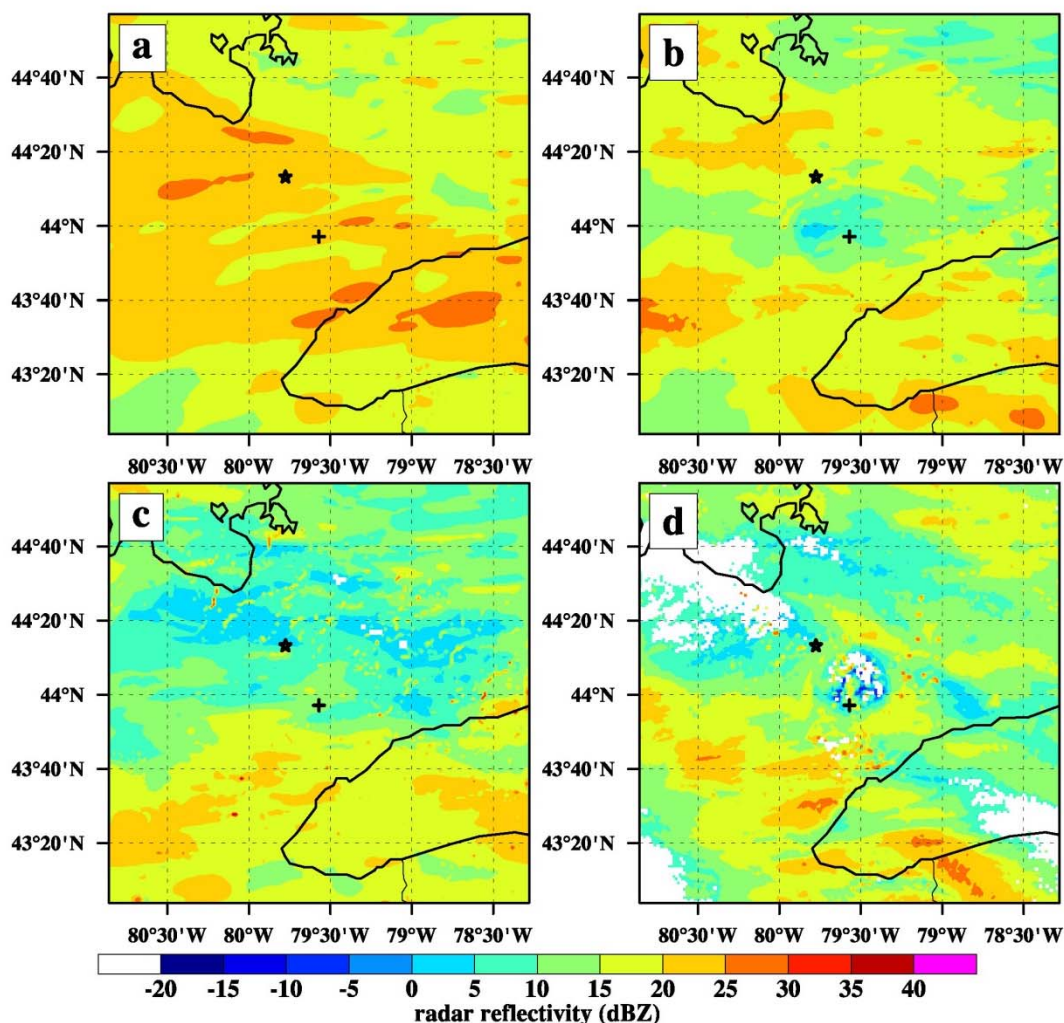
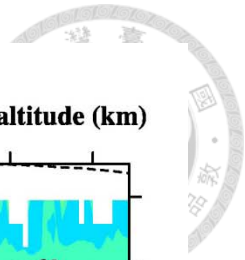


Figure 4.3 Snapshots of horizontal distributions of vertically maximum radar reflectivity (dBZ) at 00Z 22 January 2007 derived from the model simulation results of (a) Sphere-2M, (b) Shape-2M, and (c) Shape-3M runs, and the observation of the C-band King City radar depicted in (d). The radar measurement was provided by Dr. Takamichi Iguchi and Dr. Jaijn-Jung Shi at NASA/GSFC.



C3VP(2007) latitudinal averaged of radar reflectivity at 00Z 22 January by altitude (km)

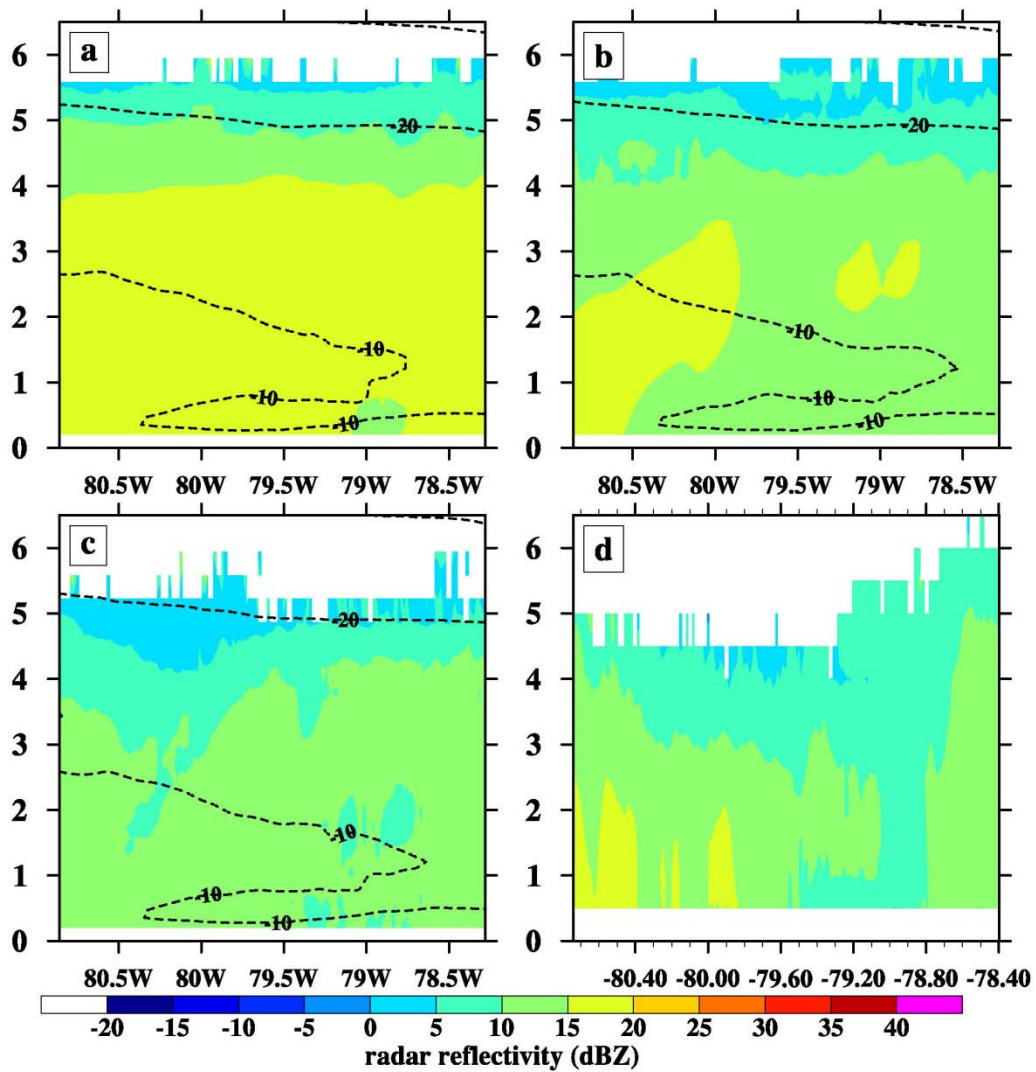
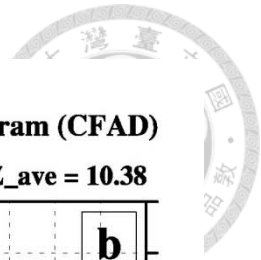


Figure 4.4 Latitudinal averaged of radar reflectivity (dBZ) by altitude (km) derived from the (a) Sphere-2M, (b) Shape-2M, and (c) Shape-3M simulation results at 00Z 22 January 2007. Panel(d) indicated the measurement of King City radar which was provided by Dr. Takamichi Iguchi and Dr. Jainn-Jung Shi at NASA/GSFC.



C3VP(2007) Normalized Contoured Frequency with Altitude Diagram (CFAD)

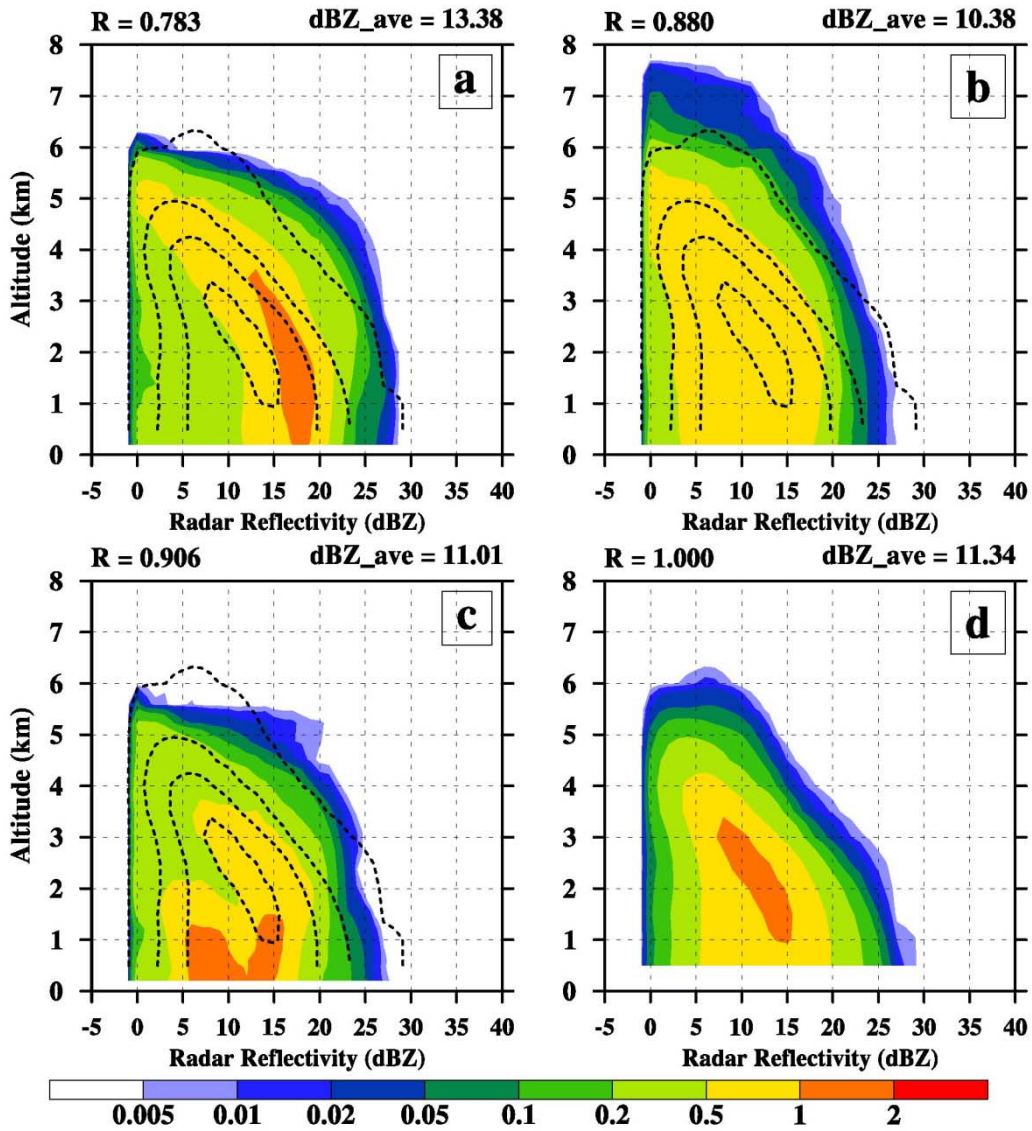
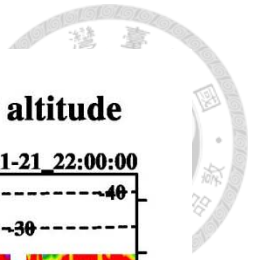


Figure 4.5 Normalized contoured frequency with altitude (km) diagram of radar reflectivity derived from the simulations of the (a) Sphere-2M, (b) Shape-2M, (c) Shape-3M, and the measurement of the (d) King City radar from the period of 00Z 22 January to 12Z 22 January 2007. The correlation (R) for each panel was determined against to the observation and the overlay black dash lines were the contour edges equal to 0.005, 0.2, 0.5, and 1 of the results in (d). The radar measurement was provided by Dr. Takamichi Iguchi and Dr. Jainn-Jung Shi at NASA/GSFC.



C3VP (2007) latitudinal averaged of ice aspect ratio by altitude

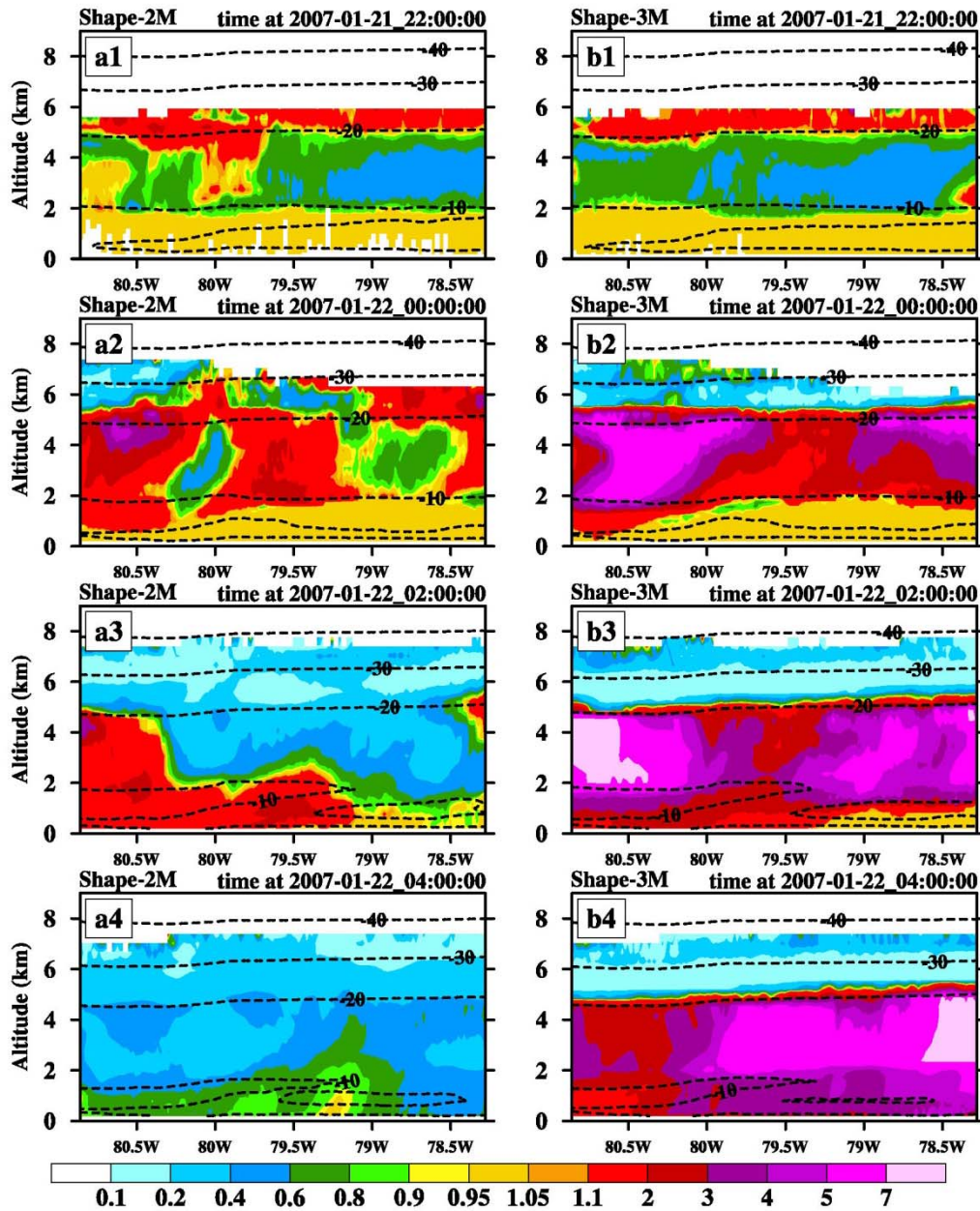


Figure 4.6 The vertical profiles of the simulated pristine ice aspect ratios ($\phi_i > 1.05$ for columnar, $\phi_i < 0.95$ for planar, otherwise for spherical crystals in orange) averaged by longitude within the latitude between 43.5°N and 44.5°N over the inner-domain for the (a) Shape-2M and (b) Shape-3M runs from the simulating period at (1) 22Z 21 January, (2) 00Z 22 January, (3) 02Z 22 January, to (4) 04Z 22 January 2007. The overlay black dash line was for the averaged ambient temperature ($^\circ\text{C}$) and the y-axis denoted the altitude in km.

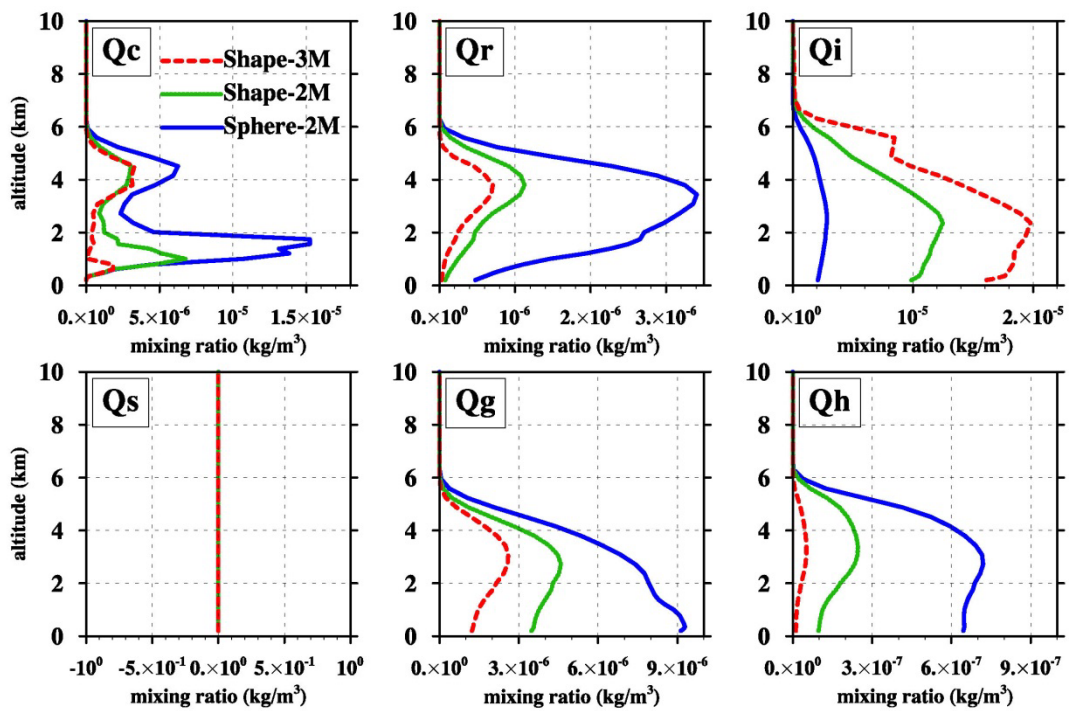


Figure 4.7 The vertical profiles of the inner-domain-averaged mixing ratio (kg m^{-3}) from 06Z 21 to 00Z 23 January for cloud droplets (Q_c), rain drops (Q_r), pristine ice (Q_i), snow-aggregates (Q_s), graupel (Q_g), and hail (Q_h) separately for the Sphere-2M (in solid blue), Shape-2M (in dotted green), and Shape-3M (in dash red) runs. The y-axis denoted the altitude in km.

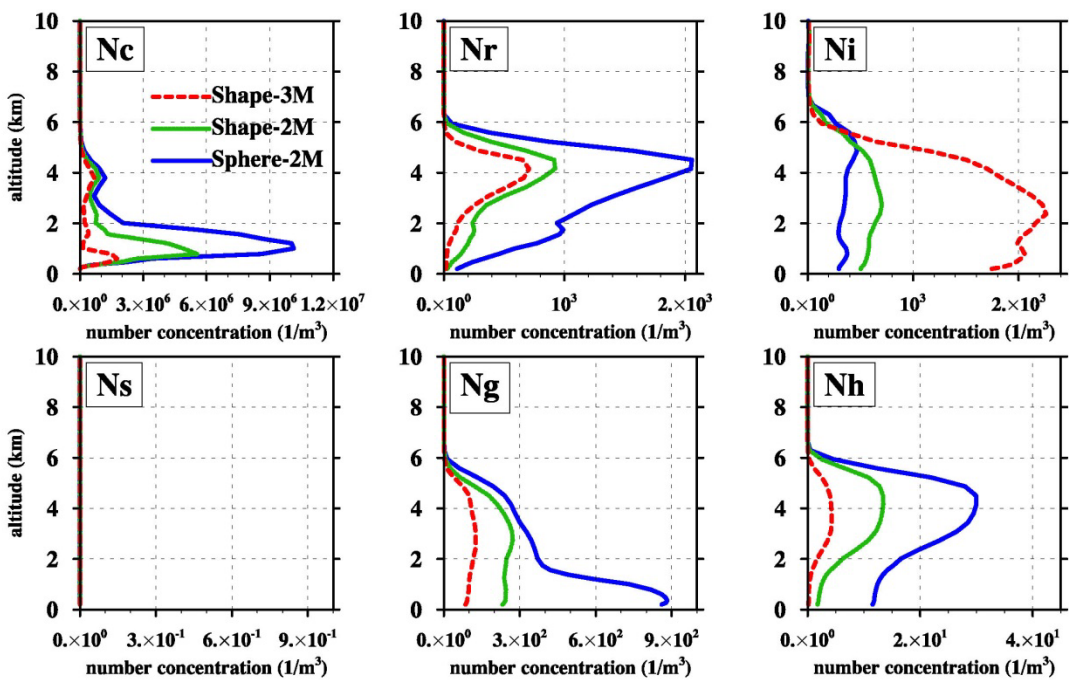


Figure 4.8 Same as Figure 4.7 but for number concentration (m^{-3}).

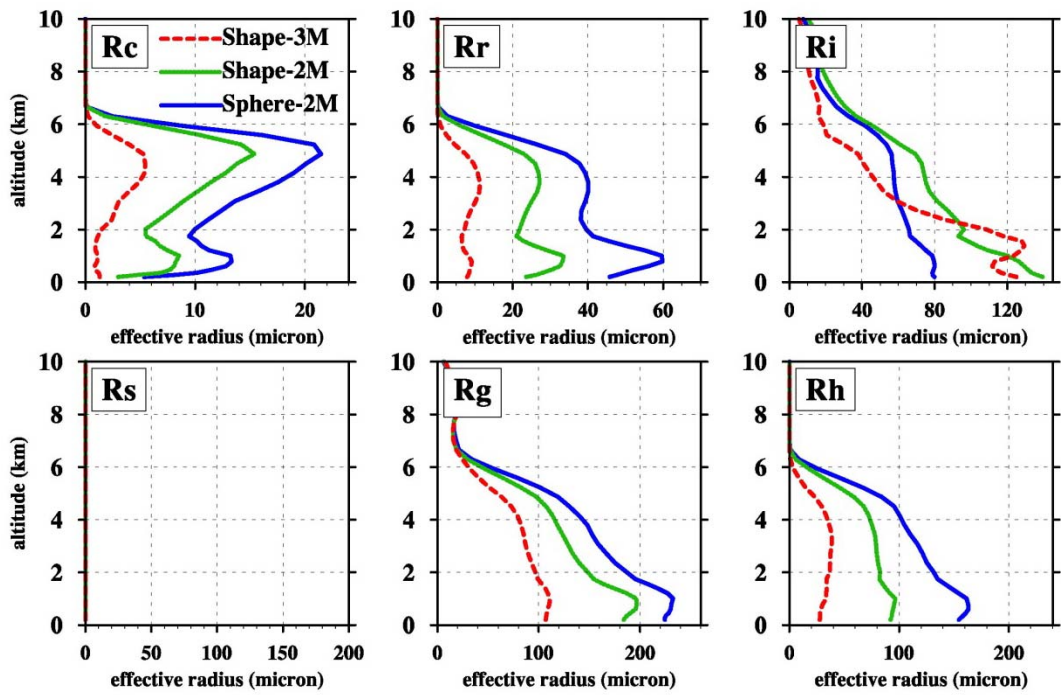


Figure 4.9 Same as Figure 4.7 but for effective radius (μm).

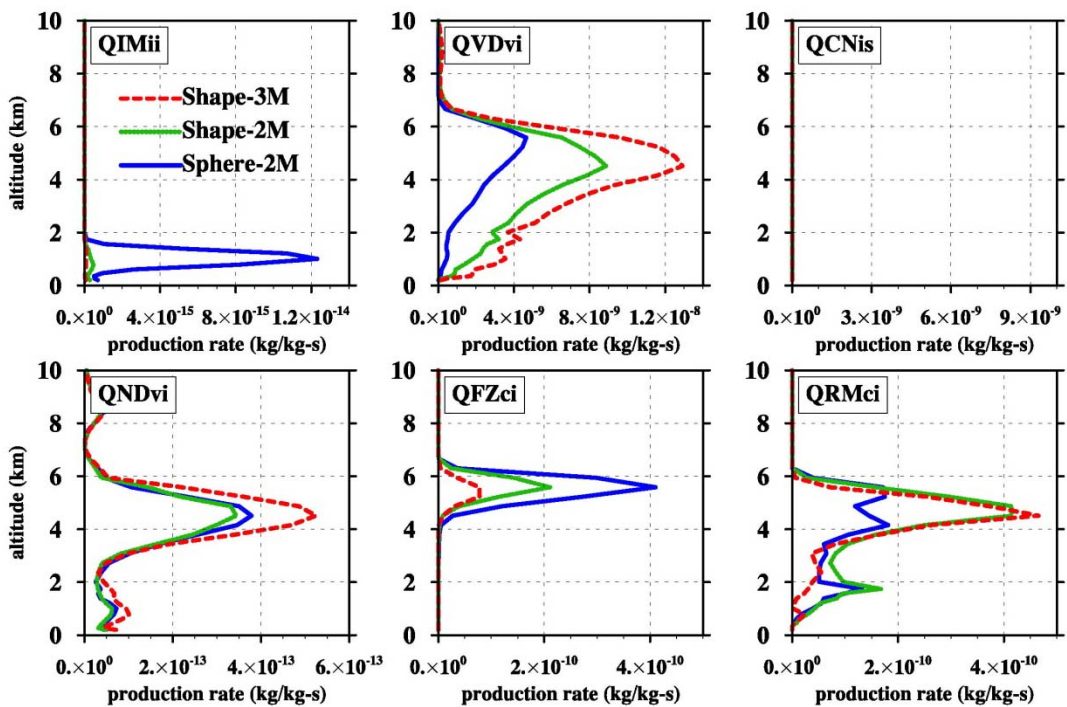


Figure 4.10 Same as Figure 4.7 but for mixing ratio change rates ($\text{kg kg}^{-1} \text{s}^{-1}$) of pristine ice. $QIMii$ for multiplication, $QVDvi$ for deposition growth, $QCNis$ for aggregation to snow-aggregates, $QNDvi$ for deposition-nucleation, $QFZci$ for cloud droplets freezing, and $QRMci$ for riming growth.

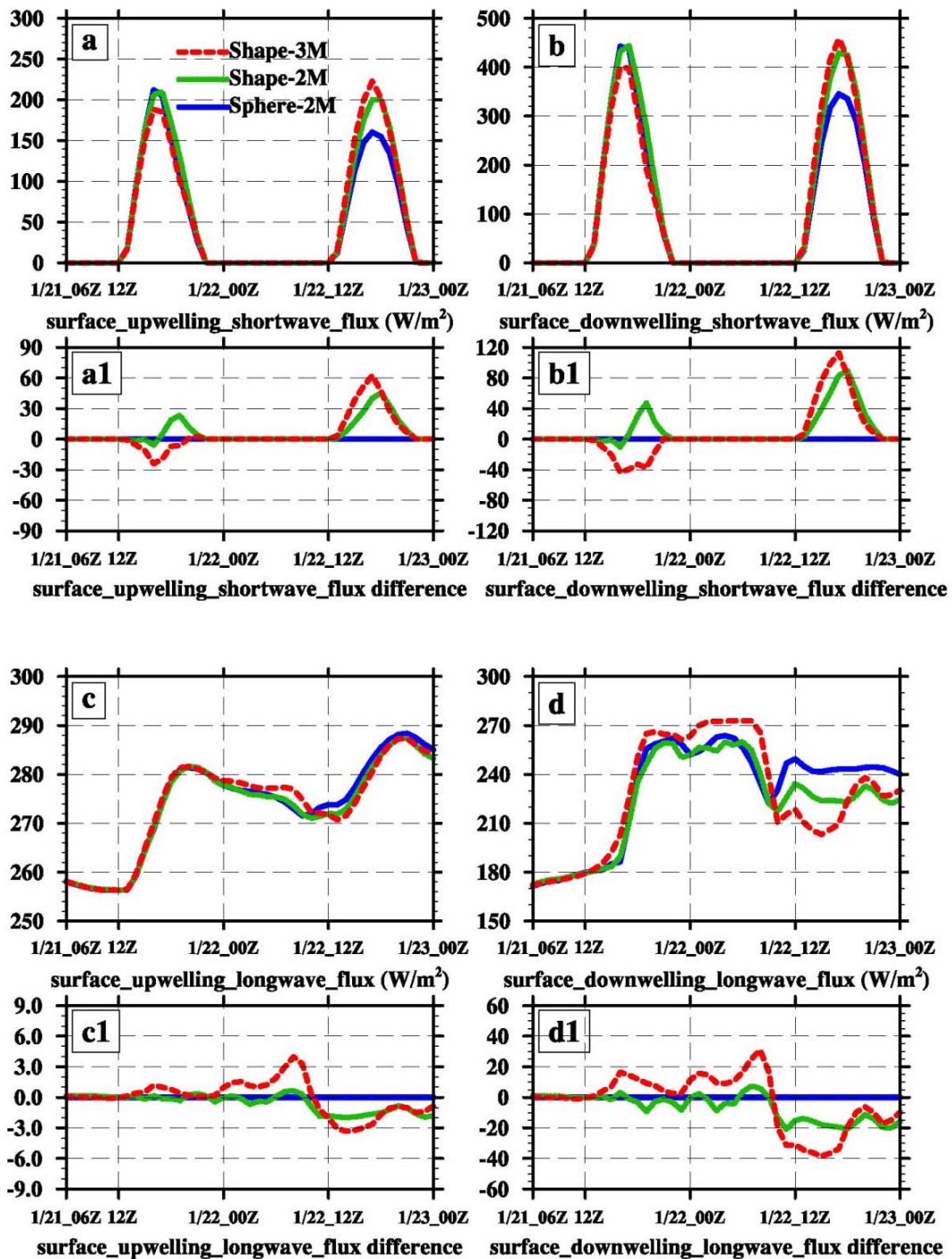
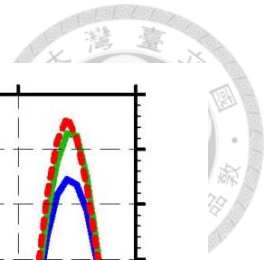


Figure 4.11 The time series plots of the inner-domain-averaged surface radiation fluxes (in W m^{-2}) for (a) the upwelling shortwave flux (in negative), (b) the downwelling shortwave flux, (c) the upwelling longwave flux (in negative), and (d) the downwelling longwave flux separately for Sphere-2M (in solid blue), Shape-2M (in dotted green) and Shape-3M (in dash red) runs. Panels (l) were the differences compared to the result of Sphere-2M run.



DIAMET(2011) doamin setup and terrain height

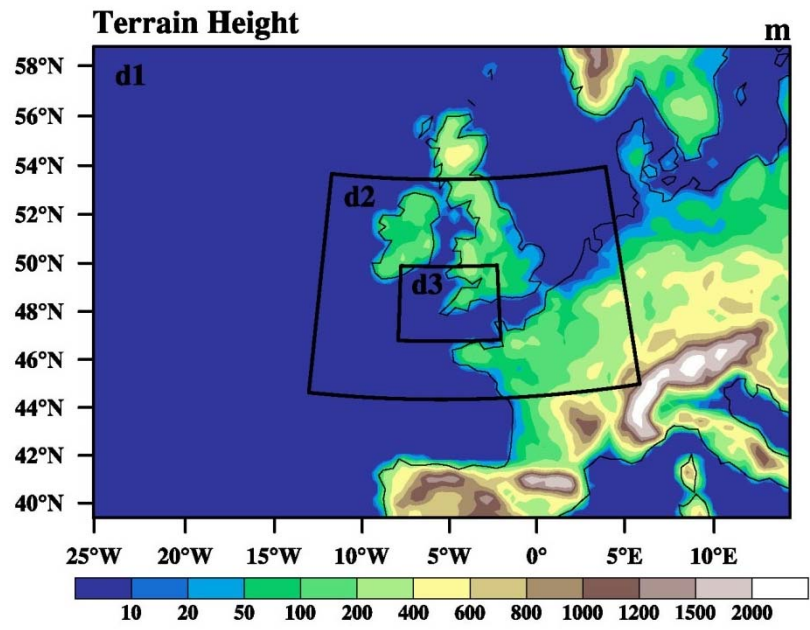


Figure 4.12 The model domain setup and terrain height (*m*) for DIAMET case.

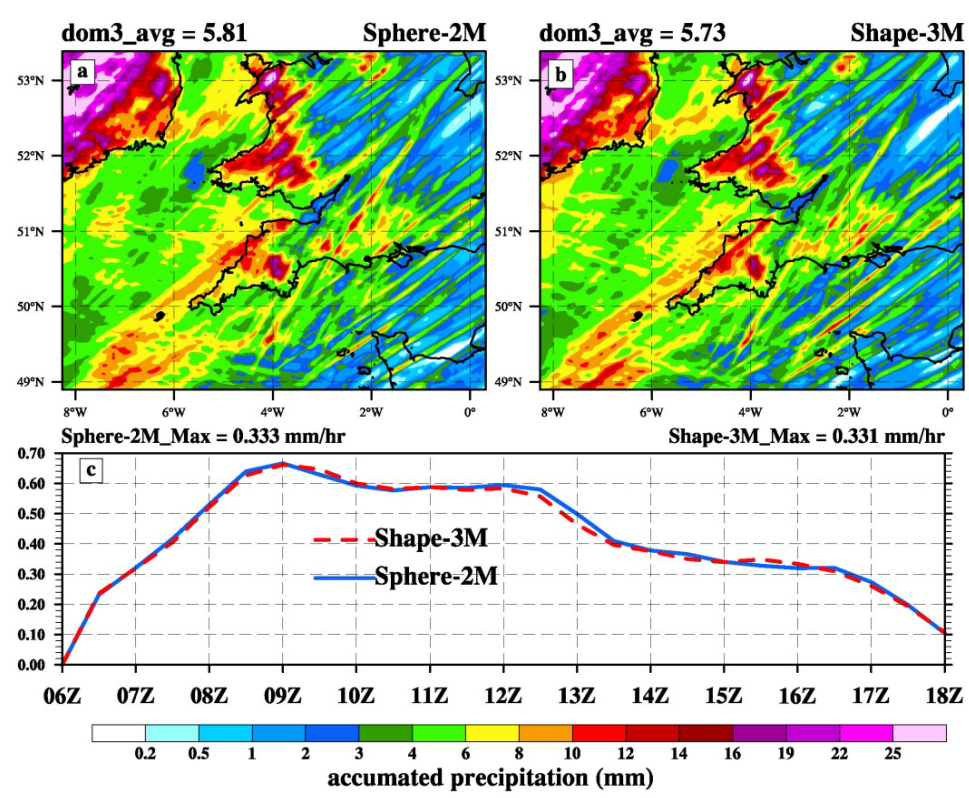


Figure 4.13 The simulation results of accumulated precipitation (mm) for (a) Sphere-2M, and (b) Shape-3M runs, and a time series plot of domain-averaged precipitation intensity (mm hr^{-1}) depicted in (c) separately for Sphere-2M (in solid blue), and Shape-3M (in dash red) runs over the inner domain.

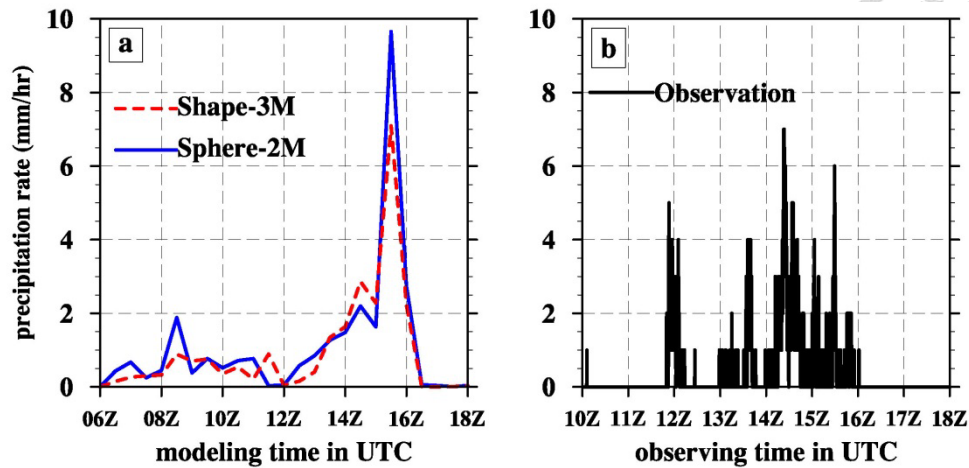


Figure 4.14 The time series plots of precipitation rate (mm hr^{-1}) for (a) model simulations (Sphere-2M in solid blue and Shape-3M in dash red) and (b) ground-based observation (in black bar) at the Chilbolton Facility for Atmospheric and Radio Research site (CFARR, 51.15°N , 1.44°W). The ground-based rainfall observation was provided by Dr. Christopher Dearden at University of Manchester.

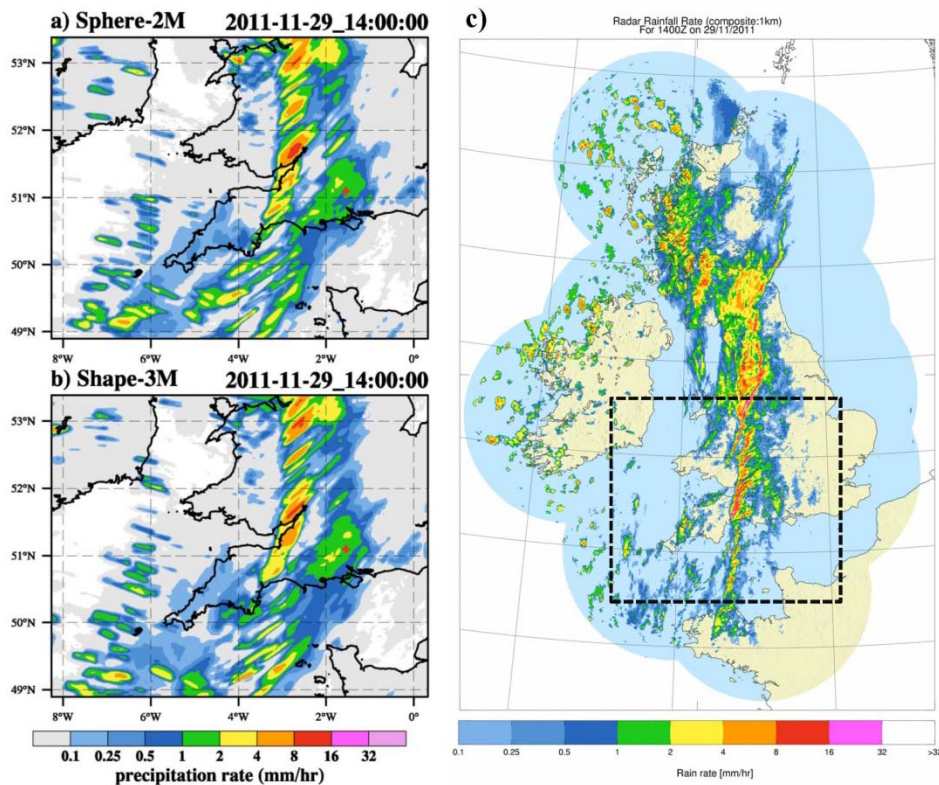


Figure 4.15 Precipitation rate in mm hr^{-1} for the (a) Sphere-2M, (b) Shape-3M model results, and (c) estimated from the ground-based S-band Chilbolton Advanced Meteorological Radar (CAMR) observation at 14Z 29 November 2011. The red-cross spot was the location of the CAMR site, and the dash black square was corresponding to the model inner domain. Panel (c) was provided by Dr. Christopher Dearden at University of Manchester.

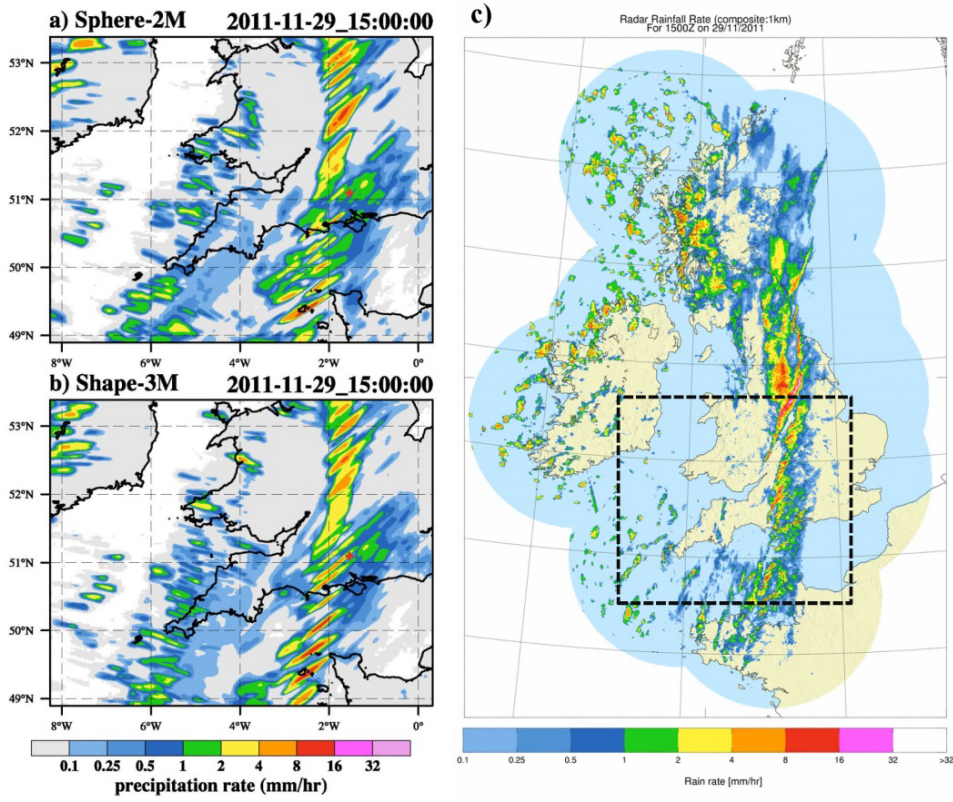
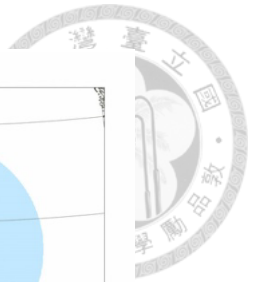


Figure 4.16 Same as Figure 4.15 but for the time period of 15Z.

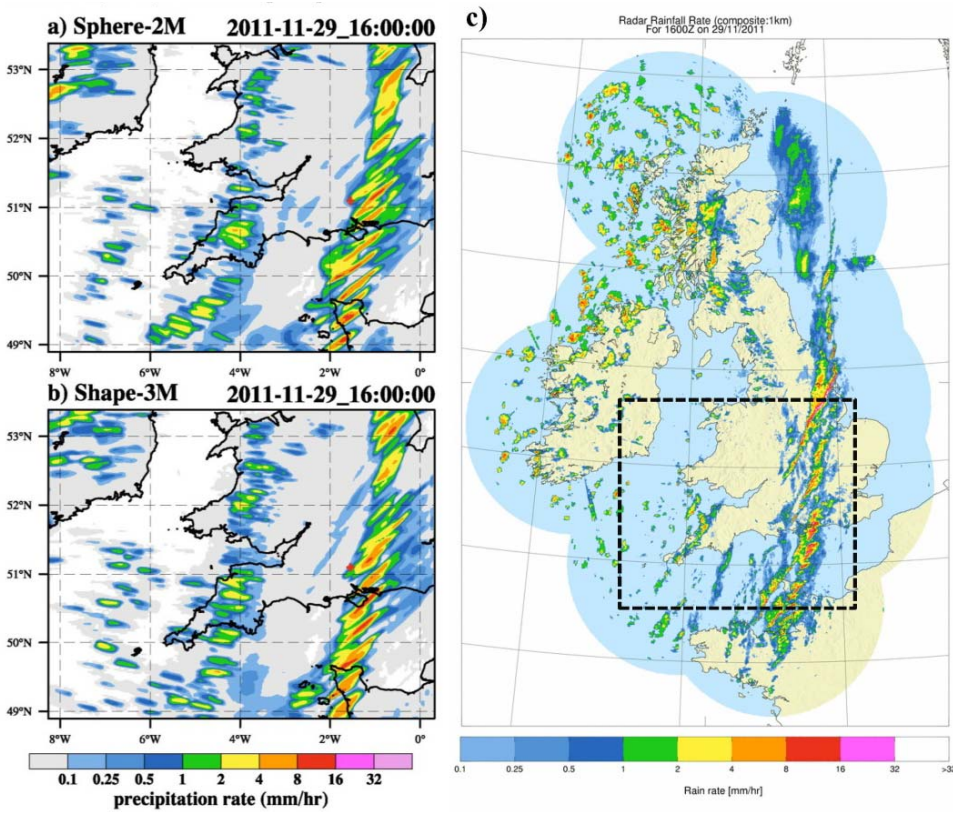


Figure 4.17 Same as Figure 4.15 but for the time period of 16Z.

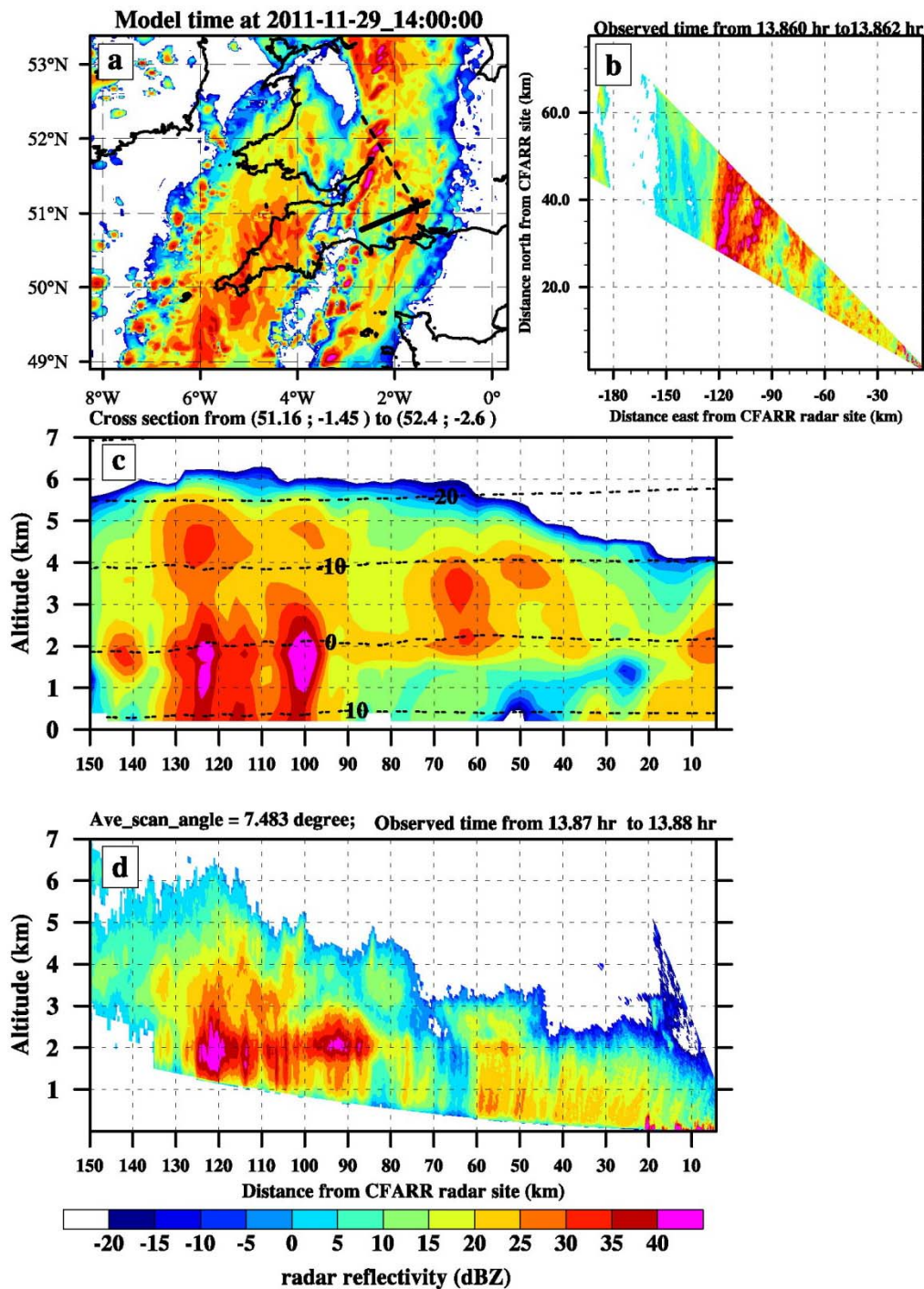


Figure 4.18 The plots of radar reflectivity (dBZ) derived from the Shape-3M simulation result at an altitude of 2 km above ground level with a solid black line for the horizontal flight track and a dash black line for the corresponding cross section in (c). Panel (b) depicted the CAMR radar observation in the scanning mode of PPI at 1351 UTC with an elevation angle of 0.5° and the azimuth angles from 283.20° to 292.95° . Panel (d) was for the RHI scanning mode at 1352 UTC with an averaged elevation angle of 7.483° and a fixed azimuth angle of 283° . The radar measurement was provided by Dr. Christopher Dearden at University of Manchester.

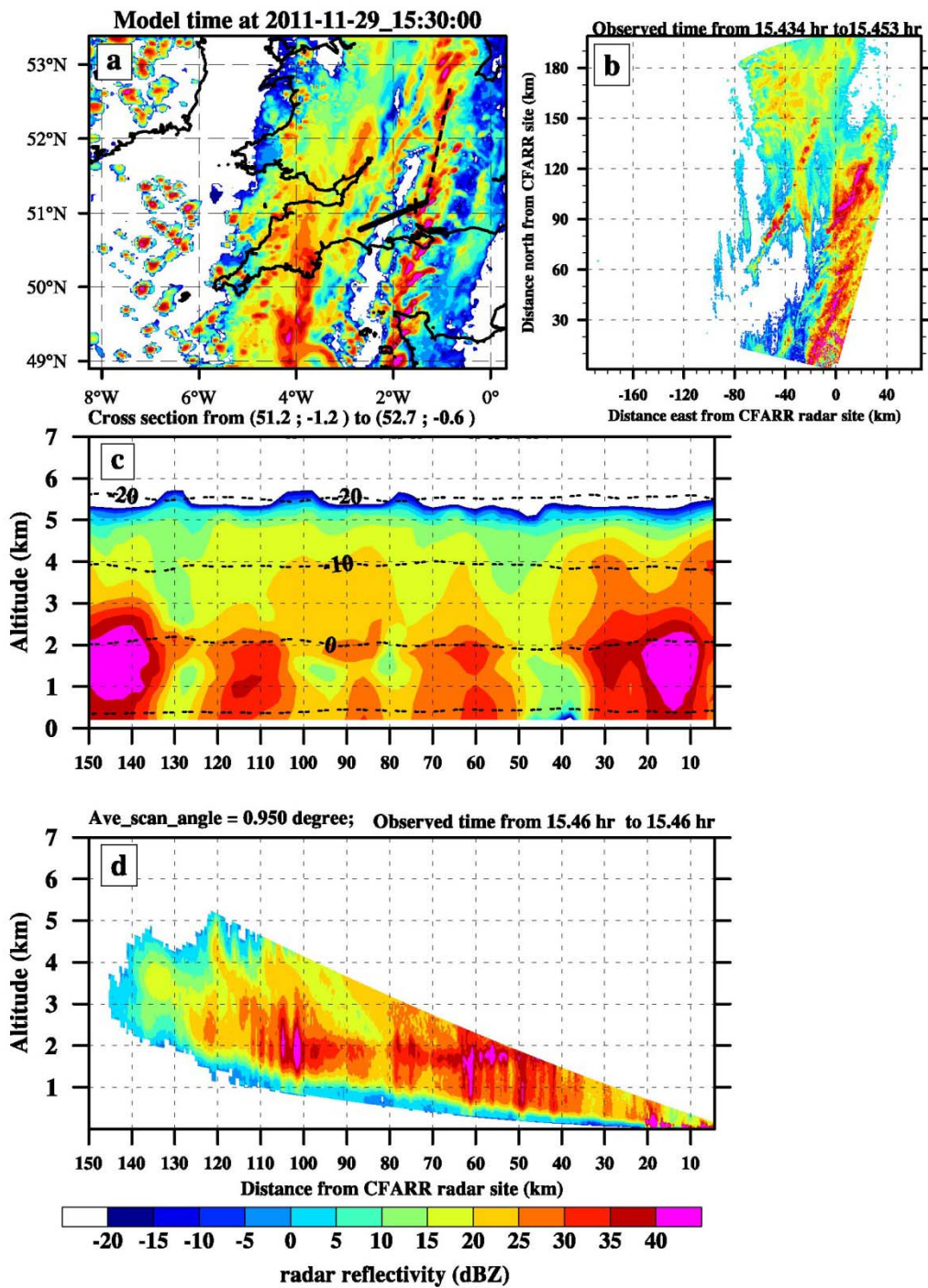


Figure 4.19 Same as Figure 4.18 but at the period of 15.5Z for the model result in (a) and (c). Panel (b) depicted the CAMR radar observation in the scanning mode of PPI at 1525 UTC with an elevation angle of 0.5° and the azimuth angles from 280.02° to 379.79° . Panel (d) was for the RHI scanning mode at 1527 UTC with an averaged elevation angle of 0.95° and a fixed azimuth angle of 366.99° . The radar measurement was provided by Dr. Christopher Dearden at University of Manchester.

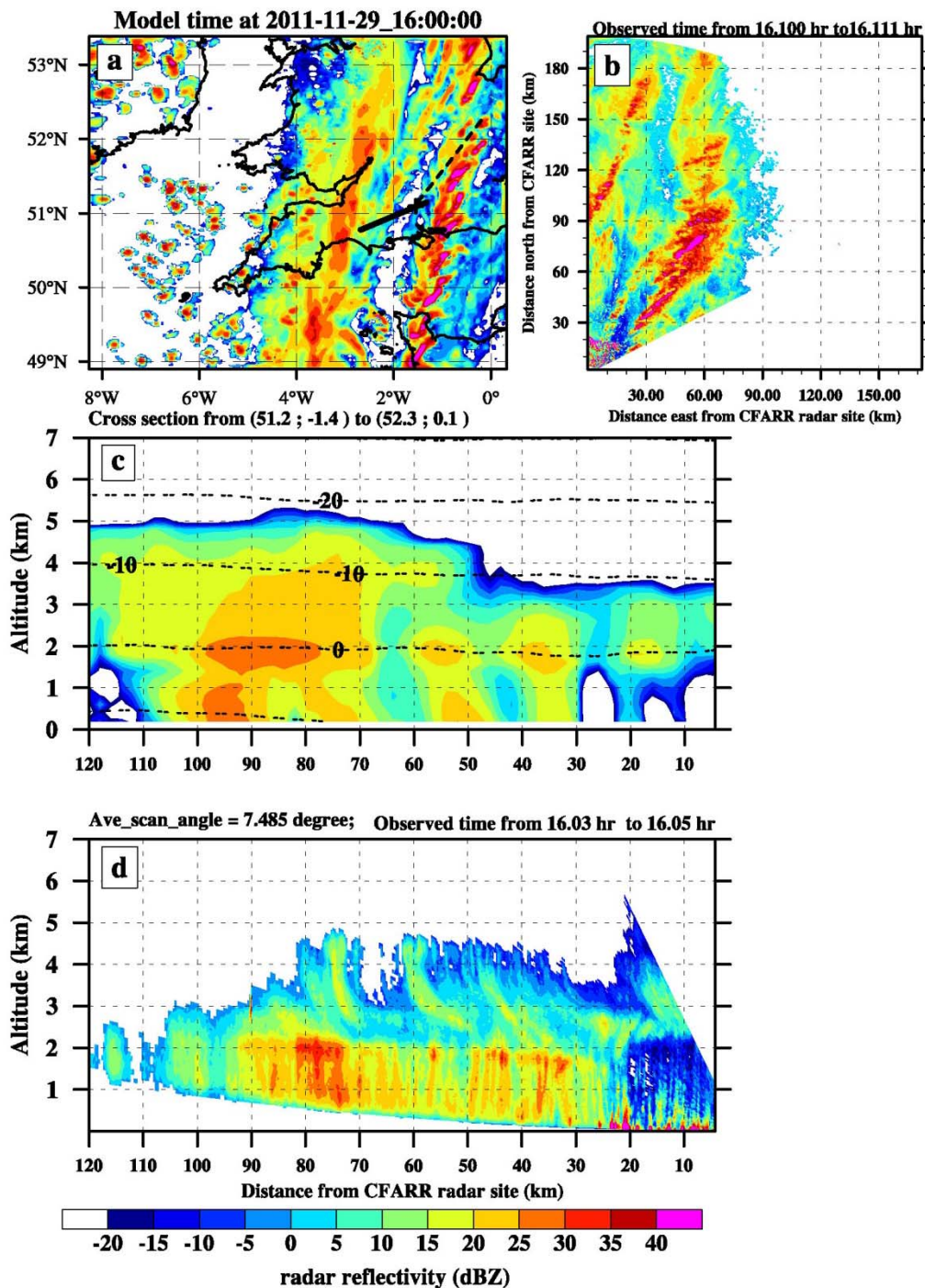


Figure 4.20 Same as Figure 4.18 but at the period of 16Z for the model result in (a) and (c). Panel (b) depicted the CAMR radar observation in the scanning mode of PPI at 1605 UTC with the elevation angles from 0.48° to 0.50° and the azimuth angles from 0.052° to 59.78° . Panel (d) was for the RHI scanning mode at 1601 UTC with an averaged elevation angle of 7.485° and a fixed azimuth angle of 44° . The radar measurement was provided by Dr. Christopher Dearden at University of Manchester.

DIAMET(2011) Normalized Contoured Frequency with Altitude Diagram (CFAD)

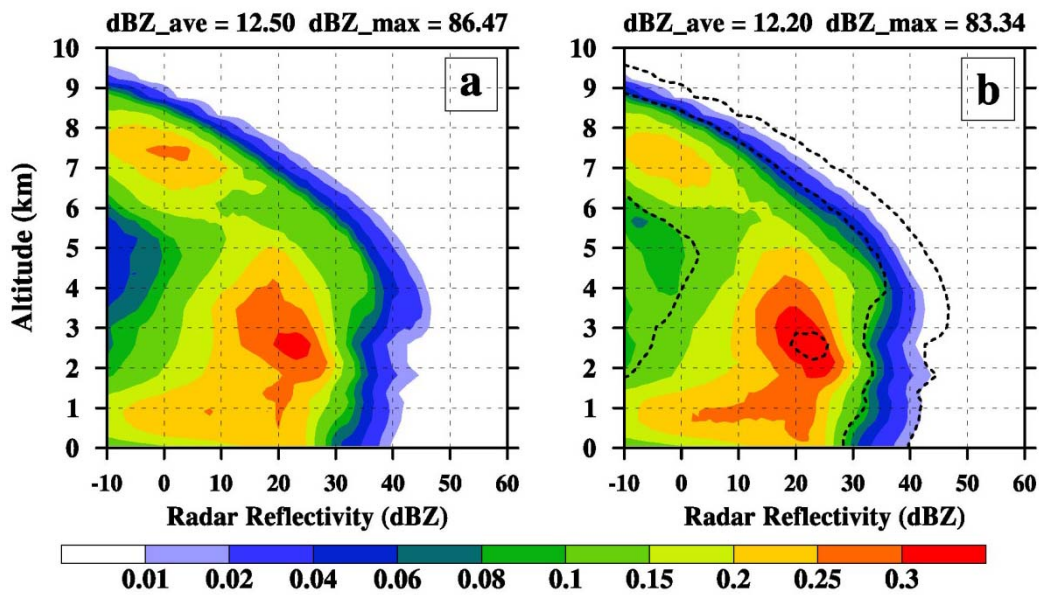
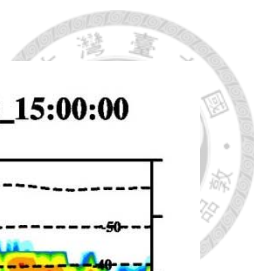


Figure 4.21 Normalized contoured frequency with altitude diagram of radar reflectivity derived from the inner-domain simulations of the (a) Sphere-2M and (b) Shape-3M runs from 06Z to 18Z 29 November 2011. The overlay black dash lines were the contour edges equal to 0.01, 0.1, and 0.3 of the results in (a).



DIAMET (2011) flight-area_avg_contour at time 2011-11-29_15:00:00

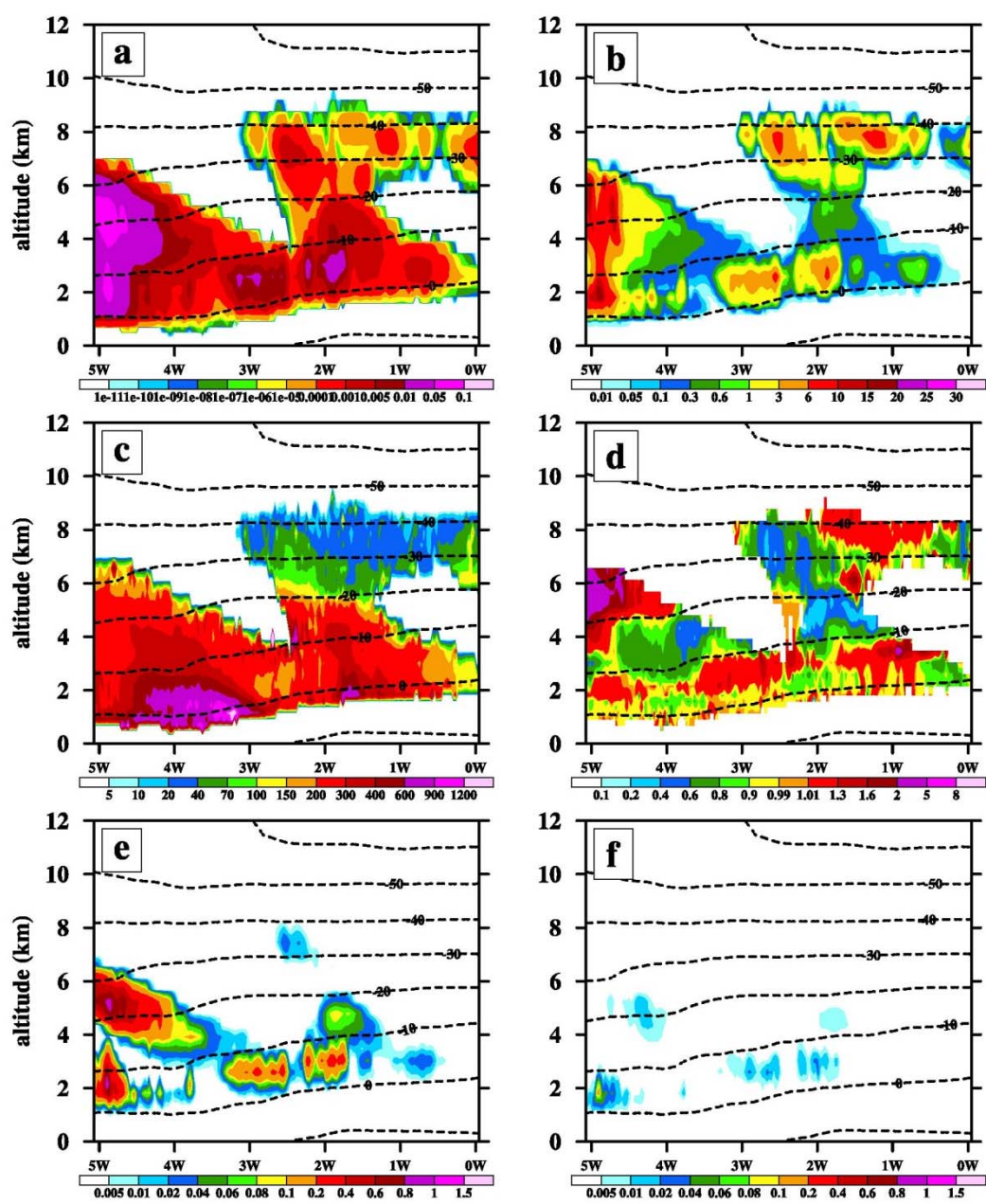
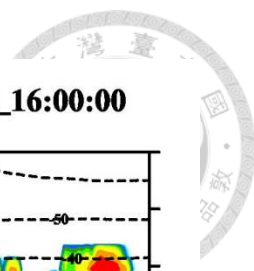


Figure 4.22 The vertical shaded contour plots of the inner-domain-averaged by longitude within the flight track region in latitude between 50.5°N and 51.5°N for the pristine ice (a) mixing ratio (g kg^{-1}), (b) number concentration (L^{-1}), (c) mean volume diameter (μm), (d) bulk aspect ratio ϕ_i , (e) deposition heating rate (K hr^{-1}), and (f) riming heating rate (K hr^{-1}) at the simulating period of 15Z 29 November 2011 for the Shape-3M run. The overlay black dash line was for the averaged ambient temperature ($^{\circ}\text{C}$) and the y-axis denoted the altitude in km.



DIAMET (2011) flight-area_avg_contour at time 2011-11-29_16:00:00

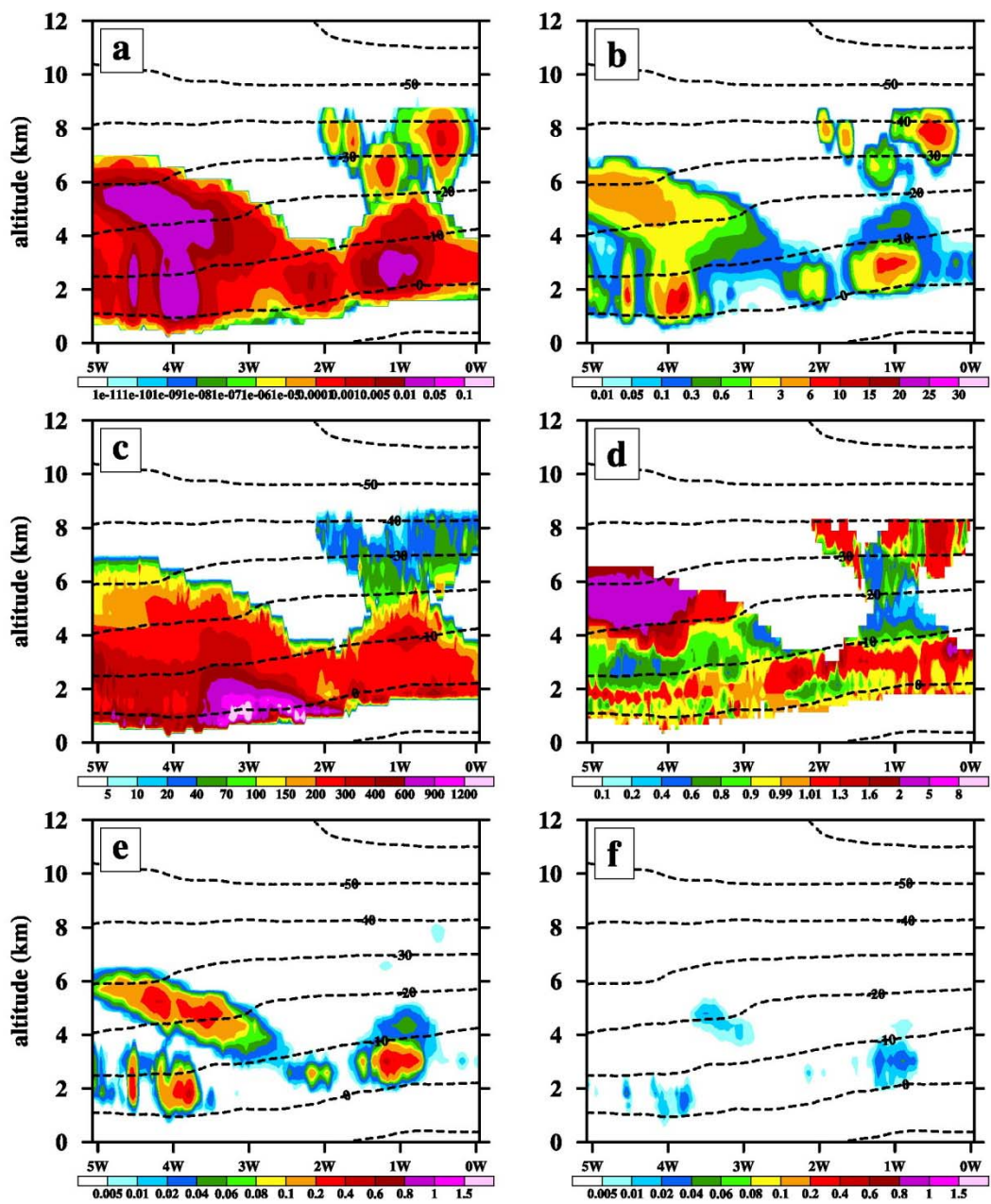


Figure 4.23 Same as Figure 4.22, but for the simulation period at 16Z.

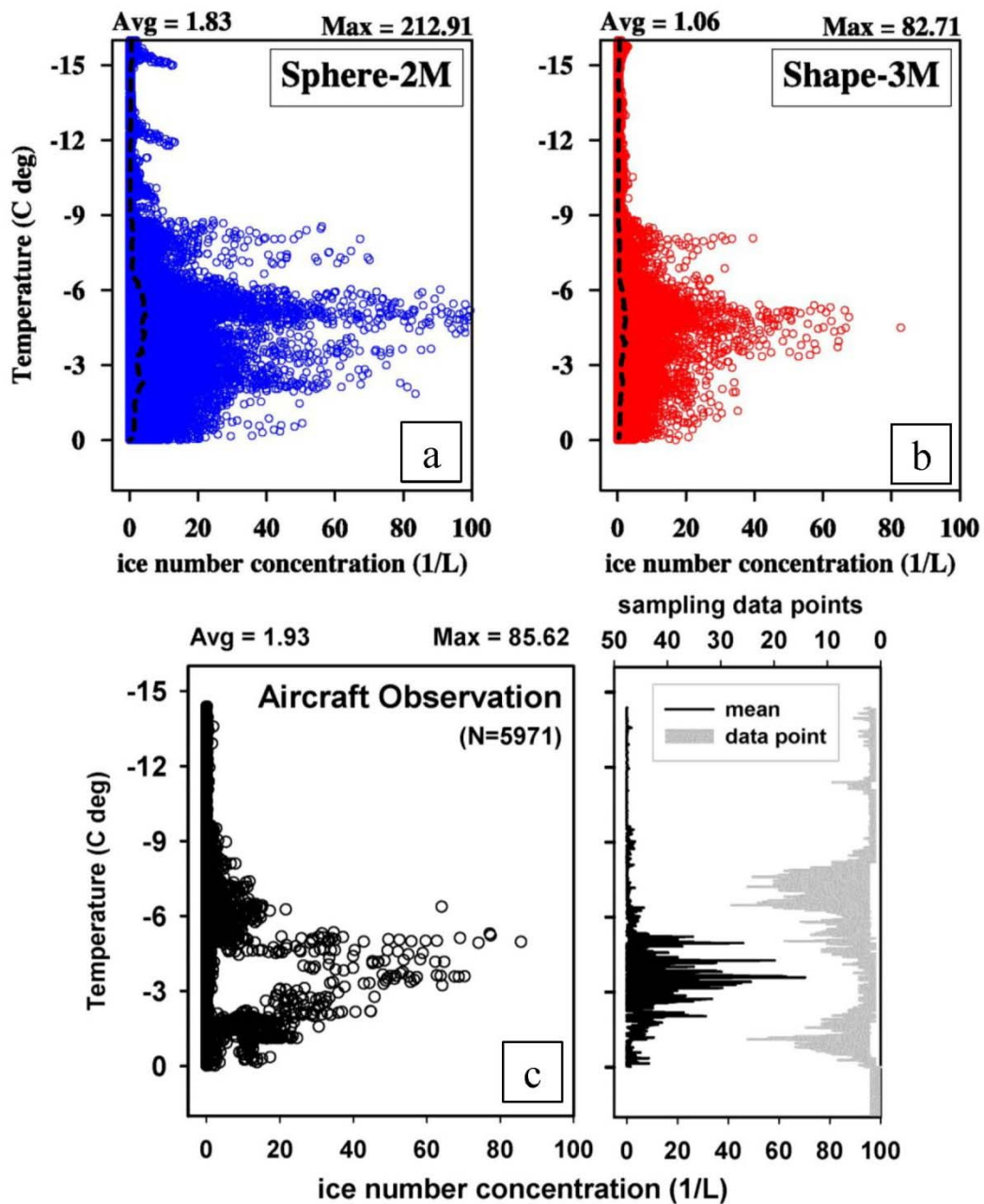


Figure 4.24 The scatter plots with mean vertical profiles (in black dash lines) of the ice number concentration (L^{-1} , x-axis) for the model (a) Sphere-2M (in blue), (b) Shape-3M run (in red), and (c) the aircraft observation (in black) with sampling data points (in grey bar) as a function of ambient temperature ($^{\circ}C$, y-axis) over the flight track area ($50.5^{\circ}N \sim 51.5^{\circ}N$; $-1^{\circ}W \sim -3^{\circ}W$) from 14Z to 16.5Z. The aircraft measurement data was provided by Dr. Christopher Dearden at University of Manchester.

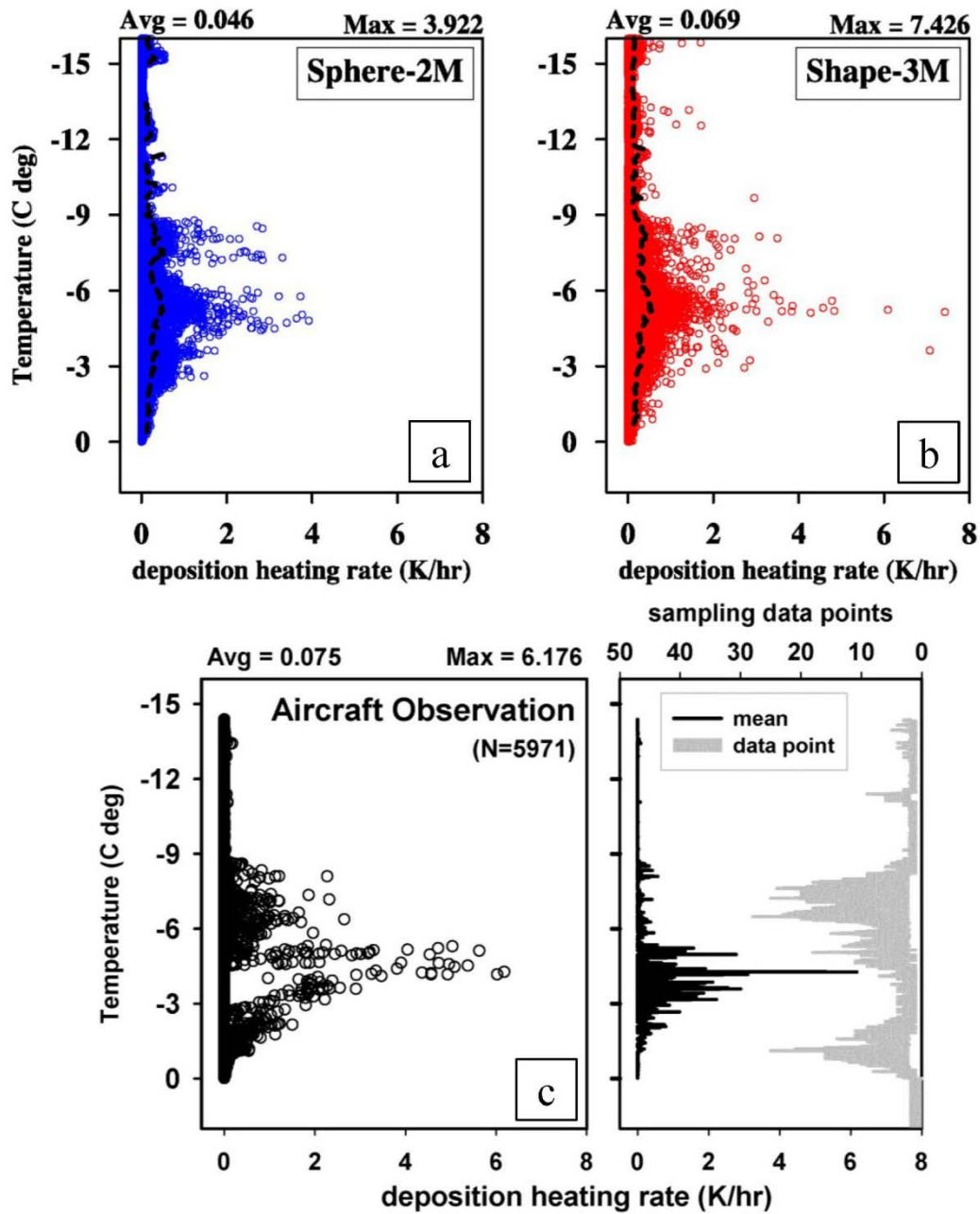


Figure 4.25 Same as Figure 4.24, but for the results of deposition heating rate (K hr^{-1} , x -axis).

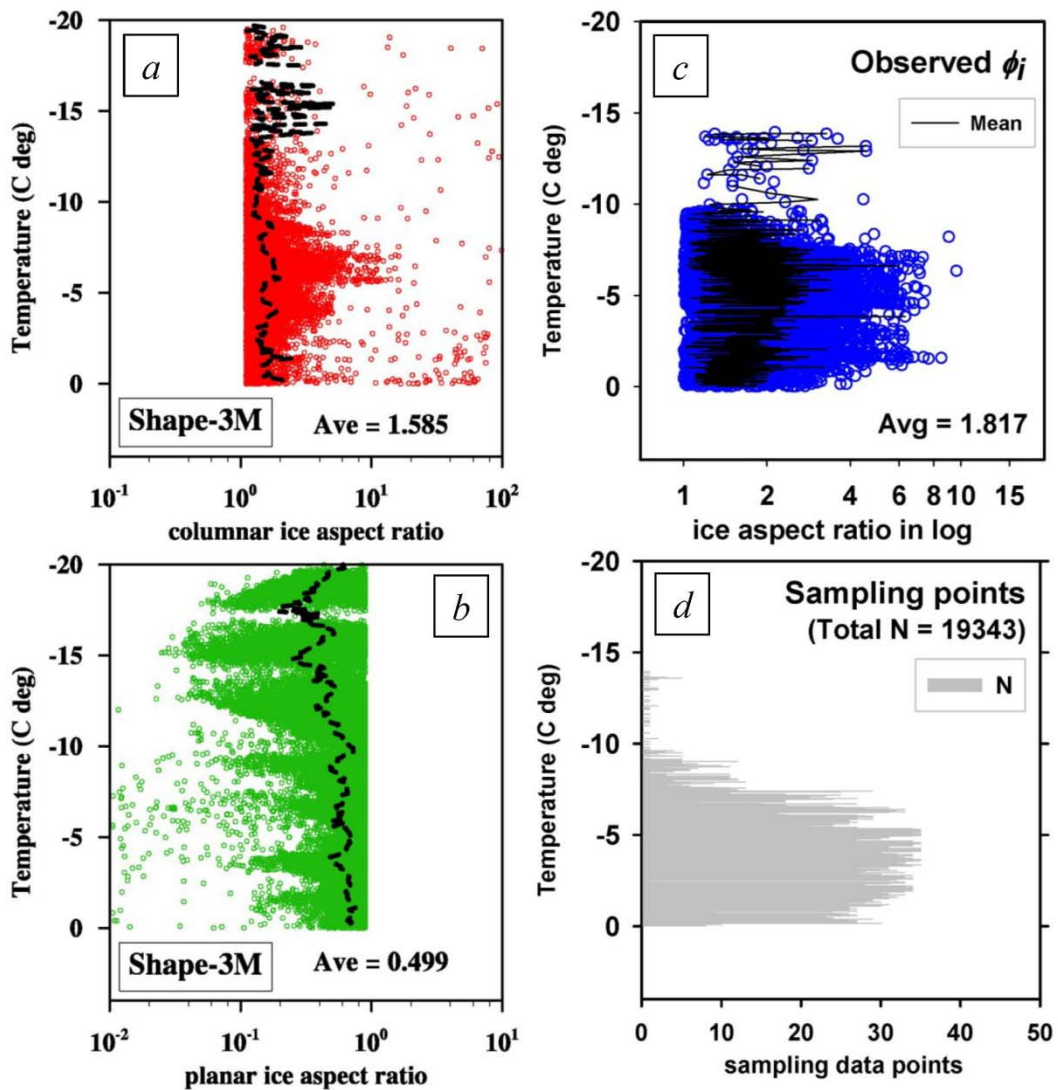


Figure 4.26 The scatter plots with mean vertical profiles (in black dash lines) of the ice aspect ratio (x -axis) derived from the model Shape-3M run for (a) column ice alone (in red), (b) planar ice alone (in green), and (c) for the aircraft observation (in blue) with (d) sampling data points (in grey bar) as a function of ambient temperature ($^{\circ}\text{C}$, y -axis) within the diameter from 50 to 400 μm over the flight track area ($50.5\sim 51.5^{\circ}\text{N}$; $-1\sim -3^{\circ}\text{W}$) from 14Z to 16.5Z. The aircraft measurement data was provided by Dr. Christopher Dearden at University of Manchester.

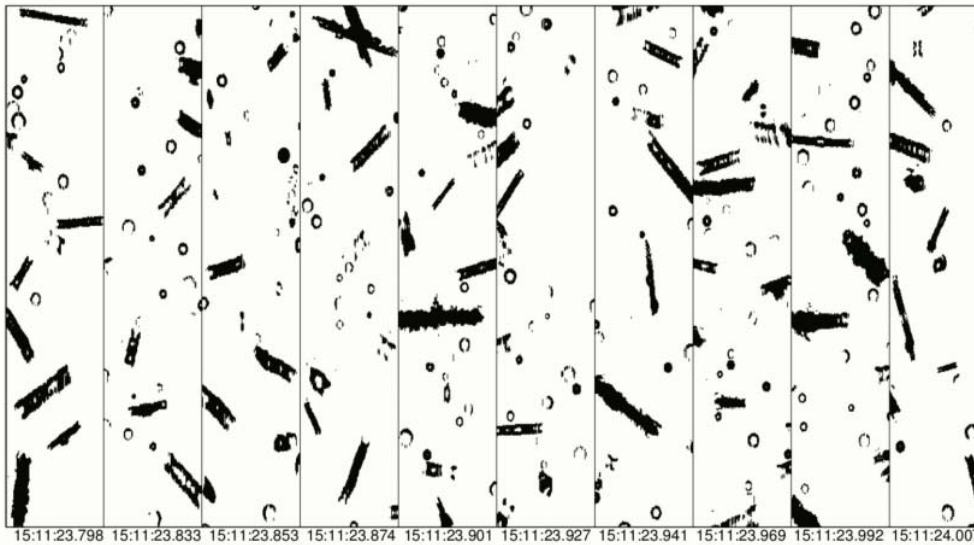


Figure 4.27 Ice crystals imaged by the 2D-S probe at 15:11Z from the aircraft observation. The circle hollow particles were cloud droplets. *The image was provided by Dr. Christopher Dearden at University of Manchester.*

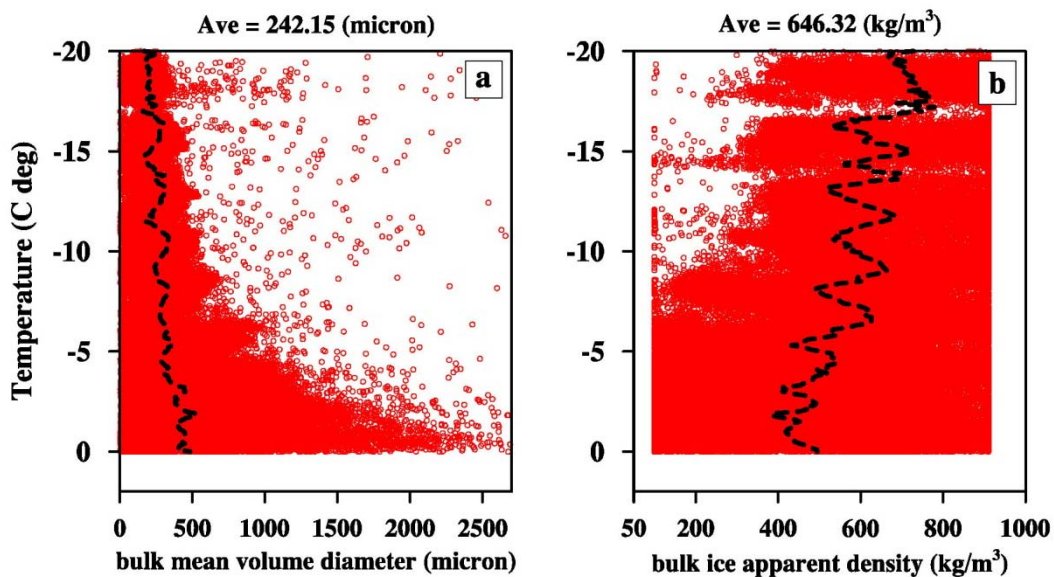


Figure 4.28 The scatter plots with mean vertical profiles (in black dash lines) of the (a) bulk mean volume diameter (μm , x -axis) and (b) apparent density (kg m^{-3} , x -axis) of pristine ice as a function of ambient temperature ($^{\circ}\text{C}$, y -axis) from the Shape-3M run over the flight track area ($50.5\sim 51.5^{\circ}\text{N}$; $-1\sim -3^{\circ}\text{W}$) from 14Z to 16.5Z.

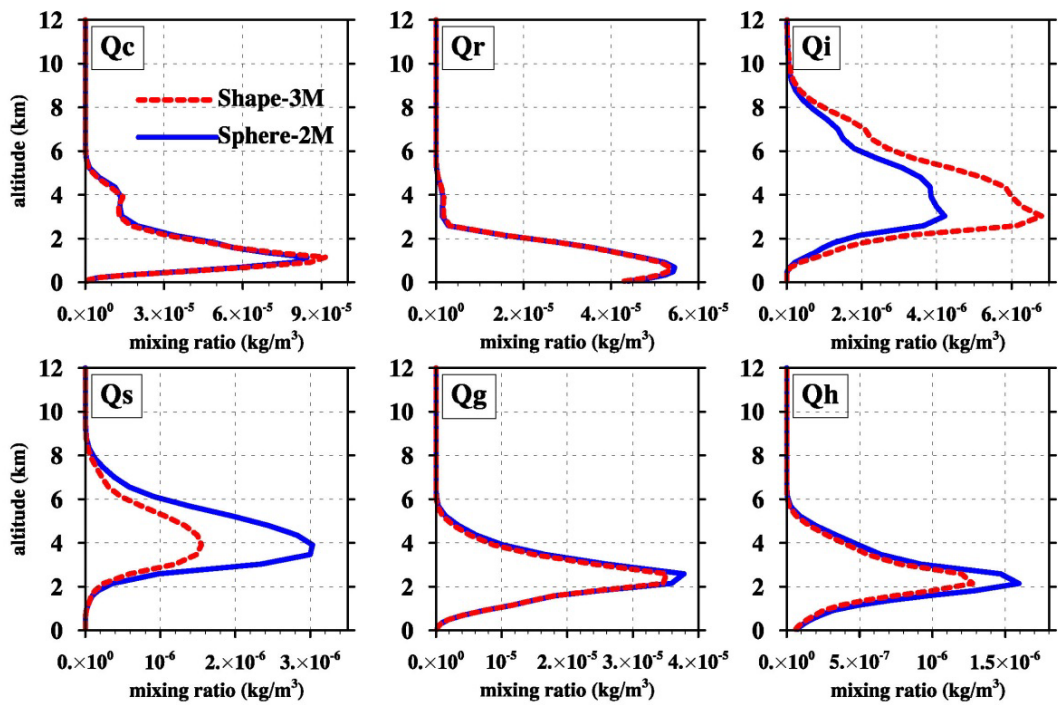


Figure 4.29 The vertical profiles of the inner-domain-averaged in mixing ratio (kg m^{-3}) within the period from 06Z to 18Z 29 November 2011 for cloud droplets (Q_c), rain drops (Q_r), pristine ice (Q_i), snow-aggregates (Q_s), graupel (Q_g), and hail (Q_h) separately for the Sphere-2M (in solid blue) and the Shape-3M (in dash red) runs. The y-axis denoted the altitude in km.

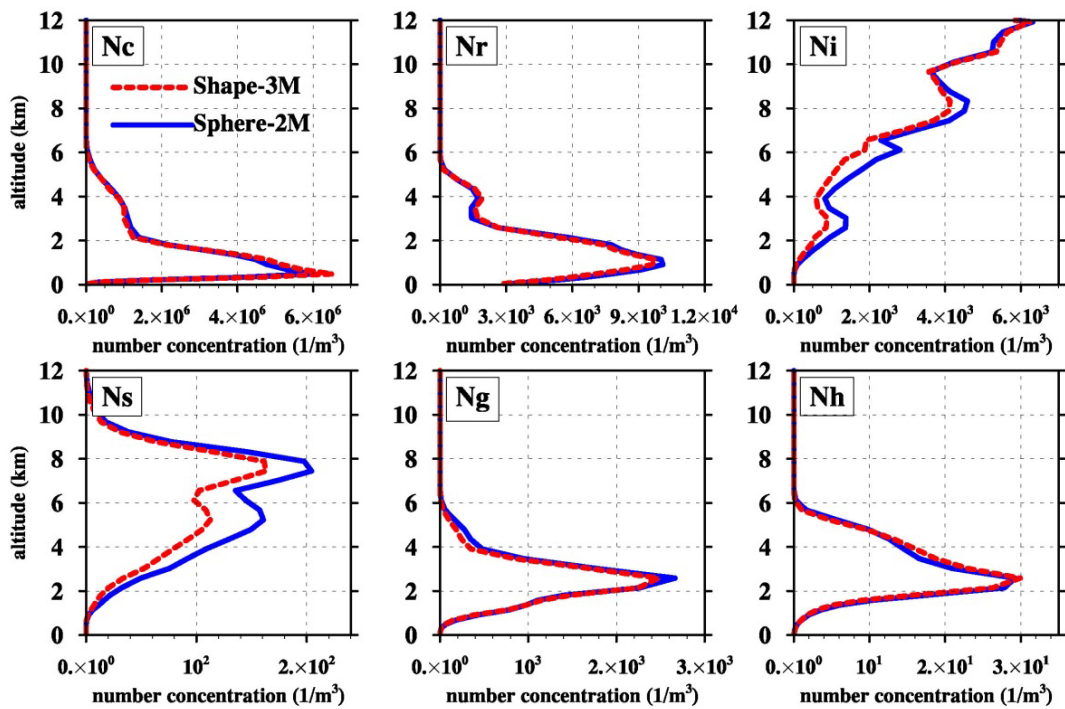


Figure 4.30 Same as Figure 4.29 but for number concentration (m^{-3}).

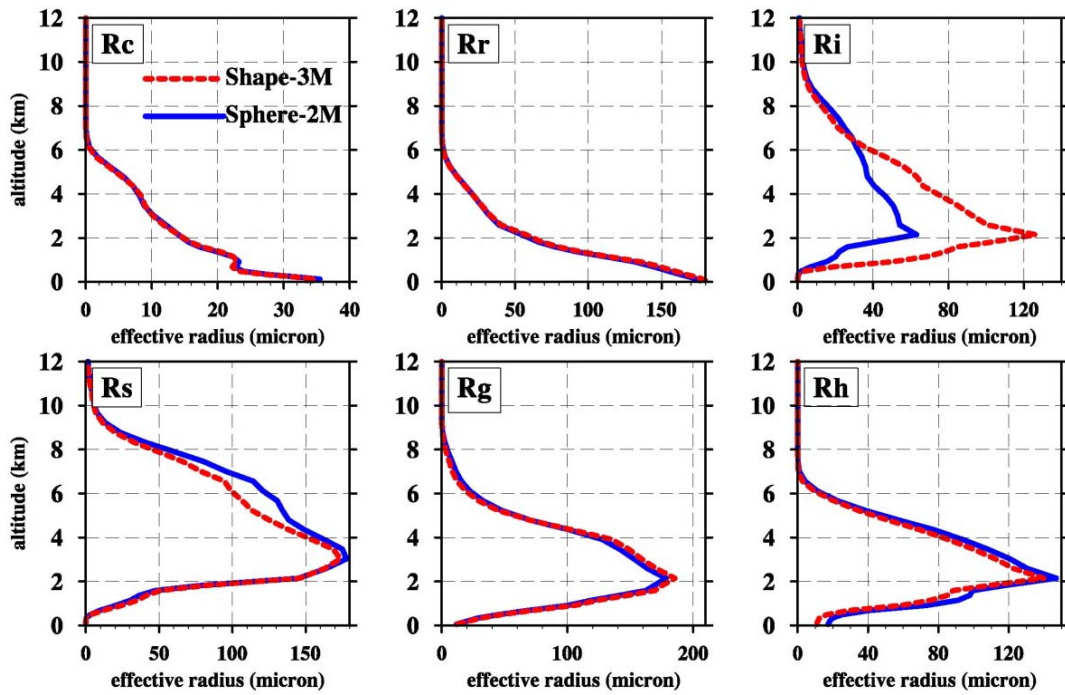


Figure 4.31 Same as Figure 4.29 but for effective radius (μm).

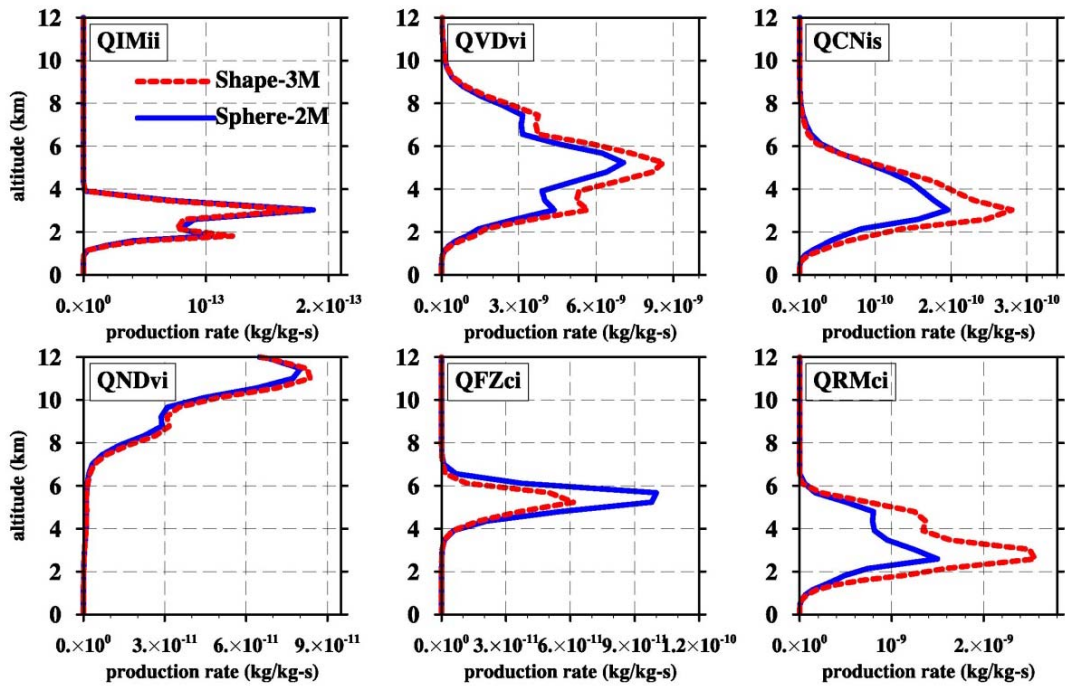


Figure 4.32 Same as Figure 4.29 but for mixing ratio change rates ($\text{kg kg}^{-1} \text{s}^{-1}$) of pristine ice. $QIMii$ for multiplication, $QVDvi$ for deposition growth, $QCNis$ for aggregation to snow-aggregates, $QNDvi$ for deposition-nucleation, $QFZci$ for cloud droplets freezing, and $QRMci$ for riming growth.

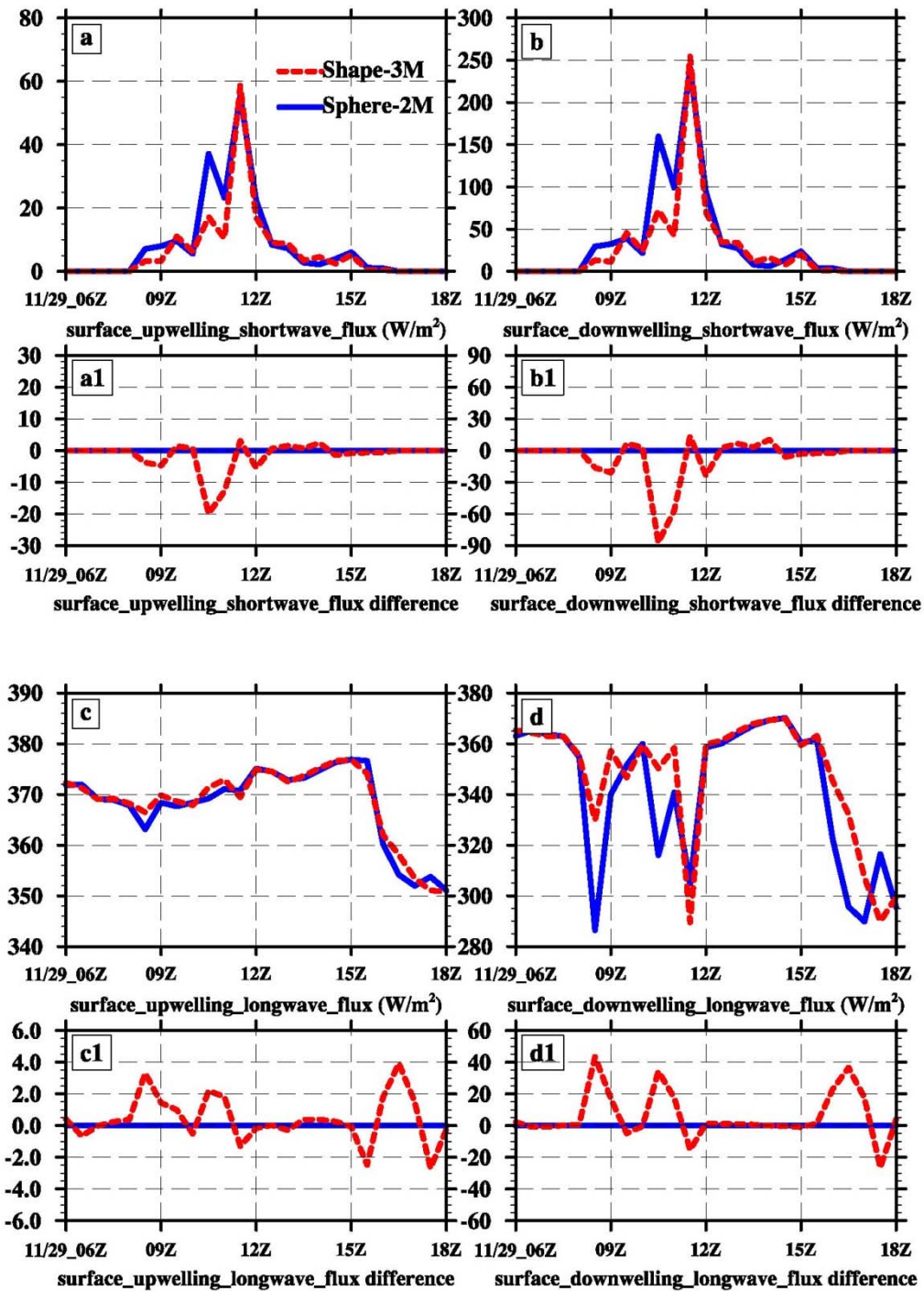
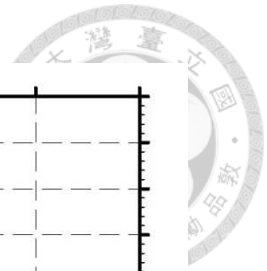


Figure 4.33 Time series of the regional averaged surface radiation fluxes (in W m^{-2}) around CFARR site within 0.05° for (a) the upwelling shortwave flux (in negative), (b) the downwelling shortwave flux, (c) the upwelling longwave flux (in negative), and (d) the downwelling longwave flux separately for Sphere-2M (in solid blue) and Shape-3M (in dash red) runs. Panels (I) were the differences between two model runs.



Appendix A

Source and Sink Terms

The microphysical source/sink terms of the continuity equations inside the new scheme are listed below. These equations are for the version of ice-four-moment scheme. For the two-moment version of spherical ice crystal with fixed bulk density, (A14) and (A15) are not used, nor are any equations for tendencies of F_i and V_i .

The tendencies for the mass mixing ratios are

$$\left. \frac{dQ_v}{dt} \right|_S = \begin{cases} -QAC_{ac} - QAC_{ar} - QAC_{cv} - QND_{vi} - QVD_{vc} - QVD_{vr} - QVD_{vi} \\ -QVD_{vs} - QVD_{vg} - QVD_{vh} - QSB_{iv} - QSB_{sv} - QSB_{gv} - QSB_{hv} \\ -QEV_{cv} - QEV_{rv} - QEV_{sv} - QEV_{gv} - QEV_{hv} \end{cases} \quad (A1)$$

$$\left. \frac{dQ_c}{dt} \right|_S = \begin{cases} QAC_{ac} + QAC_{cv} - QAC_{rc} + QVD_{vc} + QEV_{cv} - QHO_{ci} - QNM_{ci} \\ -QNC_{ci} - QML_{ic} - QIM_{csi} - QIM_{cgi} + QBK_{rc} - QCN_{cr} - QRM_{ci} \\ -QRM_{cs} - QRM_{cg} - QRM_{ch} - QCL_{cr} \end{cases} \quad (A2)$$

$$\left. \frac{dQ_r}{dt} \right|_S = \begin{cases} QAC_{ar} + QAC_{rc} + QVD_{vr} + QEV_{rv} - QHO_{rh} (-QNM_{rh}) - QML_{ir} \\ -QML_{sr} - QML_{gr} - QML_{hr} - QIM_{rsi} - QIM_{rgi} - QBK_{rc} + QCN_{cr} \\ -QRM_{ri} - QRM_{rs} - QRM_{rg} - QRM_{rh} + QCL_{cr} + \delta_w (QH_{wsh} - QH_{wml}) \end{cases} \quad (A3)$$

$$\left. \frac{dQ_i}{dt} \right|_S = \begin{cases} QND_{vi} + QVD_{vi} + QSB_{iv} + QFZ_{ci} (= QHO_{ci} + QNM_{ci} + QNC_{ci}) \\ + QML_{ir} + QML_{ic} + QIM_{ii} (= QIM_{csi} + QIM_{rsi} + QIM_{cgi} + QIM_{rgi}) \\ -QIN_{ig} - QCN_{is} + QRM_{ci} - QCL_{ir} - QCL_{is} - QCL_{ig} - QCL_{ih}^{*2} \end{cases} \quad (A4)$$

$$\left. \frac{dQ_s}{dt} \right|_S = \begin{cases} QVD_{vs} + QSB_{sv} + QEV_{sv} + QML_{sr} + QCN_{is} + QRM_{cs} - QIN_{sg} \\ + QCL_{is} - QCL_{sr} - QCL_{sg} - QCL_{sh}^{*2} + QCL_{srs} \end{cases} \quad (A5)$$

$$\left. \frac{dQ_g}{dt} \right|_S = \begin{cases} QVD_{vg} + QSB_{gv} + QEV_{gv} + QML_{gr} + QIN_{ig} + QIN_{sg} - QCN_{gh} \\ + QRM_{cg} + QCL_{ig} + QCL_{sg} - QCL_{gr} + QCL_{irg} + QCL_{srg} + QCL_{grg} \end{cases} \quad (A6)$$

$$\left. \frac{dQ_h}{dt} \right|_S = \begin{cases} QVD_{vh} + QSB_{hv} + QEV_{hv} + QFZ_{rh} (= QHO_{rh} + QNM_{rh}) + QML_{hr} \\ + QCN_{gh} + QCL_{ih} + QCL_{sh} + QCL_{irh} + QCL_{srh} + QCL_{grh} \\ + \delta_d QH_{drm}^{*1} (= QRM_{ch} + QRM_{rh}) + \delta_w QH_{wml} \end{cases} \quad (A7)$$



The tendencies for the total number concentrations are

$$\left. \frac{dN_c}{dt} \right|_S = \begin{cases} NAC_{ac} + NAC_{cv} - NFZ_{ci} (= NHO_{ci} + NNM_{ci} + NNC_{ci}) - NML_{ic} \\ -NIM_{csi} - NIM_{cgi} + NBK_{rc} - NCN_{cr} - NRM_{ci} - NRM_{cs} - NRM_{cg} \\ -NRM_{ch} - NCL_{cc} - NCL_{cr} \end{cases} \quad (A8)$$

$$\left. \frac{dN_r}{dt} \right|_S = \begin{cases} NAC_{ar} + NAC_{rc} - NFZ_{rh} (= NHO_{rh} + NNM_{rh}) - NML_{ir} - NML_{sr} \\ -NML_{gr} - NML_{hr} - NIM_{rsi} - NIM_{rgi} - NBK_{rc} + NBK_{rr} + NCN_{cr} \\ -NRM_{ri} - NRM_{rs} - NRM_{rg} - NRM_{rh} - NCL_{rr} + \delta_w NH_{wsh} \end{cases} \quad (A9)$$

$$\left. \frac{dN_i}{dt} \right|_S = \begin{cases} NND_{vi} + NSB_{iv} + NFZ_{ci} (= NHO_{ci} + NNM_{ci} + NNC_{ci}) + NML_{ir} \\ + NML_{ic} + NIM_{ii} (= NIM_{csi} + NIM_{rsi} + NIM_{cgi} + NIM_{rgi}) - NIN_{ig} \\ -NCN_{is} - NCL_{ir} - NCL_{is} - NCL_{ig} - NCL_{ih}^{*2} \end{cases} \quad (A10)$$

$$\left. \frac{dN_s}{dt} \right|_S = \begin{cases} NSB_{sv} + NML_{sr} - NIN_{sg} + NCN_{is} - NCL_{sr} - NCL_{ss} - NCL_{sg} \\ -NCL_{sh}^{*2} + NCL_{srs} \end{cases} \quad (A11)$$

$$\left. \frac{dN_g}{dt} \right|_S = \begin{cases} NSB_{gv} + NML_{gr} + NIN_{ig} + NIN_{sg} - NCN_{gh} - NCL_{gr} + NCL_{irg} \\ + NCL_{srg} + NCL_{grg} \end{cases} \quad (A12)$$

$$\left. \frac{dN_h}{dt} \right|_S = \begin{cases} NSB_{hv} + NFZ_{rh} (= NHO_{rh} + NNM_{rh}) + NML_{hr} + NCN_{gh} + NCL_{irh} \\ + NCL_{srh} + NCL_{grh} \end{cases} \quad (A13)$$

The tendency for the pristine ice shape moment is

$$\left. \frac{dF_i}{dt} \right|_S = \begin{cases} FND_{vi} + FVD_{vi} + FSB_{iv} + FFZ_{ci} (= FHO_{ci} + FNM_{ci} + FNC_{ci}) \\ + FML_{ir} + FML_{ic} + FIM_{ii} (= FIM_{csi} + FIM_{rsi} + FIM_{cgi} + FIM_{rgi}) \\ -FIN_{ig} - FCN_{is} + FRM_{ci} - FCL_{ir} - FCL_{is} - FCL_{ig} - FCL_{ih}^{*2} \end{cases} \quad (A14)$$

The tendency for the pristine ice volume moment is

$$\left. \frac{dV_i}{dt} \right|_S = \begin{cases} VND_{vi} + VVD_{vi} + VSB_{iv} + VFZ_{ci} (= VHO_{ci} + VNM_{ci} + VNC_{ci}) \\ + VML_{ir} + VML_{ic} + VIM_{ii} (= VIM_{csi} + VIM_{rsi} + VIM_{cgi} + VIM_{rgi}) \\ -VIN_{ig} - VCN_{is} + VRM_{ci} - VCL_{ir} - VCL_{is} - VCL_{ig} - VCL_{ih}^{*2} \end{cases} \quad (A15)$$

The equation of air temperature change rate is

$$\left. \frac{dT}{dt} \right|_s = \left[\begin{array}{l} L_v \left(\begin{array}{l} QAC_{cv} + QAC_{rc} + QVD_{vc} + QVD_{vr} + QEV_{cv} + QEV_{rv} \\ + QEV_{sv} + QEV_{gv} + QEV_{hv} \end{array} \right) + \\ L_f \left(\begin{array}{l} QFZ_{ci} + QFZ_{rh} + QML_{ir} + QML_{ic} + QML_{sr} + QML_{gr} \\ + QML_{hr} + QRM_{ci} + QRM_{cs} + QRM_{cg} + QRM_{ri} \\ + QRM_{rs} + QRM_{rg} + QIM_{ii} + \delta_d QH_{drm}^{*1} + \delta_w QH_{wml} \end{array} \right) + \\ L_s \left(\begin{array}{l} QVD_{vi} + QVD_{vs} + QVD_{vg} + QVD_{vh} + QSB_{iv} + QSB_{sv} \\ + QSB_{gv} + QSB_{hv} + QND_{vi} \end{array} \right) \end{array} \right] / c_{pm} \quad (A16)$$

*¹: $QH_{drm} = QRM_{ch} + QRM_{rh}$; δ_d and δ_w are for hail dry- and wet- growth modes;

*²: The collection efficiency E is switched to unity for hail wet-growth mode.

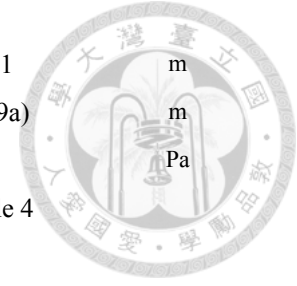
Appendix B



List of Symbols

Symbol	Description	Value	Units
a_A	Area parameter for pristine ice		
a_{mx}	Mass parameter for category x	Table 3	kg m^{-3}
a_{mi0}	Initial mass parameter for pristine ice	$\pi\rho_{i0}/6$	kg m^{-3}
a_{vx}	Fall speed parameter for category x	Table 3	$\text{m}^{1-bx}\text{s}^{-1}$
A'	Parameter in Bigg freezing equation	0.66	K^{-1}
A_{dep}	Pre-factor for ice diffusional growth		
A_{DK}	Thermodynamic function of temperature and pressure	(2.77c)	
A_{NU}	Pre-factor for ice deposition nucleation		$\text{m}^{-2}\text{s}^{-1}$
$A(D)$	Area of a particle with a diameter D	(2.48)	m^2
AB_i	Thermodynamic function with respect to ice		m^{-2}s
AB_w	Thermodynamic function with respect to water		m^{-2}s
b_A	Area parameter for pristine ice		
b_1	Parameter in ventilation factor		
b_2	Parameter in ventilation factor		
b_{mx}	Mass parameter for category x	Table 3	
b_{vx}	Fall speed parameter for category x	Table 3	
B'	Parameter in Bigg freezing equation	100	$\text{m}^{-3}\text{s}^{-1}$
C_i	Electrostatic capacitance in diameter for pristine ice		m
C_0	Non-dimensional surface roughness parameter	0.6	
C_1	Non-dimensional surface roughness parameter		
C_2	Non-dimensional surface roughness parameter		
c_p	Specific heat of dry air	1005.46	$\text{J kg}^{-1}\text{K}^{-1}$
c_{pi}	Specific heat of ice	2093	$\text{J kg}^{-1}\text{K}^{-1}$
c_{pm}	Specific heat of moist air		$\text{J kg}^{-1}\text{K}^{-1}$
c_{pw}	Specific heat of liquid water	4218	$\text{J kg}^{-1}\text{K}^{-1}$
D_{i0}	Initial diameter of ice crystal	6	μm
D_{ia}	Lateral axes of the ice crystal		m
D_{ic}	Principal axis of the ice crystal		m
D_{max}	Maximum dimension		m
D_v	Diffusivity of water vapor in air		m^2s^{-1}
D_x	Mean volume diameter of category x		m

D_{shed}	Mean diameter of shedding raindrops	0.001	m
D_{SLL}	The diameter of Shumann-Ludlam limit	(2.89a)	m
e_{sw}	Saturation vapor pressure w.r.t. water		Pa
E_{xy}	Bulk collection efficiency between categories x and y	Table 4	
f_g	Geometric term of aerosol for ice deposition nucleation		
f_{vx}	Ventilation factor for category x		
f_{b1}	Parameter of ventilation factor		
f_{b2}	Parameter of ventilation factor		
f_{b3}	Parameter of ventilation factor		
$f(\beta)$	Shape enhanced factor	(2.14)	
f_β	Function of adaptive growth ratio	$3(\beta+1)/(\beta+2)$	
g	Gravitational acceleration		
g_β	Function of adaptive growth ratio	$3/(\beta+2)$	
g_v	Asymmetry factor		
h_β	Function of adaptive growth ratio	$3\beta/(\beta+2)$	
$H_h(T)$	The specific total heat of hailstone particle at T		J
$H_h(T_0)$	The specific total heat of hailstone at 0°C		J
J_{dep}	Deposition nucleation rate per particle and time	(2.79a)	s^{-1}
J_{hof}	Homogeneous freezing rate per particle and time		s^{-1}
k	Boltzmann constant	1.38×10^{-23}	J K^{-1}
k_a	Thermal conductivity of air		$\text{Jm}^{-1}\text{s}^{-1}\text{K}^{-1}$
L_f	Latent heat of freezing/melting		J kg^{-1}
$L_f(T_0)$	Latent heat of freezing/melting at $T = 0^\circ\text{C}$	335276.3	J kg^{-1}
L_s	Latent heat of deposition/sublimation		J kg^{-1}
L_v	Latent heat of condensation/evaporation		J kg^{-1}
m_{core}	Hailstone ice core		kg
m_t	Total mass of the particles during wet growth		kg
m_w	Total mass of water surrounding the hailstone	(2.94a)	kg
m_w^*	Critical mass for shed water to occur	(2.95a)	g
$m_x(D_x)$	Mass of a particle with a diameter D for category x	(2.45a)	kg
M_k	k th moment of size spectrum		
$M_{x,k}$	k th moment of size spectrum for category x		
M_X	Moment of Best number	(2.51)	
M_v	Volume moment of pristine ice	(2.8)	
M_ϕ	Shape moment of pristine ice	(2.7)	
N_{0x}	Intercept parameter for category x		
N_{aer}	Number concentration of aerosol particles		cm^{-3}
N_{in}	Number concentration of ice nuclei		L^{-1}





N_x	Number concentration for category x		kg^{-1}
$N_x(D_x)$	Size distribution function for category x		
Q_{vsi}	Water vapor mixing ratio at ice saturation		kg kg^{-1}
Q_{vsw}	Water vapor mixing ratio at water saturation		kg kg^{-1}
$Q_{vsi}(T_0)$	Saturation vapor mixing ratio w.r.t. ice at $T = 0^\circ\text{C}$		kg kg^{-1}
Q_x	Mixing ratio for category x		kg kg^{-1}
N_{Re}	Reynolds number		
r	Spherical equivalent radius of ice crystal		m
r_0	Initial radius of ice crystal	3	μm
r_e	Effective radius	(2.75)	m
r_N	Nucleus (aerosol particle) radius	Table 8	m
R_x	Mean volume radius for the category x		m
R_v	Gas constant for water vapor	461510	$\text{J K}^{-1}\text{kg}^{-1}$
S_c	Schmidt number		
T	Temperature of air		K
T_C	Temperature of air in Celsius		$^\circ\text{C}$
T_0	Triple point of water	273.15	K
V_i	Volume of pristine ice		m^3
V_{i0}	Maximum volume of pristine ice		m^3
v_x	Fall speed for particle of category x		ms^{-1}
v_{Qx}	Mass-weighted fall speed of category x	(2.56)	ms^{-1}
v_{Nx}	Number-weighted fall speed of category x	(2.57)	ms^{-1}
$v_x(D_x)$	Fall speed of a particle with a diameter D of category x	(2.50)	ms^{-1}
w	Air density correction	$(\rho_0/\rho_a)^{0.5}$	
w_v	Single scattering albedo		
X	Best number (or Davies number)		
X_{disp}	Dispersion of the fall velocity spectrum of ice	0.25	
z	Thickness of a cloud layer		m
α_x	Spectral index for category x	Table 3	
β	Adaptive growth ratio		
β_v	Extinction coefficient		
δ_0	Non-dimensional surface roughness parameter	5.83	
ϕ_i	Pristine ice aspect ratio		
$\Gamma(n)$	Complete gamma function of number n		
$\Gamma(T)$	Inherent growth ratio		
λ_x	Slope parameter for category x		m^{-1}
θ_{dep}	Contact angle for ice deposition nucleation	Table 8	degree
θ_s	Solar zenith angle		degree

ρ_0	Surface air density		kg m^{-3}
ρ_a	Density of air		kg m^{-3}
$\rho_{i,dep}$	Deposition density for pristine ice	(2.19)	kg m^{-3}
$\rho_{i,rim}$	Riming density for pristine ice	(2.33)	kg m^{-3}
ρ_{i0}	Initial density of pristine ice	910	kg m^{-3}
ρ_x	Bulk density for category x	Table 3	kg m^{-3}
τ_i	Cloud ice optical depth		
ζ	Function of adaptive growth ratio	$(\beta-1)/(\beta+2)$	
μ_a	Dynamic viscosity of air		$\text{kg m}^{-1}\text{s}^{-1}$
ν	Kinetic viscosity		m^2s^{-1}
$\Delta g^\#$	Activation energy	Table 8	J
$\Delta g_{g,dep}$	Homogeneous energy for germ formation in the vapor phase		J
ΔQ_{vi}	Supersaturation with respect to ice ($=Q_v-Q_{vsi}$)		kg kg^{-1}
$\Delta \rho_v$	Excess water vapor density		kg m^{-3}
ΔS_i	Supersaturation ratio with respect to ice ($=Q_v/Q_{vsi}-1$)		
ΔS_w	Supersaturation ratio with respect to water ($=Q_v/Q_{vsw}-1$)		
Δt	Model time step		s
ΔV_{im}	Impact velocity		ms^{-1}

